

Andrea Cataldo
Egidio De Benedetto
Giuseppe Cannazza

Broadband Reflectometry for Enhanced Diagnostics and Monitoring Applications



Springer

Lecture Notes in Electrical Engineering

Volume 93

Andrea Cataldo, Egidio De Benedetto,
and Giuseppe Cannazza

Broadband Reflectometry for Enhanced Diagnostics and Monitoring Applications

Ing. Andrea Cataldo
University of Salento
Dept. Innovation Engineering
Via Monteroni
73100 Lecce
Italy
Ph.: 0039-0832-297823
Fax: 0039-0832-1830127
E-mail: andrea.cataldo@unisalento.it

Dr. Giuseppe Cannazza
University of Salento
Dept. Innovation Engineering
Via Monteroni
73100 Lecce
Italy
E-mail: giuseppe.cannazza@unisalento.it

Ing. Egidio De Benedetto
University of Salento
Dept. Innovation Engineering
Via Monteroni
73100 Lecce
Italy
E-mail: egidio.debenedetto@unisalento.it

ISBN 978-3-642-20232-2

e-ISBN 978-3-642-20233-9

DOI 10.1007/978-3-642-20233-9

Lecture Notes in Electrical Engineering ISSN 1876-1100

Library of Congress Control Number: 2011925494

© 2011 Springer-Verlag Berlin Heidelberg

This work is subject to copyright. All rights are reserved, whether the whole or part of the material is concerned, specifically the rights of translation, reprinting, reuse of illustrations, recitation, broadcasting, reproduction on microfilm or in any other way, and storage in data banks. Duplication of this publication or parts thereof is permitted only under the provisions of the German Copyright Law of September 9, 1965, in its current version, and permission for use must always be obtained from Springer. Violations are liable to prosecution under the German Copyright Law.

The use of general descriptive names, registered names, trademarks, etc. in this publication does not imply, even in the absence of a specific statement, that such names are exempt from the relevant protective laws and regulations and therefore free for general use.

Typeset & Coverdesign: Scientific Publishing Services Pvt. Ltd., Chennai, India.

Printed on acid-free paper

9 8 7 6 5 4 3 2 1

springer.com

*To Davide, Federico and Francesca: the
ones who motivate me every single day
Andrea*

*To my mother
Egidio*

Foreword

One of the advantages of microwave techniques for diagnostics and monitoring applications is that microwave signals penetrate within dielectric structures and they are sensitive to the presence of interior flaws and interfaces. Broadband microwave techniques provide additional information either through incorporating finite range resolution or multi-frequency material characterization.

Microwave reflectometry is commonly implemented in a one-sided manner, which in turn makes it more attractive from practical point-of-view. The interest in broadband microwave reflectometry for materials diagnostics and for monitoring physical parameters of materials covers a broad realm of applications including: civil engineering and infrastructure, agriculture and medicine. Broadband microwave reflectometry is an area of engineering and science from which many publications have resulted over the years.

The authors of this monograph have expertly brought together information from many of such papers and by many investigators as well as their own. Of course, this monograph does not reflect all works in this field, nor does it answer all questions with respect to diagnosis and monitoring applications. However, it serves as an excellent summary of important broadband reflectometry approaches including the time domain reflectometry (TDR), the frequency domain reflectometry (FDR) and the TDR/FDR combined approaches. It is also important that their specific applications for the characterization of liquid materials, for monitoring of water content and for antenna measurements are considered in detail.

They include simultaneous measurement of the levels and the dielectric characteristics of liquid materials in layered media with consideration of measurement accuracy improvement using appropriate probe design, custom-made fixtures for calibration and a targeted optimization routine.

Another application I would like to mention focuses on moisture measurements and includes estimation of moisture content directly from TDR and through TDR/FDR combined approach. Though these methods and techniques are developed for soil measurements, they can also be applied for varieties of materials.

I believe this monograph will be useful to scientists, researchers and practitioners as well as students for future comprehensive studies, investigations and applications.

Rolla (MO),
February 2011

Prof. Sergey Kharkovsky
Missouri University of Science and Technology
Rolla (MO)

Preface

Monitoring and diagnostics are essential in many application fields: for the industry, for laboratory applications, as well as for countless other areas. Therefore, over the years, considerable research effort has been devoted to explore innovative technologies and methods that could guarantee increasingly reliable and accurate monitoring solutions. In this regard, electromagnetic methods have attracted great interest, also thanks to their vast potential for nondestructive testing. In particular, broadband microwave reflectometry (BMR) has established as a powerful tool for monitoring purposes; in fact, this technique can balance several contrasting requirements, such as the versatility of the system, low implementation cost, real-time response, possibility of remote control, reliability, and adequate measurement accuracy.

On such bases, the central topic of this book is the investigation of innovative BMR-based methods for monitoring applications. More specifically, throughout the book, the different approaches of this technique will be considered (i.e., time domain reflectometry - TDR, frequency domain reflectometry - FDR, and the TDR/FDR combined approach) and several applications will be thoroughly investigated. For each considered application, particular attention will be focused on innovative strategies and procedures that can be adopted to enhance the overall measurement accuracy. There are many application areas where TDR and FDR (or the combination of the two) have proved useful and promising. Therefore, it comes as no surprise that the applications considered herein are very diverse from each other and cover different fields. The present book is structured as follows.

In Chapt. 1, a brief overview of the contexts in which monitoring has assumed a paramount importance is given.

Chapt. 2 introduces the theoretical principles that are at the basis of BMR, and describes the parameters of interest in this technique. Furthermore, this chapter introduces to dielectric spectroscopy, which is one of the pivotal applications of BMR (in fact, as well known, many of the applications of BMR often descend from dielectric spectroscopy measurements).

In Chapt. 3, the TDR, FDR, and TDR/FDR combined approaches are thoroughly discussed, and the related advantages and shortcomings are addressed. In particular, some effective strategies for enhancing the accuracy of BMR measurements; all these strategies basically aim at compensating for the effect of systematic errors.

Chapt. 4 presents some innovative BMR-based solutions for the simultaneous monitoring of qualitative and quantitative characteristics of liquids. This is quite a broad application area, and the investigated applications cover diverse sectors: from the monitoring of stratified liquids (particularly useful for the industry of petrochemicals) to the analysis on edible liquids (useful, for example, for anti-adulteration control on vegetable oils).

Chapt. 5 is focused on the qualitative analysis of granular materials and on moisture measurements. This last application, which is particularly useful in soil science and agriculture, can be extended also to different areas. In fact, the qualitative status in the production of agrofoods, in the production of inert materials, and in the fertilizer industry (just to name a few of the investigated application fields) is strongly related to the amount of water content of these materials.

Finally, Chapt. 6 deals with the characterization of antennas through BMR. In particular, some useful guidelines for antenna characterization are presented. More specifically, the proposed procedures can help obtaining a higher measurement accuracy even when measurements are not performed in dedicated facilities (i.e., anechoic chambers).

In all the described procedures and methods, the ultimate goal is to endow them with a significant performance enhancement in terms of measurement accuracy, low cost, versatility, and practical implementation possibility, so as to unlock the strong potential of BMR.

Lecce (Italy),
February 2011

Andrea Cataldo
Egidio De Benedetto
Giuseppe Cannazza

Acknowledgements

With great pleasure we express our deepest gratitude to all the people that have contributed, either directly or indirectly, to the completion of this book.

First and former, we thank Dr. Emanuele Piuizzi (Sapienza University, Rome, Italy): without his continuous support and considerable scientific contribution, this book would have not seen the light of the day.

We would also like to thank Prof. Mario Savino, Prof. Amerigo Trotta, and Prof. Filippo Attivissimo (Polytechnic of Bari, Bari, Italy), for their invaluable guidance. Their wisdom and farsightedness have been more than helpful throughout the years. A big thank you also to all the people of the *Electric and Electronic Measurements Group* of the Polytechnic of Bari for the constant exchange of ideas and the fruitful collaborations.

We deeply thank Prof. Luciano Tarricone, Dr. Luca Catarinucci, and Dr. Giuseppina Monti (*Electromagnetic Field Group*, University of Salento, Lecce, Italy) for constantly providing sensible advice; we hold them in high regard and we deeply thank them for their insightful suggestions.

We also thank Dr. Antonio Masciullo for his contribution in transforming many of the experiments from ambitious ideas into reality.

Furthermore, we would like to acknowledge the huge help provided by Dr. Agoston Agoston (Hyperlabs Inc., Beaverton, OR), who has been tireless and always available for providing constructive advice.

Finally, we also thank Prof. Sergey Kharkovsky (Missouri University of Science and Technology, Rolla, MO) for reading the manuscript and for giving us the privilege to host his foreword.

Contents

1	Introduction	1
1.1	The Concept Behind This Book	1
1.2	Survey of Typical Applications of BMR	3
1.2.1	Electrical Components Characterization: Testing and Localization of Faults	3
1.2.2	Measurements on Soil for Agricultural and Geotechnical Purposes	4
1.2.3	Civil Engineering and Infrastructural Monitoring	4
1.2.4	Dielectric Spectroscopy Measurements	5
1.2.5	Applications in Industrial Monitoring	5
1.3	Organization and Content of the Book	5
	References	7
2	Basic Physical Principles	11
2.1	Transmission Line Basics	11
2.1.1	Coaxial Transmission Line	12
2.1.2	Bifilar Transmission Line	14
2.1.3	Microstrip Line	14
2.2	Reflected Waves	15
2.3	Characteristic Parameters of Electrical Networks	16
2.4	Reflectometry Measurements for Dielectric Spectroscopy	19
2.4.1	Dielectric Relaxation Models	20
	References	23
3	Broadband Reflectometry: Theoretical Background	25
3.1	Broadband Microwave Reflectometry: Theoretical Background	25
3.2	Time Domain Reflectometry (TDR)	26
3.2.1	Typical TDR Measurements	29

3.2.2	Typical TDR Instrumentation	30
3.3	Frequency Domain Reflectometry (FDR)	33
3.4	TD/FD Combined Approach	35
3.4.1	Preserving Measurement Accuracy in the TDR/FDR Transformation	36
3.5	The Sensing Element	37
3.6	Strategies for Enhancing Accuracy in BMR Measurements	41
3.6.1	Calibration Procedure in Time Domain	41
3.6.2	Calibration Procedure in Frequency Domain	42
3.6.3	Time-gated Frequency Domain Approach	43
3.6.4	Transmission Line Modeling and Inverse Modeling ..	44
	References	47
4	Quantitative and Qualitative Characterization of Liquid Materials	51
4.1	Introduction	51
4.2	Estimation of Levels and Permittivities of Industrial Liquids Directly from TDR	53
4.2.1	Probe Design and Realization	54
4.2.2	Sources of Errors and Compensation Strategies in TD	56
4.2.3	Validation of the Method on Dielectric Liquids	58
4.3	Estimation of Levels and Permittivities of Industrial Liquids Using the TD/FD Approach	60
4.3.1	Transmission Line Modeling of the Measurement Cell	61
4.3.2	Measurement Setup and Enhanced Probe Design	62
4.3.3	Experimental Validation of the Method	64
4.4	Dielectric Spectroscopy of Edible Liquids: The Vegetable Oils Case-Study	71
4.4.1	Design of the Measurement Cell and Transmission Line Modeling	72
4.4.2	Experimental Results for Vegetable Oils	77
	References	82
5	Qualitative Characterization of Granular Materials and Moisture Measurements	85
5.1	Introduction	85
5.2	Dielectric Models for the Estimation of Water Content	87
5.3	Evaluation of Moisture Content Directly from TDR	89
5.3.1	Details on the Experimental Procedure	90
5.3.2	Uncertainty Evaluation for Apparent Dielectric Permittivity Measurement and Individuation of the Calibration Curves	91

- 5.3.3 Measurement Results and Instrumental Performance Comparison 93
- 5.4 Moisture Content Measurements through TD/FD Combined Approach and TL Modeling 97
 - 5.4.1 Moisture Content Measurements through Dielectric Mixing Model 97
 - 5.4.2 Triple-Short Calibration Procedure 98
- 5.5 Enhancements of TDR-Based Static Electrical Conductivity Measurement 107
 - 5.5.1 Traditional TDR-Based Static Electrical Conductivity Measurement 108
 - 5.5.2 Innovative Calibration Strategies: The TLM and the ICM Methods 110
 - 5.5.3 Validation of the Methods 115
 - 5.5.4 Practical Considerations 119
- 5.6 Noninvasive Moisture Content Measurements 119
 - 5.6.1 Basic Theory of Microstrip Antennas 120
 - 5.6.2 Experimental Validation of the Method: Measurements on Moistened Sand Samples 122
- References 128
- 6 BMR Characterization of Antennas through the Combined TD/FD Approach 133**
 - 6.1 Introduction 133
 - 6.2 Measurement Setup for the Validation of the Method 134
 - 6.3 Acquisition in Time Domain 135
 - 6.4 RFId Antenna Results 137
 - 6.4.1 Practical Guidelines for Retrieving Accurate Measurements 138
 - 6.5 Biconical Antenna Results 145
 - References 147

Acronyms

AC	alternate current
AUT	antenna under test
BMR	broadband microwave reflectometry
DC	direct current
EM	electromagnetic
FD	frequency domain
FDC	frequency domain calibration
FFT	fast Fourier transform
FTIR	Fourier transform infrared
FDR	frequency domain reflectometry
GBNM	globalized bounded Nelder-Mead
ICM	independent capacitance measurement
IF	intermediate frequency
IFFT	inverse fast Fourier transform
LO	local oscillator
LUT	liquid under test
MUT	material under test
NMR	nuclear magnetic resonance
PCA	principal component analysis
RF	radio frequency
RFID	radio frequency identification
rmse	root mean square error
SMA	sub-miniature A
SNR	signal to noise ratio
SOL	short open load
SUT	system under test
TD	time domain

TDR	time domain reflectometry
TEM	transverse electromagnetic
TL	transmission line
TLM	transmission line method
TM	transverse magnetic
TSC	triple-short calibration
VNA	vector network analyzer
VSWR	voltage standing wave ratio

Chapter 1

Introduction

‘Common sense is the collection of prejudices acquired by age eighteen’.
Albert Einstein

Abstract. This chapter introduces to broadband microwave reflectometry (BMR), which is the expression used in this book to indicate an electromagnetic technique used for monitoring and diagnostics purposes. The adjective *broadband* emphasizes the fact that the analysis can be carried out over a wide frequency range. A brief survey of the typical applications of BMR is also provided.

1.1 The Concept Behind This Book

Under the term *monitoring*, the Cambridge dictionary states the following definition

to watch and check a situation carefully for a period of time in order to discover something about it.

Similarly, the word *diagnosis* indicates

a judgment about what a particular illness or problem is, made after examining it.

Such broad, and yet unambiguous definitions seem to emphasize the urgency associated with the terms themselves [1]. As a matter of fact, now more than ever, ‘keeping the situation under control’, for cognitive or predictive purposes, is a transversal need in a number of interdisciplinary sectors, especially in industrial, environmental, civil, and agricultural areas. As a direct consequence, strict regulations have been enforced and guidelines have been issued that dictate specific standards (either qualitative or quantitative) that should be complied with, in order to ensure the suitability of the ‘product’ or of the ‘process’. In this scenario, monitoring and diagnosis procedures are used for the optimization of process and for triggering possible corrective actions, or for checking the compliance of the product with pre-established quality standards.

In general, a monitoring program gathers data for several purposes, such as

- to draw comparisons against standard or target *status*;
- to make comparisons between different conditions or to conduct analyses;

- to establish long-term trends in systems under observation;
- to estimate changes with respect to a reference *status*.

There are four major features that can summarize the desirable requirements that monitoring systems should satisfy: i) time saving; ii) energy saving; iii) economical feasibility (or profitability); and iv) accuracy and reliability. As a matter of fact, the Scientific Community is in constant struggle to individuate innovative monitoring solutions that can help to simultaneously satisfy such requirements or, at least, achieve an optimal trade-off among them.

Monitoring implies measuring, either directly or indirectly, a quantity that represents the value of the parameter of interest. Most measurement techniques rely on applying a stimulus to the *system under test* (SUT) and on analyzing how the system responds; one of the most popular approaches consists in *pulsing* the SUT. A broad classification of measurement techniques based on pulsing includes transmission measurements and reflectometric measurements: the former rely on the analysis of the signal that is *transmitted through* the SUT; whereas the latter are based on the analysis of the signal *reflected by* the SUT. Reflectometric measurements typically require a simpler measurement setup; hence, they are generally more adaptable to a wider range of conditions. Depending on the specific application field, the stimulus signal may be acoustic, electromagnetic, or optic.

The present book focuses on the use of electromagnetic (EM) signals as stimuli: this approach is herein referred to as broadband microwave reflectometry (BMR). This expression emphasizes the fact that the analysis is performed over a wide frequency range, that theoretically goes from 0 Hz up to the microwave region of the frequency spectrum (this is contrast, for example, to resonance methods which rely on analysis at a specific value of frequency).

In such a context, this book is intended to provide a comprehensive overview on the capabilities offered by BMR: in fact, this technique arguably encompasses the aforementioned needs, thus allowing to achieve, simultaneously, low implementation costs, accuracy of results, and in situ implementation in numerous practical applications.

As will be detailed in the following chapters, BMR-based measurements can be performed either in the time domain (time domain reflectometry - TDR) or, equivalently, in the frequency domain (frequency domain reflectometry - FDR). Depending on the specific application, one approach may be more suitable than the other. Typically, instrumentation operating in time domain (TD) is usually less expensive than instruments operating in frequency domain (FD). In fact, portable low-cost units are readily available on the market, thus making the TDR technique appealing for in situ applications. Commonly, step-like voltage function and impulse are used as stimuli for TD measurements.

On the other hand, reflectometric measurements performed directly in FD are typically carried out through vector network analyzers (VNAs). These instruments use sinusoidal signals as stimuli, and they usually provide high measurement accuracy, thanks to the possibility of directly performing calibration procedures, which are crucial for reducing the effect of systematic error sources.

An optimal trade-off (in terms of low cost, in situ applications, and measurement accuracy), can be achieved through a TD/FD combined approach. This particular approach involves standard measurements in one domain and, through a suitable data-processing, the corresponding information is retrieved in the other domain.

On such bases, the aim of the book is not only to provide a clear picture of the most interesting state-of-the-art applications of BMR, but also to give helpful hints that can allow to fully exploit the potential of BMR. In particular, throughout the book several strategies are presented (such as calibration techniques and innovative processing strategies), all aimed at enhancing measurement accuracy, while still preserving low cost and possibility of practical implementation. Particular emphasis is given to the possibility of implementing a TD/FD combined approach that, starting from measurements involving low-cost TDR apparatus, could provide accurate results in FD, useful for the intended monitoring purposes. The book also reports some significant experimental results that corroborate the proposed methods.

It is important to point out that the explored applications all have strong potential also for automation, which makes BMR particularly appealing for industrial applications.

Finally, it is worth mentioning that, although the present book focuses on microwave reflectometry, many of the core ideas can be readily extended to applications of reflectometry that employ different stimulus signals.

1.2 Survey of Typical Applications of BMR

Thanks to the intrinsic versatility and accurate performance, applications of microwave reflectometry are numerous and cover a wide range of fields. Just to give a rough idea of the broad spectrum of applications in which BMR can be successfully adopted as a monitoring tool, here follows an overview (which is far from being exhaustive) of some of the most well-established and/or promising application fields.

1.2.1 Electrical Components Characterization: Testing and Localization of Faults

This application strictly relies on measurements of the electric impedance of the SUT: in fact, faults along wires or failure of electrical components cause specific impedance changes that can thus be taken as indicators of malfunction. Several reflectometry-based approaches have been investigated over the years, a clear description of such methods can be found in [8]. However, TDR still remains one of the most advantageous techniques to fulfill this task. In fact, TDR allows to directly measure the impedance profile of the SUT as a function of the electrical distance. As a result, also the spatial location of the fault becomes very straightforward.

Locating faults along cables and wirings (in buildings, aircrafts, and so on) is the foremost application for which TDR was originally developed [7, 21]. Recently, an approach to locate wire faults using reflectometry without physical contact with the wire conductor was presented in [38]. In [32], a method based on TDR response and

genetic algorithm was proposed. The benefits of the TDR/FDR combined approach have been considered for diagnostics on electric power cables (also to monitor incipient defects [37]); in [33], faults are localized by monitoring the cross-correlation characteristics of the observed signal in both TD and FD, simultaneously. BMR is also used for the characterization of power electronics systems [39]. Based on the same principle, TDR has also been used for testing of instrumentation loops in gas turbines during scheduled maintenance [20].

1.2.2 Measurements on Soil for Agricultural and Geotechnical Purposes

Soil measurement is another pivotal application area of BMR. In particular, soil water content measurements represent one of the major practical applications of this technique, with uses that focus on environmental monitoring [34] and on the optimization of irrigation cycles and water resource management [26]. Moisture measurements through BMR start from the estimation of the relative dielectric permittivity of the sample under test: in fact, even a small amount of water (which has a relative dielectric permittivity of approximately 80) increases significantly the overall dielectric permittivity of soils (which, in dry conditions, typically have much lower relative dielectric permittivity).

TDR is also used in geotechnical engineering and environmental control for monitoring liquefaction of soils [28] and for the detection of organic pollutants in sandy soils [17].

BMR is particularly useful also for monitoring the static electrical conductivity of moistened soils. In fact, BMR measurements are performed in the whole frequency range between 0 Hz and the maximum frequency of the used instrument; as a direct result, the problems of direct current (DC) measurements of traditional methods is overcome.

Finally, resorting to TDR, by monitoring the deformation of coaxial cables it is possible to monitor landslides [6, 12], and to assess distributed pressure profiles (useful for evaluating the strength of the ground for constructions [27]).

1.2.3 Civil Engineering and Infrastructural Monitoring

Reflectometric techniques are providing promising results also for monitoring applications in civil engineering. For example, an FDR-based resonant method for the accurate evaluation of the depth of long and shallow surface damages was proposed in [14]. Other nondestructive reflectometry-based monitoring solutions include the detection of chloride ingress and the evaluation of its distribution in reinforced concrete structures (useful for monitoring corrosion) [23]; the determination of the material content of concrete (useful to infer the compressive strength of concrete) [3]; and the determination of water/cement content in fresh Portland cement-based materials [18].

Additionally, in [36] a TDR-based system for sensing crack/strain in reinforced concrete structures was presented; fault location on concrete anchors was investigated in [9]; a TDR-based solution for monitoring cement hydration was described in [11], and so on.

1.2.4 Dielectric Spectroscopy Measurements

BMR has also been extensively used for dielectric spectroscopy of materials, which involves measuring the frequency-dependent dielectric permittivity of the considered material. Typically, this kind of measurements relies on the combination of reflectometric measurements and mathematical models that describe the expected dielectric behavior of the considered material. Dielectric properties are of paramount importance because they can be related to other non-electric properties of the SUT, thus obtaining useful information.

It would be impossible to list all the specific materials for whose characterization BMR has proven useful; however, some of the materials investigated through this technique include alcohol mixtures [2], mixtures of ester with alcohol [30, 31], poly(propylene glycol)water mixtures [29], chlorobenzene with n-methylformamide [22], Nylon-11 with phenol derivatives [13], powders (e.g., zeolite powders [35]). Dielectric characterization through BMR has also been extensively used for food analysis [16] and for application on biological materials (e.g., for breast tissue analysis [25], for diagnosing skin cancer [15], for cerebral edema-related studies [10], etc.).

1.2.5 Applications in Industrial Monitoring

Typical applications of BMR for industrial use include measurement of liquid levels in tanks or containers. Basically, the level of the liquid is inferred from the travel time of the EM signal along the probe immersed in the monitored liquid [19]. Thanks to the capability of discriminating interfaces between materials with different permittivity, TDR can be used for the localization of multiple interfaces in layered media [4, 24].

Other applications of BMR include monitoring of levels in dykes and rivers; moisture evaluation of agrofoods (such as cereals and coffee [5]); monitoring of the osmotic dehydration process for fruit and vegetables; and other quality-control applications that resort to measurement of dielectric characteristics.

1.3 Organization and Content of the Book

The book comprises two main parts: one is more theory-oriented, whereas the other is more practice-oriented. The first part (from chapter two through chapter three) recalls the theoretical background of BMR measurements and presents the strategies

that are used for enhancing measurement accuracy. The second part (from chapter four through chapter six) is a representative collection of experimental results that demonstrate the potential of BMR for various monitoring tasks. Let us see the content of each chapter more in detail.

In the second chapter, the basic theoretical principles behind BMR are recalled. First, a preliminary introduction on the transmission line theory is given. Second, the most important electrical parameters related to BMR are introduced. Particular attention is given to the quantities that are directly measured through BMR, namely the reflection coefficient in time domain ($\rho(t)$) and the reflection scattering parameter ($S_{11}(f)$). Finally, the basic concepts behind dielectric spectroscopy are recalled.

The third chapter describes the ‘actors’ involved in typical BMR measurements. First, TDR and FDR are presented and the related instrumentation is fully described. Successively, the TDR/FDR combined approach is described in detail: as aforementioned, this approach can help exploit the benefits of both TDR and FDR, without necessarily employing two different measurement setups. It is worth mentioning that great emphasis is given on this issue, since it represents the solution that can ultimately lead to the optimization of the cost-benefit ratio in the implementation of the systems. Particular attention is also dedicated to the design of the probes, which is crucial for obtaining accurate results. In the third chapter, also the methods for measuring the dielectric characteristics of materials starting directly from the analysis of TDR waveforms are presented. Additionally, the major error sources in BMR-based measurement systems are described in detail: specific focus is given to the strategies for enhancing measurement accuracy.

The fourth chapter deals with the quantitative and qualitative characterization of liquid materials. In this chapter, BMR-based methods for measuring simultaneously the levels and the dielectric characteristics of liquid materials are presented. Results show that all the proposed methods have strong potential for practical implementation in the field of industrial monitoring.

First, an approach based solely on the analysis of TDR measurements is described and validated. Secondly, a further enhancement of this method is accomplished by resorting to the combination of TDR with FDR. In this second measurement method, the accuracy is enhanced also through the adoption of a transmission line modeling of the measurement cell and through the realization of a custom-made fixture that allows performing an ad hoc short-open-load (SOL) calibration.

Finally, BMR-based measurements of the dielectric characteristic are extended to edible liquids: in particular, vegetable oils are considered. This was done in view of the possibility of performing quality and anti-adulteration control.

The fifth chapter focuses on BMR applications for monitoring water content and static electrical conductivity of granular materials, focusing on applications on soils and on agrofood materials.

First, a TDR-based method for inferring water content from measurements of the apparent dielectric permittivity is presented. This approach, which relies on the individuation of so-called *calibration curves*, is discussed in detail and a metrological assessment is provided.

Successively, a method that takes into account the frequency-dependence of the dielectric permittivity of the moistened granular material (considering the permittivity of each single constituent) is presented. This application is also used as a test-case for validating an innovative calibration procedure that becomes especially useful when the traditional SOL calibration cannot be performed. Furthermore, the adoption of antennas in place of the traditional probes is discussed, thus assessing the possibility of achieving a noninvasive approach.

At the end of chapter fifth, two innovative strategies for enhancing and simplifying TDR-based measurements of electrical conductivity (typically used in soil science) are also addressed.

Finally, the sixth chapter provides some significant examples on the use of TD/FD combined approach for the characterization of antennas. In particular, some guidelines are given for obtaining accurate results even without resorting to expensive facilities such as anechoic chambers. The presented procedure can be extended to other electronic devices or systems as well.

References

- [1] Cambridge advanced learner's dictionary CD-ROM. 3rd edn. (2008)
- [2] Balamurugan, D., Kumar, S., Krishnan, S.: Dielectric relaxation studies of higher order alcohol complexes with amines using time domain reflectometry. *J. Mol. Liq.* 122(1-3), 11–14 (2005)
- [3] Bois, K.J., Benally, A.D., Zoughi, R.: Microwave near-field reflection property analysis of concrete for material content determination. *IEEE Trans. Instrum. Meas.* 49(1), 49–55 (2000)
- [4] Cataldo, A., Tarricone, L., Attivissimo, F., Trotta, A.: Simultaneous measurement of dielectric properties and levels of liquids using a TDR method. *Measurement* 41(3), 307–319 (2008)
- [5] Cataldo, A., Tarricone, L., Cannazza, G., Vallone, M., Cipressa, M.: TDR moisture measurements in granular materials: from the siliceous sand test case to the applications for agro-food industrial monitoring. *Comput. Stand Interfaces* 32(3), 86–95 (2010)
- [6] Corsini, A., Pasuto, A., Soldati, M., Zannoni, A.: Field monitoring of the Corvara landslide (Dolomites, Italy) and its relevance for hazard assessment. *Geomorphology* 66(1-4), 149–165 (2005)
- [7] Dodds, D.E., Shafique, M., Celaya, B.: TDR and FDR identification of bad splices in telephone cables. In: *Proceedings of IEEE Canadian Conference on Electrical and Computer Engineering*, pp. 838–841 (2006)
- [8] Furse, C., Chung, Y.C., Lo, C., Pendayala, P.: A critical comparison of reflectometry methods for location of wiring faults. *Smart Struct. Syst.* 2(1), 25–46 (2006)
- [9] Furse, C., Smith, P., Diamond, M.: Feasibility of reflectometry for nondestructive evaluation of prestressed concrete anchors. *IEEE Sens. J.* 9(11), 1322–1329 (2009)
- [10] Kao, H.P., Shweddyk, E., Cardoso, E.R.: Correlation of permittivity and water content during cerebral edema. *IEEE Trans. Biomedic. Eng.* 46(9), 1121–1128 (1999)
- [11] Hager III, N.E., Domszy, R.C.: Monitoring of cement hydration by broadband time-domain-reflectometry dielectric spectroscopy. *J. Appl. Phys.* 96(9), 5117–5128 (2004)

- [12] Kane, W.F., Beck, T.J., Hughes, J.: Applications of time domain reflectometry to landslide and slope monitoring. In: *Proceedings of the 2nd International Symposium and Workshop on Time Domain Reflectometry for Innovative Geotechnical Applications*, pp. 305–314 (2001)
- [13] Kumar, P.M., Malathi, M.: Dielectric relaxation studies of nylon-11 with phenol derivatives in non-polar solvents using time domain reflectometry. *J. Mol. Liq.* 145(1), 5–7 (2009)
- [14] McClanahan, A., Kharkovsky, S., Maxon, A.R., Zoughi, R., Palmer, D.D.: Depth evaluation of shallow surface cracks in metals using rectangular waveguides at millimeter-wave frequencies. *IEEE Trans. Instrum. Meas.* 59(6), 1693–1704 (2010)
- [15] Mehta, P., Chand, K., Narayanswamy, D., Beetner, D.G., Zoughi, R., Stoecker, W.V.: Microwave reflectometry as a novel diagnostic tool for detection of skin cancers. *IEEE Trans. Instrum. Meas.* 55(4), 1309–1316 (2006)
- [16] Miura, N., Yagihara, S., Mashimo, S.: Microwave dielectric properties of solid and liquid foods investigated by time-domain reflectometry. *J. Food Sci.* 68(4), 1396–1403 (2003)
- [17] Mohamed, A.M.O., Said, R.A.: Detection of organic pollutants in sandy soils via TDR and eigendecomposition. *J. Contam. Hydrol.* 76(3-4), 235–249 (2005)
- [18] Mubarak, K., Boi, K.J.: A simple, robust, and on-site microwave technique for determining water-to-cement ratio (w/c) of fresh portland cement-based materials. *IEEE Trans. Instrum. Meas.* 50(5), 1255–1263 (2001)
- [19] Namarich, C.P.: Time domain reflectometry liquid levels sensors. *IEEE Instr. Meas. Mag.* 4(4), 40–44 (2001)
- [20] Neus, C., Boets, P., Biesen, L.V., Moelans, R., de Vyvere, G.V.: Fault detection on critical instrumentation loops of gas turbines with reflectometry. *IEEE Trans. Instrum. Meas.* 58(9), 2938–2944 (2009)
- [21] O'Connor, K., Dowding, C.H.: *Geomeasurements by pulsing TDR cables and probes*. CRC Press, Boca Raton (1999)
- [22] Pawar, V.P., Patil, A.R., Mehrotra, S.C.: Temperature-dependent dielectric relaxation study of chlorobenzene with n-methylformamide from 10 MHz to 20 GHz. *J. Mol. Liq.* 121, 88–93 (2005)
- [23] Peer, S., Kurtis, K.E., Zoughi, R.: Evaluation of microwave reflection properties of cyclically soaked mortar based on a semiempirical electromagnetic model. *IEEE Trans. Instrum. Meas.* 54(5), 2049–2060 (2005)
- [24] Piuze, E., Cataldo, A., Catarinucci, L.: Enhanced reflectometry measurements of permittivities and levels in layered petrochemical liquids using an 'in-situ' coaxial probe. *Measurement* 42(5), 685–696 (2009)
- [25] Popovic, D., McCartney, L., Beasley, C., Lazebnik, M., Okoniewski, M., Hagness, S.C., Booske, J.H.: Precision open-ended coaxial probes for in vivo and ex vivo dielectric spectroscopy of biological tissues at microwave frequencies. *IEEE Trans. Microw. Theory Tech.* 53(5), 1713–1722 (2005)
- [26] Previati, M., Bevilacqua, I., Canone, D., Ferraris, S., Haverkamp, R.: Evaluation of soil water storage efficiency for rainfall harvesting on hillslope micro-basins built using time domain reflectometry measurements. *Agric. Water Manag.* 97(3), 449–456 (2010)
- [27] Scheuermann, A., Huebner, C.: On the feasibility of pressure profile measurements with time-domain reflectometry. *IEEE Trans. Instrum. Meas.* 58(2), 467–474 (2009)
- [28] Scheuermann, A., Hubner, C., Wienbroer, H., Rebstock, D., Huber, G.: Fast time domain reflectometry (TDR) measurement approach for investigating the liquefaction of soils. *Meas. Sci. Technol.* 21(2) (2010)

- [29] Sengwa, R.J.: Dielectric behaviour and relaxation in poly(propylene glycol)-water mixtures studied by time domain reflectometry. *Polym. Int.* 53(6), 744–748 (2004)
- [30] Sivagurunathan, P., Dharmalingam, K., Ramachandran, K., Prabhakar Undre, B., Khirade, P.W., Mehrotra, S.C.: Dielectric study of butyl methacrylate–alcohol mixtures by time-domain reflectometry. *Phys B: Condens Matter* 387(1-2), 203–207 (2007)
- [31] Sivagurunathan, P., Dharmalingam, K., Ramachandran, K., Undre, B.P., Khirade, P.W., Mehrotra, S.C.: Dielectric studies on binary mixtures of ester with alcohol using time domain reflectometry. *J. Mol. Liq.* 133(1-3), 139–145 (2007)
- [32] Smail, M.K., Pichon, L., Olivas, M., Auzanneau, F., Lambert, M.: Detection of defects in wiring networks using time domain reflectometry. *IEEE Trans. Magn.* 46(8), 2998–3001 (2010)
- [33] Song, E., Shin, Y.J., Stone, P.E., Wang, J., Choe, T.C., Yook, J.G., Park, J.B.: Detection and location of multiple wiring faults via time–frequency-domain reflectometry. *IEEE Trans. Electromagn. Compat.* 51(1), 131–138 (2009)
- [34] Stangl, R., Buchan, G.D., Loiskandl, W.: Field use and calibration of a TDR-based probe for monitoring water content in a high-clay landslide soil in Austria. *Geoderma* 150, 23–31 (2009)
- [35] Sun, M., Maichen, W., Pophale, R., Liu, Y., Cai, R., Lew, C.M., Hunt, H., Deem, M.W., Davis, M.E., Yan, Y.: Dielectric constant measurement of zeolite powders by time-domain reflectometry. *Microporous Mesoporous Mater.* 123(1-3), 10–14 (2009)
- [36] Sun, S., Pommerenke, D.J., Drewniak, J.L., Chen, G., Xue, L., Brower, M.A., Koledintseva, M.Y.: A novel TDR-based coaxial cable sensor for crack/strain sensing in reinforced concrete structures. *IEEE Trans. Instrum. Meas.* 58(8), 2714–2725 (2009)
- [37] Wang, J., Stone, P.E.C., Shin, Y.J., Dougal, R.: Application of joint time-frequency domain reflectometry for electric power cable diagnostics. *IET Signal Process.* 4(4), 395–405 (2010)
- [38] Wu, S., Furse, C., Lo, C.: Noncontact probes for wire fault location with reflectometry. *IEEE Sens. J.* 6(6), 1716–1721 (2006)
- [39] Zhu, H., Hefner Jr, A.R., Lai, J.S.: Characterization of power electronics system interconnect parasitics using time domain reflectometry. *IEEE Trans. Power Electron.* 14(4), 622–628 (1999)

Chapter 2

Basic Physical Principles

*'If we knew what it was we were doing, it would not be called research, would it?'.
Albert Einstein*

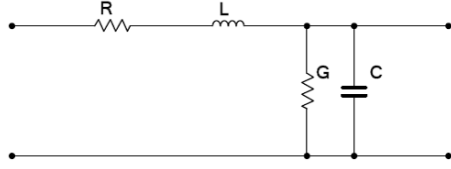
Abstract. In this chapter, the basic concepts behind broadband microwave reflectometry (BMR) are recalled. First, a brief overview of the transmission line theory is provided, and the most common electromagnetic structures are introduced. Secondly, the major parameters that are used to characterize electrical networks are introduced, and the related theoretical background is briefly discussed. Finally, a short overview on dielectric spectroscopy is provided, thus anticipating its connection with reflectometric measurements.

2.1 Transmission Line Basics

In electric circuits, when the wavelength of the propagating signal is large compared to the physical dimensions of the system, the electrical characteristics of the system, at a given time, can be assumed to be the same at all points (*lumped-element model*). On the other hand, when the physical dimensions of the system are comparable to the wavelength of the propagating signal, the dimensions of the cables, connectors and other components cannot be ignored: in such cases, it is particularly useful to model the system through transmission line (TL) segments.

TLs are typically used to transfer a signal from the generator to the load, by guiding the electromagnetic (EM) signal between two conductors [5]. A TL is a distributed-parameter network and must be described by circuit parameters that are distributed throughout its length. For the purposes of analysis, a TL can be modeled as a two-port network. The model represents the transmission line as an infinite series of two-port elementary components, each representing an infinitesimal segment of the transmission line. The elementary section of a TL can be modeled as shown in Fig. 2.1. This model includes four parameters, referred to as *primary line constants*, which are generally defined 'per unit length'. The primary line constants are the series resistance (R), the series inductance (L), the shunt conductance (G), and the shunt capacitance (C). For a uniform transmission line, the primary line constants do not change with distance along the line. These constants are used to

Fig. 2.1 Equivalent circuit model for a transmission line



define the *secondary line constants*, namely the propagation coefficient (γ) and the characteristic impedance (Z_0).

For an infinitely long line, the characteristic impedance Z_0 (which is defined as the ratio of voltage V to current I in any position) can be written as

$$Z_0 = \sqrt{\frac{R + i\omega L}{G + i\omega C}} \quad (2.1)$$

where $\omega = 2\pi f$ is the angular frequency and $i^2 = -1$.

The propagation coefficient is given by

$$\gamma = \sqrt{(R + i\omega L)(G + i\omega C)}. \quad (2.2)$$

It is useful to separate the imaginary part (β), which gives the phase-shift coefficient, from the real part (α), which gives the attenuation coefficient:

$$\alpha \cong \frac{R}{2Z_0} + \frac{GZ_0}{2} \quad (2.3)$$

$$\beta \cong \omega\sqrt{LC}. \quad (2.4)$$

For a lossless TL (i.e., when $R \cong 0$ and $G \cong 0$), Z_0 can be written simply as

$$Z_0 \cong \sqrt{L/C}. \quad (2.5)$$

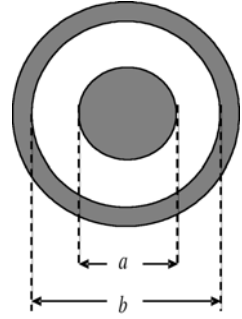
From (2.5), it can be seen that for a lossless TL, the characteristic impedance is purely resistive, although given by reactive elements (C and L). It is important to point out that this does not mean that the line is a resistance.

In the following subsections, the most common types of TLs are considered, namely coaxial, two-wire, and microstrip.

2.1.1 Coaxial Transmission Line

Coaxial lines are made of a central conductor with diameter a and a hollow outer conductor with inner diameter b . The space between the conductors is usually filled with a dielectric material: the electric and magnetic fields are confined within the

Fig. 2.2 Schematic of the cross section of a coaxial line



dielectric. Fig. 2.2 shows the schematization of the cross section of a typical coaxial line. The capacitance and the inductance per unit length are

$$C_{\text{coax}} = \frac{2\pi\epsilon}{\ln \frac{b}{a}} \quad (2.6)$$

$$L_{\text{coax}} = \frac{\mu}{2\pi} \ln \frac{b}{a} \quad (2.7)$$

where μ is the permeability of the transmission line medium; and ϵ is the dielectric permittivity of the dielectric material. Therefore, the impedance per unit length is

$$Z_{\text{coax}} = \sqrt{\frac{L_{\text{coax}}}{C_{\text{coax}}}} = \frac{1}{2\pi} \sqrt{\frac{\mu}{\epsilon}} \ln \frac{b}{a}. \quad (2.8)$$

For many materials, the permeability is equal to that of free space (i.e., $\mu \cong \mu_0 \cong 4\pi \times 10^{-7} \text{ H m}^{-1}$). Additionally, considering that $\epsilon = \epsilon_0 \epsilon_r$, where $\epsilon_0 \cong 8.854 \times 10^{-12} \text{ F m}^{-1}$ is the dielectric permittivity of free space, for practical purposes, (2.8) becomes

$$Z_{\text{coax}} = \frac{60}{\sqrt{\epsilon_r}} \ln \frac{b}{a}. \quad (2.9)$$

Typically, coaxial line can support transverse electromagnetic (TEM), transverse electric (TE), and transverse magnetic (TM) modes. In radio-frequency applications up to a few GHz, the wave propagates in the TEM mode only. However, at frequencies for which the wavelength (in the dielectric) is significantly shorter than the circumference of the cable, TE and TM modes can also propagate: when more than one mode can exist, bends and other irregularities in the cable geometry can cause power to be transferred from one mode to another. For many microwave applications, most of coaxial lines are designed to work at the TEM mode [4]. Higher-order modes are prevented from propagating, when the frequency is below the cutoff frequency, f_{c-o} :

$$f_{c-o} = \frac{c}{\pi \left(\frac{a+b}{2} \right) \sqrt{\mu_r \epsilon_r}} \quad (2.10)$$

where $c \cong 3 \times 10^8 \text{ ms}^{-1}$ is the velocity of light in free space; μ_r is the relative permeability of the transmission line medium; and ϵ_r is the relative permittivity of the dielectric material.

2.1.2 Bifilar Transmission Line

The configuration of this TL comprises a pair of parallel conducting wires separated by a constant distance (Fig. 2.3). For a bifilar transmission line [25],

$$C_{\text{bif}} = \frac{\pi \epsilon}{\ln(2D/d)} \quad (2.11)$$

$$L_{\text{bif}} = \frac{\mu}{\pi} \ln \frac{2D}{d}. \quad (2.12)$$

Hence, the characteristic impedance of a bifilar TL is given by

$$Z_{\text{bif}} = \frac{120}{\sqrt{\epsilon_r}} \ln \frac{2D}{d} \quad (2.13)$$

where ϵ_r is the relative permittivity of the dielectric between the wires/rods; D is distance between the rods; and d is the diameter of each rod.

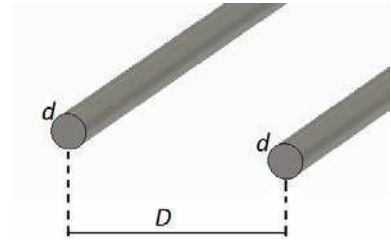
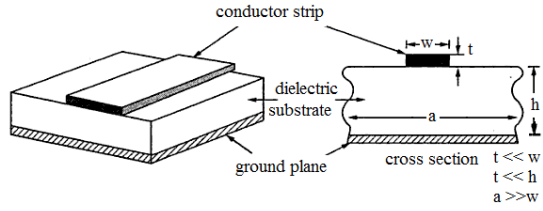


Fig. 2.3 Schematic of a two-wire line

2.1.3 Microstrip Line

The geometry of microstrip lines is very simple: a thin conductor and a ground plane separated by a low-loss dielectric material. The fabrication typically relies on printed circuit techniques. The use of a substrate with a high dielectric constant reduces the fringing field in the air region above the conductor. Because the electric field lines remain partially in the air and partially in the substrate, microstrip lines do not support pure TEM mode, but a quasi-TEM mode [3]. For $0.05 < w/h < 1$, the characteristic impedance is given by

Fig. 2.4 Schematic of a microstrip line



$$Z_{ms} = \frac{120\pi}{\sqrt{\epsilon_{\text{eff}}}} \ln \left[\frac{8h}{w} + \frac{w}{4h} \right] \quad (2.14)$$

whereas for $1 < w/h < 20$

$$Z_{ms} = \frac{120\pi}{\sqrt{\epsilon_{\text{eff}}}} \left[\frac{w}{h} + 1.393 + 0.667 \ln \left(\frac{w}{h} \right) + 1.49 \right]^{-1} \quad (2.15)$$

where ϵ_{eff} is the effective permittivity; w is the width of the microstrip; and h is the thickness of the substrate [26].

2.2 Reflected Waves

Let us consider a Z_0 -impedance TL, terminated with a generic load impedance, Z_L (Fig. 2.5). When Z_L does not match Z_0 , part of the incident wave is absorbed by the load, and the rest is reflected along the line.

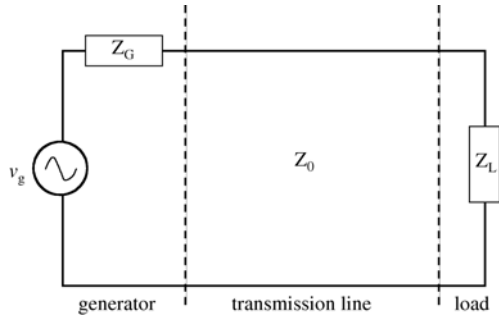


Fig. 2.5 TL connected between the generator and the load

At any point on the line, the reflected voltage is given by [25]

$$V_R = \Gamma V_I \quad (2.16)$$

where Γ is the reflection coefficient and V_i is the incident voltage. Γ is given by

$$\Gamma = \frac{Z_L - Z_0}{Z_L + Z_0} \quad (2.17)$$

with $|\Gamma| \leq 1$. By rearranging (2.17)

$$Z_L = Z_0 \frac{1 + \Gamma}{1 - \Gamma} \quad (2.18)$$

Generally, Γ is a complex quantity and it is often defined through magnitude (ρ) and angle phase (ϕ):

$$\Gamma = \rho \angle \phi. \quad (2.19)$$

It is worth noting that usually both Γ and ρ are referred to as reflection coefficient; however, the former is a complex quantity, whereas the latter is scalar. As long as there is no change in the impedance of the TL, the magnitudes of the incident and reflected voltages do not change with position; therefore, ρ does not change with position. On the other hand, the phase of the reflection coefficient changes as position changes [29].

When a sinusoidal signal propagates down a transmission line and the termination of the line is not matched, the incident voltage and the reflected voltage create a typical interference pattern. The envelope of the sinusoidal voltage will maintain a constant shape (*standing wave*). The magnitude varies with distance, but the voltage at each point on the line varies sinusoidally. The voltage standing wave ratio (VSWR) is the ratio of the maximum V_{\max} and minimum V_{\min} of the envelope:

$$VSWR = \frac{V_{\max}}{V_{\min}}. \quad (2.20)$$

The $VSWR$ is related to the magnitude of the complex reflection coefficient by the following equation:

$$VSWR = \frac{1 + |\Gamma|}{1 - |\Gamma|}. \quad (2.21)$$

$VSWR$ is greater than or equal to one: $VSWR = 1$ when no mismatch occurs; $VSWR \rightarrow \infty$ for an open or short circuit.

2.3 Characteristic Parameters of Electrical Networks

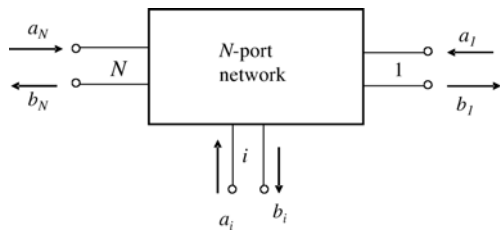
An electrical network is typically used to indicate a circuit (either single or multi-component) or a generic TL. Generally, an electrical network is represented as a black box with input and output terminals, and the analysis of the network is done at the terminals. A network can be characterized through different parameters that relate current to voltage; the most common parameters are summarized in Table 2.3. When dealing with multi-port networks, it is particularly useful to represent network parameters through matrices. The choice of the most suitable representation depends not only on which the characteristics of interest are, but also on the frequency range of analysis and, obviously, on the available measurement instrumentation.

Table 2.1 Typical parameters used for describing electrical networks

symbol	matrix
ABCD*	transmission
\bar{Z}	impedance
\bar{Y}	admittance
H*	hybrid
G*	inverse hybrid
S	scattering

* Cannot be used for networks with more than 2 ports.

At high frequencies, the influence of parasitics (i.e., capacitances, cable inductance, undesired coupling effects) becomes more significant; hence, it becomes increasingly difficult to measure voltages and currents. In this case, it is preferred to measure power, and if necessary, to successively extrapolate the other parameters of interest. In this regard, scattering parameters (*S-parameters*) are particularly convenient; in fact, *S-parameters* relate to signal flow rather than to voltages and currents directly. In particular, the ‘measured quantities’ are traveling waves.

**Fig. 2.6** Schematization of an *N*-port network

Considering an *N*-port network (Fig. 2.6), scattering variables at the generic port *n* are defined in terms of the port voltage V_n , port current I_n , and a normalization impedance Z_0 . The voltage and the current can be synthesized by an incident scattering variable, a_n , and a reflected scattering variable b_n , given by

$$a_n = \frac{V_n}{2\sqrt{Z_0}} + \frac{I_n\sqrt{Z_0}}{2}, \quad (2.22)$$

$$b_n = \frac{V_n}{2\sqrt{Z_0}} - \frac{I_n\sqrt{Z_0}}{2}. \quad (2.23)$$

The scattering parameters are measured in terms of a_n and b_n . For a *N*-port network, there are N^2 scattering parameters, S_{ij} , with $i, j = 1, \dots, N$.

The *S-parameters* where $i = j$ are referred to as reflection scattering parameters. They are practically measured as the ratio between the outgoing and incoming wave

at the i^{th} port, when a matched generator is connected to the i^{th} port and all the other ports are terminated with a matched load (i.e., $a_j = 0, \forall j \neq i$) [30]:

$$S_{ii} = \frac{b_i}{a_i} \Big|_{a_j=0, \forall j \neq i}. \quad (2.24)$$

The terms S_{ij} are referred to as transmission scattering parameters. They are measured as the ratio of the outgoing wave at the i^{th} port (b_i) and the incoming wave at the j^{th} port (a_j) when a matched generator is connected at port j and the other ports are connected to a matched load:

$$S_{ij} = \frac{b_i}{a_j} \Big|_{a_i=0, \forall i \neq j}. \quad (2.25)$$

Often, the matrix notation is used

$$\begin{bmatrix} b_1 \\ b_2 \\ \dots \\ b_N \end{bmatrix} = \begin{bmatrix} S_{11} & S_{12} & \dots & S_{1N} \\ S_{21} & \dots & \dots & \dots \\ \dots & \dots & \dots & \dots \\ S_{N1} & \dots & \dots & S_{NN} \end{bmatrix} \times \begin{bmatrix} a_1 \\ a_2 \\ \dots \\ a_N \end{bmatrix} \quad (2.26)$$

For a reciprocal network, the scattering matrix is symmetrical, i.e. $S_{mn} = S_{nm}$ ($m, n = 1, 2, \dots, N$). As can be seen from the previous equations, to measure the generic scattering parameter S_{ij} , which involves ports i and j , the remaining ports have to be terminated with matched loads¹ (rather than with short or open circuits, as must be done with other network parameters). This is great advantage of characterizing electrical networks through *S-parameters*; in fact, at microwave frequencies, open and short circuits are more difficult to implement and may lead to instability (severe distortion or oscillation may occur) [29].

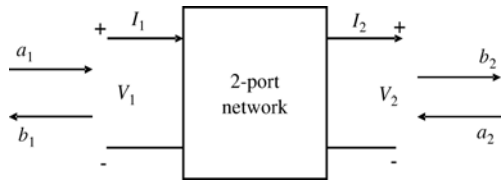


Fig. 2.7 Two-port network scheme

Fig. 2.7 shows the schematic of a two-port network: I_1 and I_2 are the currents at the terminals; V_1 and V_2 are the voltages at the terminals; and a and b are the traveling waves. The square of the coefficient represents the power: $|a_1|^2$ and $|b_1|^2$ can be considered as the power entering *port 1* and exiting *port 1*, respectively. For two-port networks, the system can be modeled by two equations:

¹ Clearly, when performing reflection measurements (i.e., S_{ii}), all ports except the i^{th} port should be terminated with a matched impedance.

$$b_1 = S_{11}a_1 + S_{12}a_2, \quad (2.27)$$

$$b_2 = S_{21}a_1 + S_{22}a_2. \quad (2.28)$$

The scattering parameters are therefore measured as

$$S_{11} = \frac{b_1}{a_1} \Big|_{a_2=0}, \quad (2.29)$$

$$S_{21} = \frac{b_2}{a_1} \Big|_{a_2=0}, \quad (2.30)$$

$$S_{12} = \frac{b_1}{a_2} \Big|_{a_1=0}, \quad (2.31)$$

$$S_{22} = \frac{b_2}{a_2} \Big|_{a_1=0}. \quad (2.32)$$

The potential of *S-parameters* for monitoring and diagnostics purposes will be clearer in the following chapters. In fact, it will be shown that, when the *system to be monitored* can be considered as an electrical network, the *S-parameters* of the system can disclose useful information on the system itself. In particular, the scattering parameters can be used to extrapolate the dielectric characteristics of the SUT. The retrieved information, although related to the dielectric behavior, may be appropriately associated with several quantitative and/or qualitative properties of the sample.

2.4 Reflectometry Measurements for Dielectric Spectroscopy

Dielectric spectroscopy, also called impedance spectroscopy, measures the dielectric properties of a medium as a function of frequency. It is based on the interaction of an external field with the electric dipole moment of the sample, often expressed by permittivity. This technique measures the impedance of a system over a range of frequencies, and, therefore, the frequency response of the system, including the energy storage and dissipation properties. Almost any physico-chemical system possesses energy storage and dissipation properties that can be analyzed through dielectric spectroscopy.

There are several approaches that can be used to measure the dielectric properties of materials, such as open-ended probe technique, free-space transmission technique, cavity resonant systems, time domain reflectometry, and so on. An overview of some of the most common methods for measuring dielectric properties of materials can be found in [27].

In particular, dielectric spectroscopy performed through microwave reflectometry, has gained enormous popularity over the past few years and is now being widely employed in a wide variety of scientific fields that go from food analysis [20] to biomedical applications [24, 19, 12]. As will be detailed in the following

chapters, for microwave reflectometry-based dielectric spectroscopy of materials, either the direct frequency domain (FD) approach or the time domain/frequency domain (TD/FD) combined approach can be adopted [28].

2.4.1 Dielectric Relaxation Models

Materials can be classified according to their dielectric permittivity. The dielectric behavior of a material is suitably described by the frequency-dependent complex relative permittivity, $\epsilon_r^*(f)$, which can be written as follows [4]:

$$\epsilon_r^*(f) = \epsilon_r'(f) - i \left(\epsilon_r''(f) + \frac{\sigma_0}{2\pi f \epsilon_0} \right) \quad (2.33)$$

where $i^2 = -1$, $\epsilon_0 \cong 8.854 \times 10^{-12} \text{ Fm}^{-1}$ is the dielectric permittivity of free space, f is the frequency, $\epsilon_r'(f)$ describes energy storage, $\epsilon_r''(f)$ accounts for the dielectric losses, and σ_0 is the static electrical conductivity (which is related to the ionic losses). Generally, when $(\sigma_0/2\pi f \epsilon_r') \gg 1$, the material can be considered a good conductor. On the other hand, when $(\sigma_0/2\pi f \epsilon_r') \ll 1$, the material is considered a dielectric (i.e., lossless or low-loss material). Materials with a large amount of loss inhibit the propagation of electromagnetic waves. Those that do not fall under either limit are considered to be general media. A perfect dielectric is a material that has no conductivity, thus exhibiting only a displacement current.

The dielectric relaxation refers to the relaxation response of a dielectric medium to an external electric field of microwave frequencies. This relaxation is often described, in terms of dielectric permittivity, through the so-called *relaxation models*. Fig. 2.8 shows a schematization of typical relaxation phenomena.

There are several mathematical models (obtained either theoretically or empirically) that are used to describe the dielectric properties of materials.

For example, for pure polar materials, the equation known as Debye model describes the dielectric permittivity [9]:

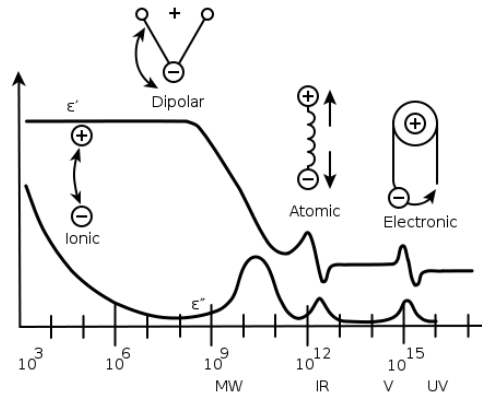


Fig. 2.8 Generic dielectric permittivity spectrum over a wide range of frequencies. The figure shows the main processes that occur: ionic and dipolar relaxation, and atomic and electronic resonances at higher energies [1]

$$\epsilon_r^*(f) = \epsilon_\infty + \frac{\epsilon_s - \epsilon_\infty}{1 + \left(i \frac{f}{f_{\text{rel}}}\right)} \quad (2.34)$$

where ϵ_∞ is the dielectric constant at frequency so high that molecular orientation does not have time to contribute to polarization (i.e., at infinite frequency) [7]; ϵ_s is the static dielectric permittivity; f_{rel} is the relaxation frequency (defined as the frequency at which the permittivity is $(\epsilon_s + \epsilon_\infty)/2$) [16]; and f is the frequency.

As a matter of fact, only few materials of interest behave as pure polar materials with a single relaxation frequency; therefore, other models have been developed to describe more accurately the dielectric behavior of materials [7]. The Cole-Cole model, with symmetric distribution of relaxation times, is described through the following equation:

$$\epsilon_r^*(f) = \epsilon_\infty + \frac{\epsilon_s - \epsilon_\infty}{1 + \left(i \frac{f}{f_{\text{rel}}}\right)^{(1-\beta)}} \quad (2.35)$$

where β is a parameter that describes the spread in relaxation frequency ($0 \leq \beta \leq 1$) [10, 17]. When $\beta = 0$, the Cole-Cole model reduces to the Debye model.

A further generalization of the Debye model is given by the Havriliak-Negami formula [2, 14]:

$$\epsilon_r^*(f) = \epsilon_\infty + \frac{\epsilon_s - \epsilon_\infty}{\left[1 + \left(i \frac{f}{f_{\text{rel}}}\right)^{(1-\beta)}\right]^\alpha} \quad (2.36)$$

where α describes the broadness of the permittivity spectra.

Finally, the Cole-Davidson model with asymmetric distribution of relaxation times follows for $\beta = 0$ and for $0 < \alpha < 1$ [8]:

$$\epsilon_r^*(f) = \epsilon_\infty + \frac{\epsilon_s - \epsilon_\infty}{\left[1 + \left(i \frac{f}{f_{\text{rel}}}\right)\right]^\alpha} \quad (2.37)$$

When the static electrical conductivity is not negligible, an additional term must be included in the equations above; therefore, for example, the Cole-Cole model described by (2.35) becomes

$$\epsilon_r^*(f) = \left\{ \epsilon_\infty + \frac{\epsilon_s - \epsilon_\infty}{\left[1 + \left(i \frac{f}{f_{\text{rel}}}\right)^{(1-\beta)}\right]} \right\} - i \frac{\sigma_0}{2\pi f \epsilon_0} \quad (2.38)$$

The five parameters are referred to as Cole-Cole parameters: they are different for each material and they define its spectral signature. The Cole-Cole relaxation model has proved suitable in describing relaxation phenomena of various materials, especially for lossy media [6, 9], and for a wide number of materials (e.g., concrete, paper, petrochemicals, and even blood) [13, 15].

In particular, the estimation of the Cole-Cole parameters of foods (e.g., egg white, butter, bacon, etc.) has received considerable attention, thanks to the possibility of associating the dielectric parameters to the quality status of the products/materials [23, 22, 21].

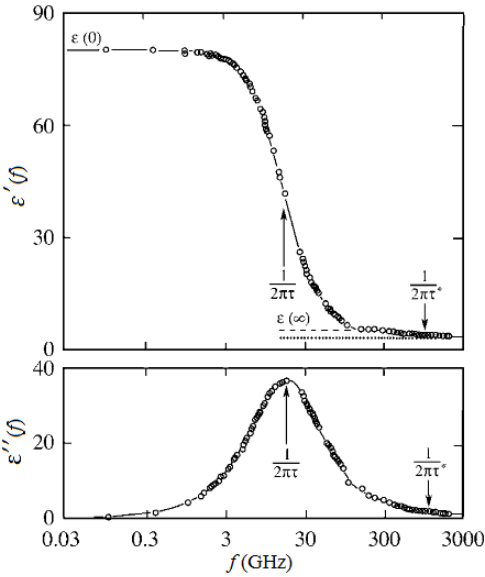
As a matter of fact, the evaluation of such parameters is not always a straightforward task, especially when dealing with complex materials, such as mixtures, powders, etc..

For the sake of example, Table 2.2 shows the Cole-Cole parameters for some common liquids, as reported in [11]. The Cole-Cole parameters of these and of other liquids are typically used as reference for calibrating and validating experimental setups for dielectric measurements. Fig. 2.9 shows the complex dielectric spectrum of water, as reported in [18].

Table 2.2 Values of the Cole-Cole parameters for some common liquids, as reported in [11]

material	ϵ_s	ϵ_∞	$\tau = 1 / (2\pi f_r)$ (ps)	β
air	1.0005			
chloroform	4.82	2.28	6.25	
ethyl-acetate	6.04	2.48	4.4	0.06
toluene	2.40	2.25	7.34	

Fig. 2.9 Complex dielectric spectrum of water at 20°C. The dashed line indicates the extrapolated high frequency permittivity, ϵ_∞ , of the principal relaxation of water. The dotted line shows the extrapolated high frequency permittivity of an additional relaxation, with relaxation frequency $1/2\pi\tau^{-1}$, around 1000 GHz [18]



References

- [1] Basics of measuring the dielectric properties of materials. Hewlett Packard Application Note 1217-1, USA (1992)
- [2] Axelrod, N., Axelrod, E., Gutina, A., Puzenko, A., Ishai, P.B., Feldman, Y.: Dielectric spectroscopy data treatment: I. frequency domain. *Meas. Sci. Technol.* 15(4), 755–764 (2004)
- [3] Bagad, V.S.: Microwave engineering. Technical Publications Pune, Pune (2009)
- [4] Chen, L.F., Ong, C.K., Neo, C.P., Varadan, V.V., Varadan, V.K.: Microwave electronics: measurement and materials characterization. John Wiley & Sons, UK (2004)
- [5] Chen, W.: The electrical engineering handbook. Elsevier Academic Press, Burlington (2005)
- [6] Cole, K.S., Cole, R.H.: Dispersion and absorption in dielectrics: I. alternating current characteristics. *J. Chem. Phys.* 9(4), 341–351 (1941)
- [7] Datta, A.K., Anantheswaran, R.C.: Handbook of microwave technology for food application. CRC Press, New York (2001)
- [8] Davidson, D.W., Cole, R.H.: Dielectric relaxation in glycerol, propylene glycol, and n-propanol. *J. Chem. Phys.* 19(12), 1484–1490 (1951)
- [9] Debye, P.J.W.: Polar molecules. The Chemical Catalog Company Inc., New York (1929)
- [10] Dyer, S.A.: Survey of instrumentation and measurement. John Wiley & Sons, USA (2001)
- [11] Folgero, K., Friiso, T., Hilland, J., Tjomsland, T.: A broad-band and high-sensitivity dielectric spectroscopy measurement system for quality determination of low-permittivity fluids. *Meas. Sci. Technol.* 6(7), 995–1008 (1995)
- [12] Kao, H.P., Shwedyk, E., Cardoso, E.R.: Correlation of permittivity and water content during cerebral edema. *IEEE Trans. Biomed. Eng.* 46(9), 1121–1128 (1999)
- [13] Hager III, N.E., Domszy, R.C.: Monitoring of cement hydration by broadband time-domain-reflectometry dielectric spectroscopy. *J. Appl. Phys.* 96(9), 5117–5128 (2004)
- [14] Havriliak, S., Negami, S.: *Polymer* 8, 161–201 (1967)
- [15] Hayashi, Y., Oshige, I., Katsumoto, Y., Omori, S., Yasuda, A., Asami, K.: Temporal variation of dielectric properties of preserved blood. *Phys. Med. Biol.* 53(1), 295–304 (2008)
- [16] Huisman, J.A., Bouten, W., Vrugt, J.A., Ferrè, P.A.: Accuracy of frequency domain analysis scenarios for the determination of complex permittivity. *Water Resour. Res.* 40 (2004)
- [17] Jones, S.B., Or, D.: Frequency domain analysis for extending time domain reflectometry water content measurement in highly saline soils. *Soil Sci. Soc. Am J.* 68, 1568–1577 (2004)
- [18] Kaatz, U., Feldman, Y.: Broadband dielectric spectrometry of liquids and biosystems. *Meas. Sci. Technol.* 17(2), R17–R35 (2006)
- [19] Mehta, P., Chand, K., Narayanswamy, D., Beetner, D.G., Zoughi, R., Stoecker, W.V.: Microwave reflectometry as a novel diagnostic tool for detection of skin cancers. *IEEE Trans. Instrum. Meas.* 55(4), 1309–1316 (2006)
- [20] Miura, N., Yagihara, S., Mashimo, S.: Microwave dielectric properties of solid and liquid foods investigated by time-domain reflectometry. *J. Food Sci.* 68(4), 1396–1403 (2003)
- [21] Nelson, S.O., Bartley Jr, P.G.: Measuring frequency- and temperature-dependent permittivities of food materials. *IEEE Trans. Instrum. Meas.* 51, 589–592 (2002)

- [22] Nelson, S.O., Trabelsi, S.: Dielectric spectroscopy of wheat from 10 MHz to 1.8 GHz. *Meas. Sci. Technol.* 17(8), 2294–2298 (2006)
- [23] Nelson, S.O., Guo, W., Trabelsi, S., Kays, S.J.: Dielectric spectroscopy of watermelons for quality sensing. *Meas. Sci. Technol.* 18(7), 1887–1892 (1999)
- [24] Popovic, D., McCartney, L., Beasley, C., Lazebnik, M., Okoniewski, M., Hagness, S.C., Booske, J.H.: Precision open-ended coaxial probes for in vivo and ex vivo dielectric spectroscopy of biological tissues at microwave frequencies. *IEEE Trans. Microw. Theory Tech.* 53(5), 1713–1722 (2005)
- [25] Roddy, D.: *Microwave technology*, 2nd edn. Prentice-Hall, Englewood Cliffs (1986)
- [26] Roussy, G., Pearce, J.A.: *Foundations and industrial applications of microwaves and radio frequency fields*. J. Wiley & Sons Inc., Chichester (1995)
- [27] Venkatesh, M.S., Raghavan, G.S.V.: An overview of microwave processing and dielectric properties of agri-food materials. *Biosyst. Eng.* 88(1), 1–18 (2004)
- [28] de Winter, E.J.G., van Loon, W.K.P., Esveld, E., Heimovaara, T.J.: Dielectric spectroscopy by inverse modelling of time domain reflectometry wave forms. *J. Food Eng.* 30(3–4), 351–362 (1996)
- [29] Witte, R.A.: *Spectrum & network measurements*. Noble Publishing Corporation, Atlanta (1993)
- [30] Zhang, K., Li, D.: *Electromagnetic theory for microwaves and optoelectronics*, 2nd edn. Springer, Heidelberg (2008)

Chapter 3

Broadband Reflectometry: Theoretical Background

*'A scientist's aim in a discussion with his colleagues is not to persuade, but to clarify'.
Leo Szilard*

Abstract. In this chapter, the basic approaches of broadband microwave reflectometry are described in detail. More specifically, time domain reflectometry (TDR) and frequency domain reflectometry (FDR) are presented and the involved instrumentation is fully described. Successively, the FDR/TDR combined approach is described in detail: this approach can help exploit the benefits of both TDR and FDR, without necessarily employing two different measurement setups. Additionally, since the sensing element (or probe) plays a major role in all the aforementioned approaches, a comprehensive description of its design and of the corresponding performance is given. Finally, the basic principles leading to the possibilities of enhancing accuracy in BMR measurements are presented.

3.1 Broadband Microwave Reflectometry: Theoretical Background

Broadband microwave reflectometry (BMR) is a powerful technique that can be effectively employed for a number of practical applications; in particular, the high versatility, the real-time response and the potential for practical implementation have contributed to the success of microwave reflectometry for monitoring purposes.

Generally, in BMR, a low-power electromagnetic signal is propagated into the system under test (SUT): the analysis of the reflected signal along with specific data-processing are used to retrieve the desired information on the SUT [32].

Two main elements are involved in BMR measurements:

1. the instrument for generating/receiving the electromagnetic (EM) signal, and
2. the measurement cell, which includes the sensing element (or probe) and the SUT.

Microwave reflectometry-based measurements can be performed either in time domain (time domain reflectometry - TDR) or in frequency domain (frequency domain

reflectometry - FDR). Depending on the specific application, one approach may be more suitable than the other.

TDR instrumentation is usually less expensive than instruments operating in frequency domain. Nevertheless, instruments operating directly in frequency domain, such as vector network analyzers (VNAs), despite being more expensive, usually provide higher measurement accuracy. An optimal trade-off (in terms of low cost and measurement accuracy), can be achieved through a time domain/frequency domain (TD/FD) combined approach: in this case, measurements are carried out, for example, in TD and the corresponding FD-information is retrieved through appropriate processing of the acquired data, thus discovering additional information [11, 36].

It is worth pointing out that a substantial advantage in operating in FD relates to the possibility of performing calibration procedures (as will be detailed in Sect. 3.4), thus enhancing the final measurement accuracy. This procedure can be implemented in the TD/FD approach; consequently, the combination of the two approaches is highly regarded as a powerful tool for guaranteeing at the same time low cost of the setup and adequate measurement accuracy. This aspect, along with the detailed description of the specific implemented procedure, will be addressed in Sect. 3.4. In the following subsections, the basic principles behind all the three approaches are recalled, and pros and cons are discussed.

3.2 Time Domain Reflectometry (TDR)

In TDR measurements, the EM stimulus is usually a step-like signal that propagates along the probe, through the SUT. The basic block diagram of a typical TDR system is shown in Fig. 3.1. It consists of a step-pulse generator, a sampling scope, and a signal analyzer. The step generator produces a positive-going incident wave that is applied to the SUT. The step travels down the transmission line at the velocity of propagation of the line. Any impedance variation causes the partial reflection of the propagating signal. If the load impedance is equal to the characteristic impedance of the line, no wave is reflected, and the oscilloscope displays only the incident voltage step. If a mismatch exists at the load, part of the incident wave is reflected

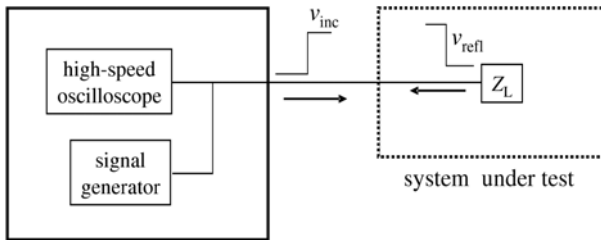


Fig. 3.1 Functional block diagram for a time domain reflectometer [4]

[4]. The reflected signal is acquired by the oscilloscope, and its voltage amplitude is displayed as a function of time (or as a function of the traveled electric distance).

The ratio between the amplitude of the reflected signal, $v_{\text{refl}}(t)$, and the amplitude of the generated signal, $v_{\text{inc}}(t)$, gives the value of the reflection coefficient in time domain, $\rho(t)$ [10]:

$$\rho(t) = \frac{v_{\text{refl}}(t)}{v_{\text{inc}}(t)} \quad (3.1)$$

where $-1 \leq \rho(t) \leq +1$.

It is important to point out that, most often, the oscilloscope functionality is integrated with the signal generator within one single instrument (which, as will be detailed later in this chapter, can be either portable or benchtop).

Clearly, the behavior of $\rho(t)$ is strictly associated with the impedance variations along the electrical path traveled by the electromagnetic (EM) signal. As an example, Fig. 3.2 shows the schematization of the TDR waveforms observed when the SUT exhibits purely-resistive behavior.

If an increase of impedance is encountered (i.e., $Z_L > Z_0$), then a positive step is observed and the reflection coefficient will be positive. Conversely, if a decrease of impedance is encountered (i.e., $Z_L < Z_0$), then a negative step is observed and the reflection coefficient will be negative. In particular, if the impedance of the load equals the characteristic impedance of the line (i.e., $Z_L = Z_0$), no wave will be reflected ($\rho = 0$); hence, the TDR display on the scope is a flat line. If an open circuit is encountered, then the reflected voltage will equal the generated voltage and the reflection coefficient will be $+1$. If a short circuit is encountered, the reflection coefficient will be -1 . It goes without saying that the actual value of an ‘unknown’ Z_L may be inferred from the reflection coefficient displayed by the TDR unit.

Also of interest are the reflections produced by complex load impedances. Four basic examples of these reflections are shown in Fig. 3.3, where the incident step voltage is indicated as E_i . A direct analysis (in TD) of the reported waveforms involves evaluating the reflected voltage at $t = 0$ and at $t = \infty$, and assuming any transition between these two values to be exponential.

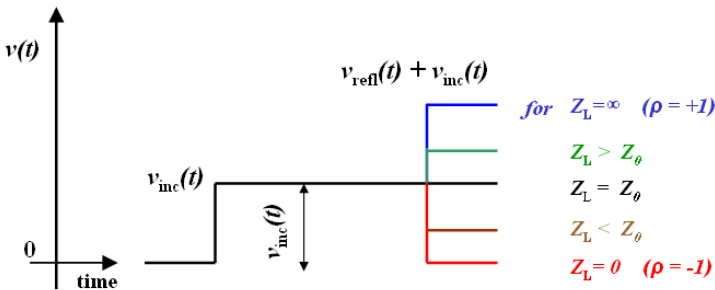


Fig. 3.2 Schematization of TDR waveforms for purely-resistive terminations

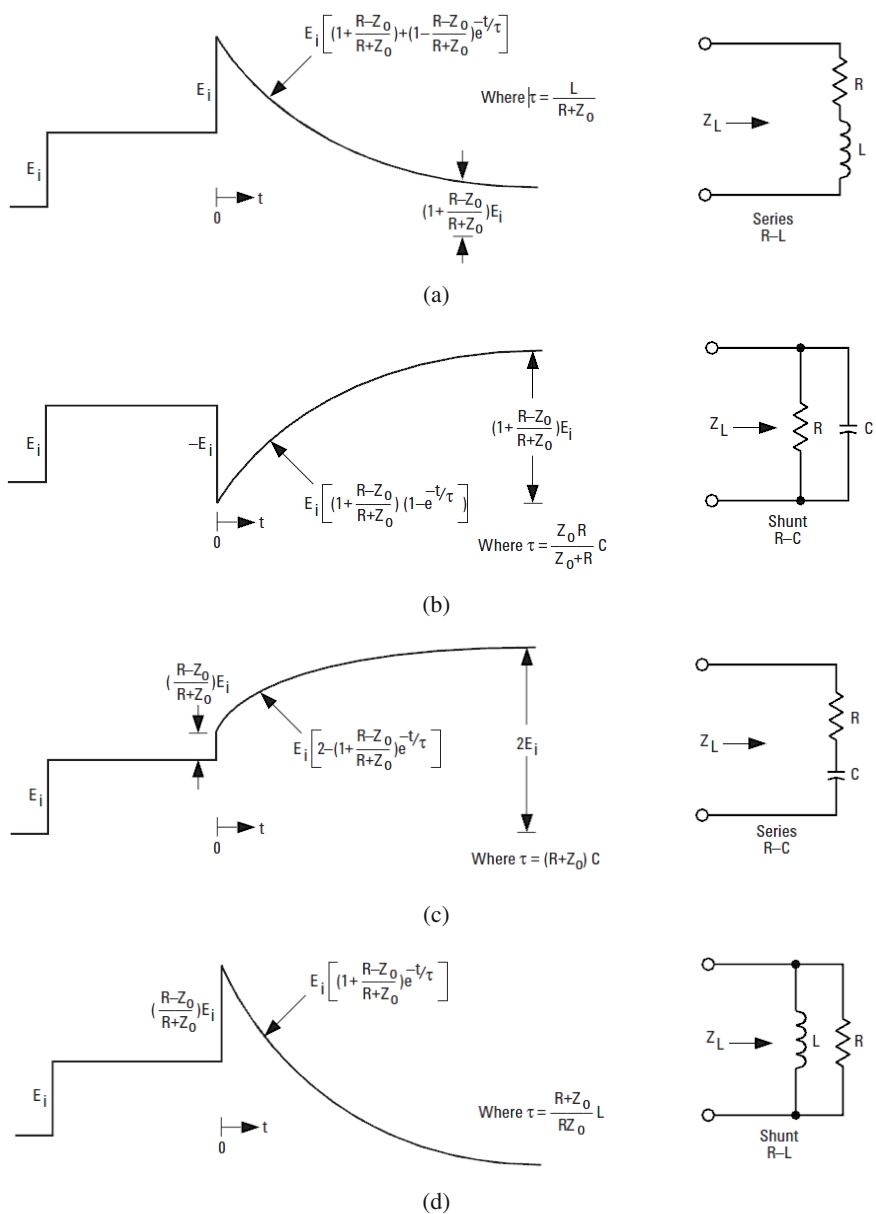


Fig. 3.3 TDR waveforms when reactive components are present [4]. The incident step signal is indicated as E_i

For the sake of example, let us consider the series R - L case [4]. Also, for simplicity, let us assume that the time is zero when the reflected wave arrives back at the monitoring point.

At $t = 0$, the reflected voltage is $+E_i$. This is because the inductor will not accept a sudden change in current: it initially behaves like an infinite impedance; hence, at $t = 0$, ρ will be unit.

Successively, the current in L builds up exponentially and its impedance drops toward zero. Therefore, at $t = \infty$, $E_r(t)$ is determined only by the value of R :

$$\rho = \frac{R - Z_0}{R + Z_0} \quad (3.2)$$

The exponential transition of $E_r(t)$ has a time constant (τ) determined by the effective resistance seen by the inductor. Since the output impedance of the transmission line is Z_0 , the inductor sees Z_0 in series with R :

$$\tau = \frac{L}{R + Z_0} \quad (3.3)$$

A similar analysis can be carried out for the other three cases reported in Fig. 3.3.

It must be pointed out that an in-depth analysis of the impedance characteristics of the SUT should rely also on a FD approach (in particular, through the evaluation of the reflection scattering parameter). However, as seen from Fig. 3.3, the TDR waveforms can provide a concrete idea on the impedance-behavior of the SUT.

This approach is particularly useful for TDR-based individuation of faults along cables. In fact, faults do show specific impedance behavior, whose meaning can be inferred directly from the TDR waveforms.

3.2.1 Typical TDR Measurements

When the TDR signal propagates along a transmission line, impedance mismatches cause the reflection of a portion of the signal. The TDR signal's propagation velocity, v , is related to the relative dielectric permittivity (ϵ_r) of the medium, which is assumed to be lossless or at least with negligible conductivity, and to the relative magnetic permeability (μ_r), which is equal to 1 for most materials [4]:

$$v = \frac{c}{\sqrt{\epsilon_r \mu_r}} \quad (3.4)$$

where c is the speed of light in free space ($c \cong 3 \times 10^8 \text{ m s}^{-1}$).

For the sake of example, let us consider a typical three-rod probe, whose electrodes have length L . A typical TDR waveform for such a probe, immersed in a generic homogeneous dielectric, is represented in Fig. 3.4. The analysis of TDR waveform directly leads to the evaluation of L_{app} (also called electric distance), which can be directly associated to the dielectric characteristic of the medium. In

fact, L_{app} can be considered as the distance that would be traveled by the EM signal, in the same interval of time, if the signal were propagating at a speed c .

Typically, in TDR analysis, the apparent distance is evaluated through the individuation of the beginning and end of the probe, thus it can be associated to the physical length, L , through the following equation:

$$L_{\text{app}} = \sqrt{\epsilon_{\text{app}}} L = \frac{ct_t}{2} \quad (3.5)$$

where t_t is the travel time (round-trip time taken by the signal to travel between the beginning and end points), and ϵ_{app} is referred to as apparent dielectric permittivity of the material in which the probe is inserted [4].

A more rigorous expression for ϵ_{app} is given by the following equation [37]:

$$\epsilon_{\text{app}}(f) = \frac{\epsilon_r'(f)}{2} \left(1 + \sqrt{1 + \left\{ \frac{[\epsilon_r''(f) + \frac{\sigma_0}{2\pi f \epsilon_0}]}{\epsilon_r'(f)} \right\}^2} \right) \quad (3.6)$$

where $\epsilon_0 \cong 8.854 \times 10^{-12} \text{ Fm}^{-1}$ is the dielectric permittivity of free space, f is the frequency, $\epsilon_r'(f)$ describes energy storage, $\epsilon_r''(f)$ accounts for the dielectric losses, and σ_0 is the static electrical conductivity.

However, when dealing with low-loss materials, the imaginary part of the complex permittivity can be neglected. Additionally, considering low dispersive materials, the dependence of $\epsilon_r'(f)$ on frequency can be considered negligible. Under these circumstances, $\epsilon_{\text{app}}(f)$ can be considered approximately constant:

$$\epsilon_{\text{app}}(f) \cong \epsilon_r'(f) \cong \text{const.} \quad (3.7)$$

On the basis of the above described theory, TDR-based dielectric measurements simply rely on the individuation of the points corresponding to the beginning and to the end of the probe. To individuate these two points in the TDR waveform, different approaches based on the so-called tangent method can be used [24, 41]. However, as can be intuitively deduced from Fig. 3.4, L_{app} can be easily evaluated through the derivative of the TDR waveform, which typically exhibits prominent peaks in correspondence of the probe-beginning and probe-end sections. Indeed, not only is this ‘derivative method’ simple and quick, but it also proves particularly advantageous when significant impedance changes are masked by other impedance variations (for example, by the transition coaxial cable/rods in Fig. 3.4), as will be clarified later in this book.

3.2.2 Typical TDR Instrumentation

As aforementioned, the pivotal components of a TDR instrument are a high-bandwidth oscilloscope and a high-speed pulse generator: the characteristics of

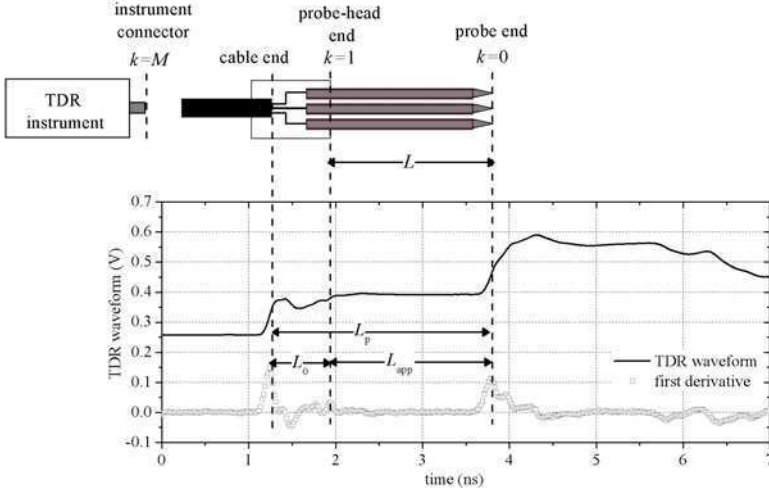


Fig. 3.4 Typical TDR waveform (black curve) and corresponding first derivative (red curve) for a 30 cm-long three-rod probe in air, obtained through a Tektronix TDR80E04. The amplitude of the incident step-like signal is 0.25 V. The first derivative of the TDR waveform emphasizes the impedance variations. The section $k = 1$ indicates where the sensing portion of the considered probe begins

these two components have the major influence on the performance of the instrument. In particular, the frequency content of the signal, f_B , is approximately given by the following equation:

$$f_B \cong \frac{0.35}{t_r} \quad (3.8)$$

where t_r is the rise-time of the generated step signal¹.

A higher bandwidth of the signal makes the TDR measurements significant in a wider frequency range; this concept will be detailed in Sect. 3.4, when the TDR/FDR combined approach is described. The lower the rise-time of the generated signal, the more sophisticated (and costly) is the TDR instrument.

It is worth mentioning that the minimum spatial resolution, ΔL_{\min} , is related to the rise-time of the TDR step-like signal, t_r [10]:

$$\Delta L_{\min} = \frac{t_r c}{2\sqrt{\epsilon_{\text{app}}}}. \quad (3.9)$$

¹ Equation (3.8) is a simplification of $f_B \cong \frac{\ln(0.9/0.1)}{2\pi t_r}$, which is an expression typically used in electrical engineering to describe the frequency characteristics of low-pass filters. This expression remains accurate when the energy contained in the voltage pulse is equally distributed across the frequency bandwidth and when there is no significant dispersion [31].

Indeed, there is a wide availability of TDR units on the market: ranging from low-cost portable units to high-performance benchtop instrument.

Most of the experimental results reported in this book were obtained using two TDR instruments with different characteristics, namely the Hyperlabs 1500 (HL1500) and/or the Tektronix TDR80E04.

The Hyperlabs 1500 is a low-cost portable TDR unit (see Fig. 3.5) [7]. The rise time of the generated signal is approximately 200 ps, which corresponds to a frequency bandwidth of around 1.7 GHz. The incident pulse amplitude is 250 mV and the pulse duration is 14 μ s. The maximum number of acquisition points, for the selected time window, is 2048. The HL1500 is a single-port instrument; the output has a BNC connector and the output impedance is 50 Ω . The HL1500 can be controlled through a computer. This TDR instrument supports multiplexer, thus allowing the simultaneous connection of several probes to a single TDR unit. This feature is particularly useful for practical purposes (e.g., for monitoring along the production lines, for geotechnical analysis of soils, etc.), as it would lower the implementation costs.



Fig. 3.5 Picture of the HL1500 portable TDR instrument [7]

As for the Tektronix TDR80E04, it is a highly sophisticated TDR module that is mounted on the Tektronix Digital Serial Analyzer DSA8200 (a benchtop instrument) shown in Fig. 3.6. The TDR incident step signal has a rise-time of approximately 23.5 ps, thus the frequency content is about 15 GHz. The incident pulse amplitude is ± 250 mV and its duration is approximately 2.65 μ s. The maximum number of acquisition points, for the selected time window, is 4000. The TDR80E04 has two ports (as it also allows transmission measurements to be performed). The output ports have 3.5 mm connectors.

These two specific instruments were chosen, because they are representative of two categories of TDR instrumentation. The HL1500 is a compact and rugged TDR unit, and this make it particularly useful for in situ applications. On the other hand, the TDR80E04 is a high-performance instrument, and it is typically used in laboratories.

Fig. 3.6 Picture of the Tektronix DSA8200 equipped with the TDR80E04 unit [8]



3.3 Frequency Domain Reflectometry (FDR)

In FD, the parameter that corresponds directly to the time-domain reflection coefficient, $\rho(t)$, is the reflection scattering parameter, $S_{11}(f)$. In this case, the frequency-domain response function, $R(f)$, can be written as

$$R(f) = V_0(f) S_{11}(f) \quad (3.10)$$

where $V_0(f)$ is the input signal [26, 38]. Traditionally, measurements performed directly in FD rely on VNAs: in this case, the excitation stimulus is a sinusoidal signal whose frequency is swept over the desired range of analysis.

VNAs usually have more than a single port; therefore, they can also be used for transmission measurements. A generalized block diagram of a VNA is shown in Fig. 3.7, showing the major signal-processing sections. In order to measure the incident, reflected and transmitted signal, four sections are required [3]:

1. *source for stimulus*: most network analyzers have integrated, synthesized sources, providing excellent frequency resolution and stability.
2. *signal-separation block*: this block is generally referred to as the ‘test set’ (which can be either integrated within or separate from the VNA). There are two functions that the signal-separation section must provide. The first is to measure a portion of the incident signal to provide a reference for ratioing (this can be done with splitters or directional couplers). The second function of the signal-splitting hardware is to separate the incident (forward) and reflected (reverse) traveling waves at the input of the SUT (for this task, bridges are often used).
3. *receivers that downconvert and detect the signals*: there are two basic ways of providing signal detection. One relies on diode detectors which convert the RF signal level to a proportional DC level. If the stimulus signal is amplitude modulated, the diode strips the RF carrier from the modulation (this is called AC detection). Diode detection is inherently scalar, as phase information of the RF carrier is lost. The other solution for detecting the signal relies on the tuned receiver, which allows preserving phase information. The tuned receiver uses a local oscillator (LO) to mix the RF down to a lower intermediate frequency (IF).

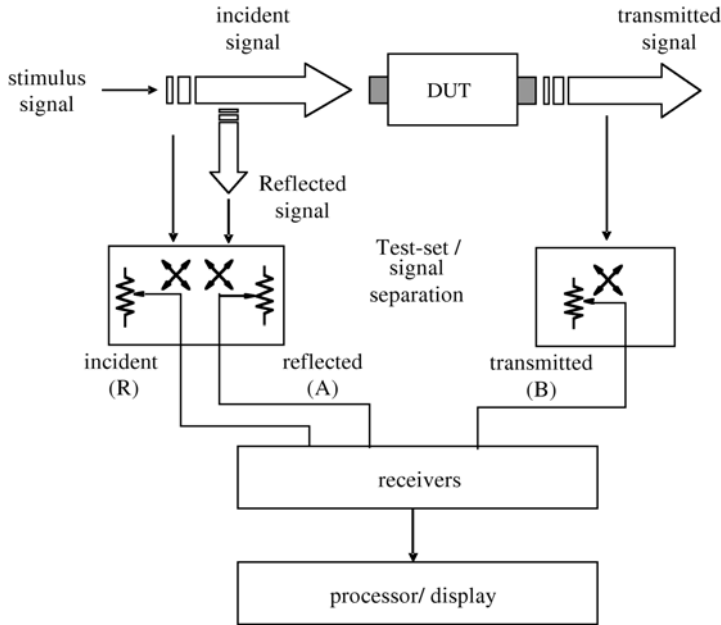


Fig. 3.7 Generalized block diagram of a VNA [1]

The LO is either locked to the RF or the IF signal so that the receivers in the network analyzer are always tuned to the RF signal present at the input. The IF signal is bandpass filtered, which narrows the receiver bandwidth and greatly improves sensitivity and dynamic range. This architecture is called *superheterodyne receiver*, and it is used not only in VNAs, but, as well known, also in spectrum analyzers.

4. *processor/display for calculating and reviewing the results*: this is where the reflection and transmission data are formatted in ways that make it easy to interpret the measurement results.

The picture of a VNA (model Agilent E8361C) is shown in Fig. 3.8.

As will be detailed in the following sections, one of the advantages of FD measurements is that there are well-established error correction models that, through appropriate calibration procedures [such as the short-open-load (SOL) calibration], can be used to reduce the influence of systematic errors [2].

Although VNAs are still costly instruments, in [9], a low-cost single-port VNA for high frequency measurements was developed. The major feature of the VNA proposed in [9] is that it eliminates the need for expensive heterodyne detection schemes required for tuned receiver-based VNA designs; as a result, the realization costs can be reduced dramatically.

Fig. 3.8 Picture of an Agilent E8361C VNA [6].



The FDR approach is often used for the dielectric spectroscopy of materials and for impedance characterization of electronic devices and components. In particular, a VNA used in conjunction with a dielectric probe kit can be employed to characterize the dielectric behavior of materials. However, it is important to point out that, although these are well-established experimental setups, their application is far from being universal, and often specific solutions must be designed.

3.4 TD/FD Combined Approach

The adoption of the TD/FD combined approach allows taking advantage of the benefits of both the approaches. In particular, estimating the frequency-dependent scattering parameter starting from TDR measurements, can help disclosing useful information that is masked in time domain (e.g., single or multiple dielectric relaxation) [21]. This strategy is regarded as a powerful tool for guaranteeing simultaneously low cost and portability of the instruments, and measurement accuracy. The $S_{11}(f)$ of the monitored system can be calculated as the ratio between the discrete Fourier transformation (DFT) of the reflected signal and that of the input signal [22]:

$$S_{11}(f) = \frac{DFT[r(t)]}{DFT[v_0(t)]} \quad (3.11)$$

where $v_0(t)$ is the input function, which should be the unaltered signal generated by the TDR instrument and propagating (along the cable) up to the section where the $S_{11}(f)$ is being measured [29].

This approach provides reliability and adequate measurement accuracy, although relying on relatively-inexpensive TDR instrumentation.

In this regard, it is worth mentioning that, unlike VNAs, portable and affordable TDR instruments (with wide operating frequency range) are commonly available on the market. For example, for the time being, the cost of portable TDR modules with a frequency bandwidth of 10 GHz and of 2 GHz is approximately 7000 USD and 3500 USD, respectively.

3.4.1 Preserving Measurement Accuracy in the TDR/FDR Transformation

There are some crucial aspects that need to be considered to perform an accurate TD/FD transformation, thus reducing errors on the assessment of the spectral response of the system and in the extraction of $S_{11}(f)$ [29].

First, the time duration of the acquisition window, T_w , should be sufficiently long, so as to include all multiple reflections due to the signal traveling back and forth from the probe-end toward the generator. However, an excessively-long T_w would lower the sampling frequency (since the maximum number of acquisition points for a given instrument is fixed), thus limiting the possible frequency range of analysis.

Additionally, to reduce the spectral leakage caused by the rectangular truncation window, two main strategies can be adopted. One is the application of the Nicolson algorithm: a linear ramp is subtracted from the original TDR waveform, and each of the acquired N points is scaled according to the N^{th} final point; in this way, the value of the TDR waveform at the truncation point is zero. The resulting scaled signal, $w^*(nT_c)$, can be written as [33]

$$w^*(nT_c) = w(nT_c) - \frac{w(NT_c)n}{N} \quad (3.12)$$

where T_c is the sampling period, $w(nT_c)$ is the rectangular-windowed signal, and $n = 1, 2, \dots, N$ refers to each sampling point. The important feature of this algorithm is that the FFT of the Nicolson-modified signal produces the same response as the FFT of the original TDR signal [29]. Alternatively to the Nicolson algorithm, it is possible to use the derivatives of the time domain signals calculated with the backward difference method; however, generally, noise is slightly enhanced when the derivative of two similar quantities is taken in digital systems [24, 29].

Moreover, the addition of a number of zeros to the Nicolson-modified waveform (or to the derived signal) artificially enhances the frequency resolution of the obtained FD data, thus corresponding to an ideal interpolation in FD [29].

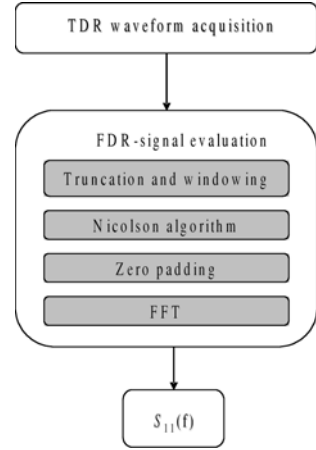
The steps at the basis of the TD/FD approach are summarized in Fig. 3.9: this procedure can be implemented, for example, in a MATLAB-based algorithm that, starting from the TDR waveforms, extrapolates the $S_{11}(f)$.

In practical applications, the specification of the input signal, $v_0(t)$, is crucial for obtaining accurate results. As aforementioned, the input function should be the unaltered signal generated by the TDR instrument and propagating (along the cable) up to the section where the scattering parameter is being measured [29]: in fact, the $S_{11}(f)$ should be evaluated at this very section. $v_0(t)$ may be acquired by removing one of the electrodes from the probe [24]; however, this can be unpractical for most commercial probes, like the probe shown in Fig. 3.4, in which the central conductor is attached to the molded probe-head.

A possible alternative is the use an artificial TDR waveform modeled as an analytical function [23]:

$$v_{0,\text{art}}(t) = \frac{1 + \text{erf}[\alpha_t(t - t_0)]}{2} \quad (3.13)$$

Fig. 3.9 Schematic diagram illustrating the algorithm for the TD/FD combined approach and for extrapolating the reflection scattering parameter from TDR measurements



where erf is the error function, α_t is the inverse of the rise time of the step-like signal, and t_0 is the position where the input signal starts the rise. The parameter α_t is evaluated by fitting the $v_{0,art}(t)$ to the TDR waveform of the probe in air [29].

As will be seen later, the adoption of the SOL calibration on FD-transformed TDR measurements can help circumventing the need of evaluating $v_0(t)$.

3.5 The Sensing Element

The sensing element (or probe) is responsible for the interaction of the stimulus signal with the SUT, and it is the ultimate factor that influences the accuracy of results. Since microwave reflectometry senses the changes in impedance, it is extremely important to employ a probe with a well-known impedance profile; in this way, it is easier to discriminate and interpret the impedance variations due to the SUT.

The high versatility of microwave reflectometry is also related to the possibility of customizing the probe configuration, thus employing an ad hoc solution for the specific needs.

Coaxial probes, which are widely used for monitoring and diagnostics on liquids, are the most simple to design. A coaxial probe is composed of an outer cylinder (acting as the outer conductor) and a rod along the center line of the cylinder (acting as a central conductor). The impedance profile (in the TEM propagation mode) can be easily determined from the transmission line theory, as reported in Sect. 2.1 [21, 25]:

$$Z(f) = \frac{60}{\sqrt{\epsilon_r(f)}} \ln(b/a) \quad (3.14)$$

where $Z(f)$ is the frequency-dependent impedance of the probe filled with the considered material; $\epsilon_r(f)$ is the relative dielectric permittivity of the material filling the

probe (which is assumed lossless²); b is the inner diameter of the outer conductor; and a is the outer diameter of the inner conductor.

On the other hand, for soil monitoring and for granular materials monitoring in general, the multi-rod configuration is a widely used solution. In fact, this configuration allows an easier insertion of the probe into the granular material. For a two-wire transmission line, the characteristic impedance can be derived from (2.13) and it may be written as

$$Z(f) = \frac{120}{\sqrt{\epsilon_r(f)}} \ln \frac{2D}{d}$$

where D is the distance between the center of the conductors, and d is the diameter of each conductor.

However, three-rod probes have become a widespread solution since their electric behavior resembles coaxial cells [42]. Unfortunately, for configurations different from a coaxial line, models are not always available [25], and the evaluation of the probe impedance is not straightforward, especially for unbalanced probes. However, for multi-rod probes, an analytical formulation relating the impedance of the probe in air, Z_p , to the geometric characteristics can be found in [12]:

$$Z_p = \frac{1}{2\pi(n-1)} \sqrt{\frac{\mu_0}{\epsilon_0}} \ln \left[H + \sqrt{H^2 - 1} \right] \quad (3.15)$$

where H is given by

$$H = \frac{(s^2 - a_0^2)^{n-1} - a_i^{2(n-1)}}{a_i^{n-1} \{ (s + a_0)^{n-1} - (s - a_0)^{n-1} \}} \quad (3.16)$$

In the previous equations, n is the number of rods of the probe, a_i is the radius of the probe center conductor, a_0 is the radius of the outer conductors, s is the distance between the middle of the center conductor and the middle of the outer conductor, $\epsilon_0 = 8.854 \times 10^{-12} \text{ Fm}^{-1}$ is the dielectric permittivity of free space, and $\mu_0 = 4\pi \times 10^{-7} \text{ Hm}^{-1}$ is the magnetic permeability of free space. The cross-section of a four-wire probe is shown in Fig. 3.10.

A simplification of (3.16) for three-rod probes is reported in [27]:

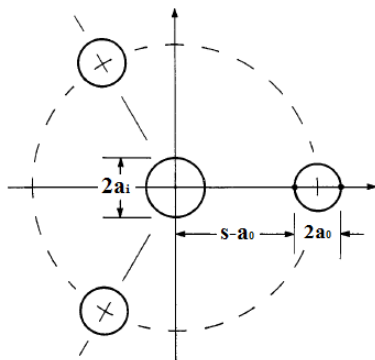
$$Z_{p,\text{three-rod}} = \frac{1}{4\pi} \sqrt{\frac{\mu_0}{\epsilon_0}} \ln \left(\frac{1 - (g/s)^4}{2(g/s)^3} \right) \quad (3.17)$$

where s is the center-to-center rod spacing, and g is the rod radius.

Recently, the adoption of a single-rod probe for monitoring soil moisture was investigated. This probe exploits transverse magnetic (TM) propagation, rather than transverse electromagnetic (TEM) propagation. This kind of probe is simple to

² It is worth pointing out that when dielectric losses of the material cannot be neglected, equation (3.14) can be extended by considering the complex dielectric permittivity.

Fig. 3.10 Cross section of a four-wire TDR probe [12]



realize and easy to insert; nevertheless, the analysis of the TDR waveform is somewhat more complicated and the region of influence is relatively high [34].

Fig. 3.11 shows the geometry and corresponding electrical fields of some typical probe configurations. A three-rod probe and a two-rod probe are shown in Fig. 3.12 [13].

It must be pointed out that, when a noninvasive approach must be preserved, it is possible to use surface probes, like the one shown in Fig. 3.13 [40]. Alternatively, it is also possible to use antennas as sensing elements: this possibility will be discussed in Sect. 5.6 [18].

It is worth mentioning that the probe configuration introduces some limitations on the useful frequency range of analysis, mostly because of the geometric characteristics. In particular, the TEM mode propagation assumption is true when the operating wavelength is higher than the dimensions of the probe [26]. For example, for a coaxial probe, the circumferential resonance frequency $f_{\text{up,circ}}$ (below which the TEM mode propagation assumption is valid) is given by

$$f_{\text{up,circ}} = \frac{2c}{(a+b)\pi\sqrt{\epsilon_r}} \quad (3.18)$$

where c is the speed of light and ϵ_r is the dielectric permittivity of the material filling the probe³. Similarly, the longitudinal resonant frequency is given by [26]

$$f_{\text{up,long}} = \frac{c}{2L\sqrt{\epsilon_r}} \quad (3.19)$$

where L is the length of the probe.

As a matter of fact, several probe configurations are commonly available on the market; nevertheless, their configurations often do not allow an easy calibration procedure to be performed. As will be detailed later in the book, the calibration procedure consists in measuring the reflected signal when some standard (known)

³ Equation (3.18) is equivalent to 2.10.

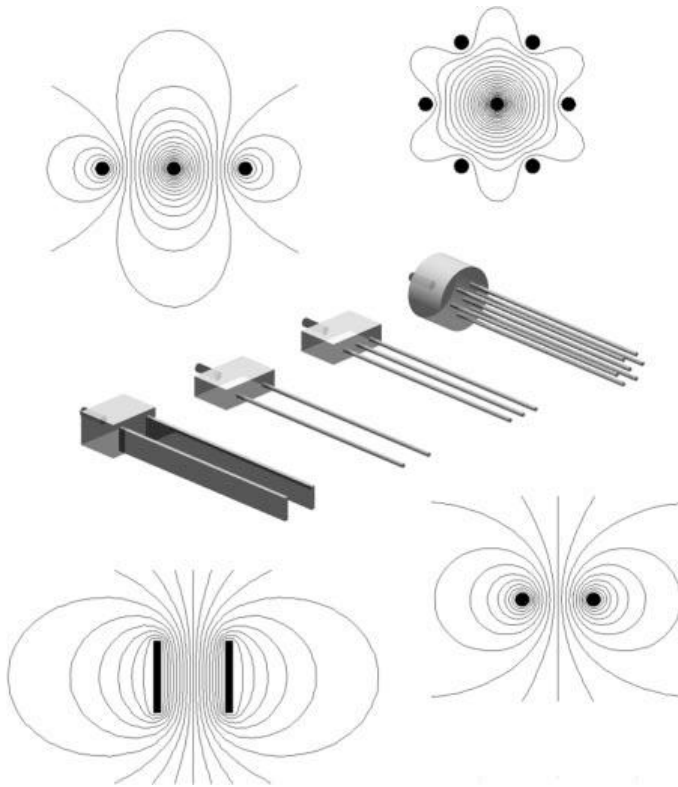
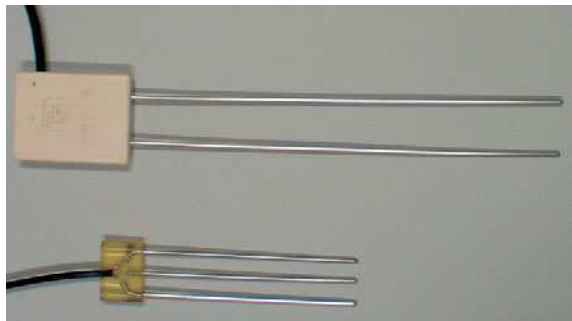


Fig. 3.11 Various probe designs (parallel plate and multi-wire configurations), typically used for TDR-based soil moisture. Electrical field lines generated for different probe configurations are also shown: closer line spacing is associated with a more concentrated field (i.e., greater influence on permittivity) [30]

Fig. 3.12 Three-rod TDR probe (0.15 m-long; 3.20 mm-diam. rods; 12.0 mm rod spacing), and two-rod probe (Campbell Scientific CS616) [13]



impedances are connected at the section where the sensing portion of the probe begins. Fig. 3.14 clarifies this aspect; however, the importance of calibration will be discussed in detail in the following chapters.

Fig. 3.13 Serpentine-shaped probe [40]

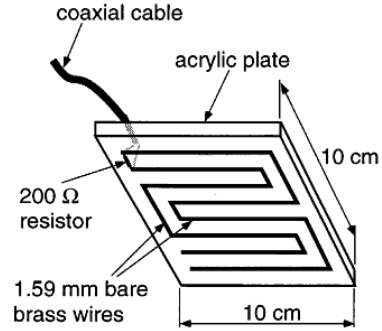
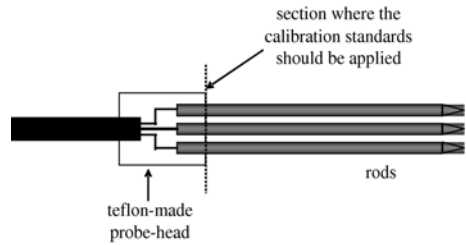


Fig. 3.14 Schematic of the longitudinal section of a three-rod probe. The section where the reference standard impedances should be connected is indicated



Indeed, the calibration procedure plays a major role in terms of minimization of systematic errors, thus leading to a significant enhancement of the final measurement accuracy. A viable alternative is to specifically design and realize the probe that would suit the specific needs [39] and to realize the corresponding calibration structure (as described for the application discussed in Sect. 4.3).

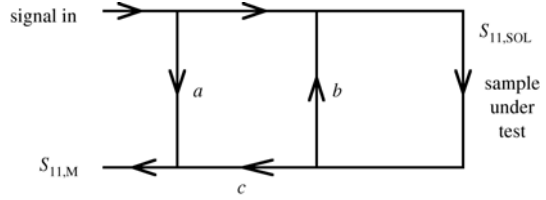
3.6 Strategies for Enhancing Accuracy in BMR Measurements

As well known, measurements are typically affected by both systematic and random errors. The effects of systematic errors can be compensated for through appropriate calibration procedures [28]. On the other hand, the residual random measurement fluctuations (essentially due the environmental and operating conditions, noise, etc.) are taken into account through a statistical analysis performed on a series of repeated measurements.

3.6.1 Calibration Procedure in Time Domain

In TD measurements, since the information on the SUT is retrieved from direct measurement of the apparent length of the probe immersed in the SUT, it is necessary to

Fig. 3.15 Signal flow graph describing the error model for the SOL calibration procedure [15]



locate exactly where the beginning and the end of the probe are. This is not a trivial task especially when unmatched probes are used. For example, for the widely-used three-rod probe schematized in Fig. 3.4, the actual beginning of the sensing element is section $k = 1$ and this point has to be individuated in the corresponding TDR waveform. In fact, when the probe is inserted in a material with specific dielectric characteristics, only L_{app} will change. The offset length (L_0) has to be individuated: L_0 corresponds to the electric distance between the cable end and the section $k = 1$. The individuation of the point that, in the TDR waveform, corresponds to section $k = 1$ may be complicated because of the masking effect caused by the transition coaxial cable/rods and the portion of the rods included in the rigid support (i.e., probe-head).

On such bases, to discriminate the electric distance of the rods inserted in the SUT, L_{app} , from the electric distance of the probe-head, L_0 , a simple but effective procedure has to be performed. To evaluate L_0 , it is necessary to perform preliminary TDR measurements on materials with well-known dielectric characteristics, such as air and de-ionized water [16]. Considering Fig. 3.4, this can be simply summarized in the following equations:

$$L_{p,water} = L_0 + \sqrt{\epsilon_{app,water}} L \quad (3.20)$$

$$L_{p,air} = L_0 + \sqrt{\epsilon_{air}} L \quad (3.21)$$

where L is the physical length of the sensitive portion of the probe in air; $\epsilon_{app,water} \cong 80$ is the apparent permittivity of water; and $\epsilon_{air} \cong 1$ is the dielectric constant of air. Once L_0 is individuated, it can be compensated for in successive measurements.

3.6.2 Calibration Procedure in Frequency Domain

Frequency domain reflectometry can rely on well-established calibration procedures. For single-port measurements, such as microwave reflectometry measurements, the short-open-load (SOL) calibration is largely used [14]. The error model can be identified using a signal flow graph as shown in Fig. 3.15: $S_{11,SOL}$ is the response of the sample under test; $S_{11,M}$ is the measured response (which includes the parasitic effects); and a , b and c are the parameters calculated from the open, short

and 50 Ω -load calibration measurements. The SOL-calibrated frequency response of the sample under test can be extracted from the signal flow graph according to

$$S_{11,\text{SOL}} = \frac{S_{11,\text{M}} - a}{bS_{11,\text{M}} - ab + c} \quad (3.22)$$

where a , b , and c include the contribution of $S_{11,\text{MO}}$, $S_{11,\text{MS}}$, and $S_{11,\text{ML}}$, which are the reflection scattering parameters when an open, a short and a matched loads are connected:

$$a = S_{11,\text{ML}}, \quad (3.23)$$

$$b = \frac{S_{11,\text{MO}} + S_{11,\text{MS}} - 2S_{11,\text{ML}}}{S_{11,\text{MO}} - S_{11,\text{MS}}}, \quad (3.24)$$

$$c = \frac{2(S_{11,\text{ML}} - S_{11,\text{MO}})(S_{11,\text{MS}} - 2S_{11,\text{ML}})}{S_{11,\text{MO}} - S_{11,\text{MS}}}. \quad (3.25)$$

The aforementioned error-compensation model is solved directly in FD; nevertheless, it can be implemented in the TD/FD transformation algorithm described in [15], thus extracting the calibrated $S_{11}(f)$ from TDR measurements [17]. The aforementioned calibration procedures were implemented in the transformation algorithm used for transforming TD data into FD data. An additional advantage of this strategy is that it overcomes the need of acquiring the input function, v_0 .

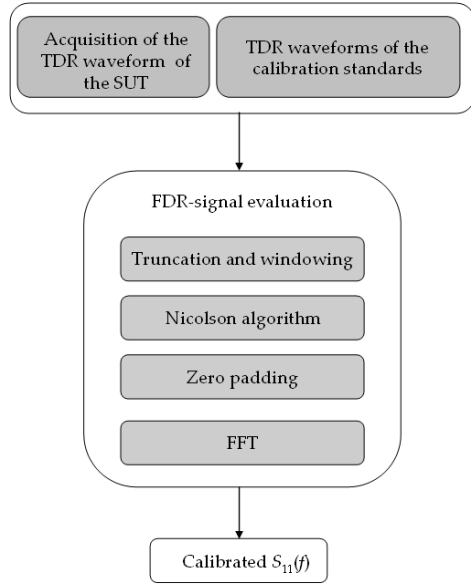
However, calibration standards are often not readily available for many commercial probes. In these cases, it is necessary to fabricate appropriate calibration fixtures or custom-made calibration standards.

An innovative calibration procedure, namely triple short calibration (TSC), has been presented in [35]: this procedure, which will be described in detail in Chap. 5, relies on three short-circuit applied at three different sections along the probe. The major advantage is that realizing a short-circuit condition is easier than achieving an open-circuit condition or a matched condition, especially for probes as the one represented in Fig. 3.4.

3.6.3 Time-gated Frequency Domain Approach

Time gating is a calibration strategy that can be adopted for excluding systematic errors in the TD/FD combined approach [5]. Time gating implies the individuation and the removal of those portions of the waveform that are considered undesired effects (e.g., reflections caused by connection transitions): once these effects are removed from the TD data (via software), the data are transformed into the FD. As a result of the process, the gated frequency response will resemble more closely the response of the sole SUT. As a matter of fact, the time-gating option is often directly integrated within VNAs: in this case, the FD response is transformed in TD; then gating is applied, and, finally, the data are transformed back into the FD.

Fig. 3.16 Schematic diagram illustrating the implemented algorithm for the TD/FD combined approach and for extrapolating the calibrated reflection scattering parameter from TDR measurements



As an example, Fig. 3.17 shows the sequence of the gating operation for isolating the frequency-domain response of the outer connector of a cable. Considering the non-gated time domain response of the cable, the discontinuity on the left is due to the input connector and the discontinuity on the right is due to the output connector. By using the gating function, the effect of the mismatch can be removed in order to see the frequency response of just the output connector; in this way, the frequency response of the sole output connector is obtained.

It must be pointed out, however, that gating is an extremely delicate strategy, and it should be adopted with particular care.

Time-gated frequency-domain reflectometry can be particularly useful for removing undesired reflections from the environment while measuring the $S_{11}(f)$ of antennas when the anechoic chamber is not available [19]; this aspect will be further discussed in the following chapters.

3.6.4 Transmission Line Modeling and Inverse Modeling

An additional strategy for compensating for systematic errors is to model the influence of the parasitics through a transmission line (TL) model. More specifically, the SUT is schematized as a circuit model, and the parasitics are modeled as lumped circuit elements. This approach can virtually compensate for all the systematic errors effects.

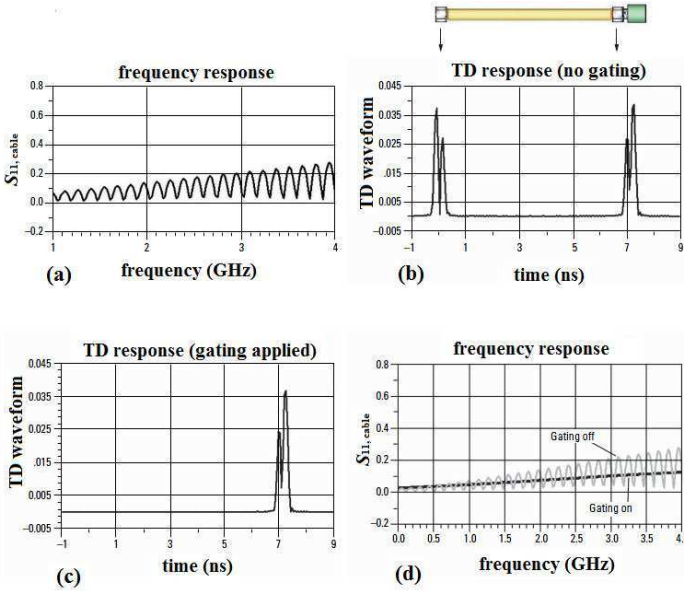


Fig. 3.17 Sequence of the gating operation. **a** frequency response of a cable. **b** time domain response. **c** gating applied to remove the first discontinuity. **d** frequency response with gating on and off [5]

This approach is based on the fact that the $S_{11}(f)$ at a specific section is to be seen as the resultant of infinite contributions, that can be mathematically represented through the multiple reflection theory [20]. The measurement cell can be considered as a multi-section transmission line, and M is the number of sections where impedance changes occur. Let $k = 0, \dots, M$ be the number of sections starting from the end of the probe ($k = 0$) up to the TDR output ($k = M$). For the sake of example, Fig. 3.18 shows the ‘main’ sections of a three rod probe.

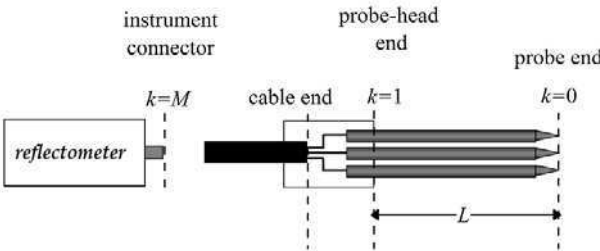


Fig. 3.18 Schematization of the ‘main’ sections of a typical three-rod probe

The scattering parameter at the generic section k , due to the sections up to the k^{th} is given by the following equation [20, 23, 38]:

$$S_{11}^k(f) = \frac{\Gamma_s^k(f) + S_{11}^{k-1}(f) e^{-2\gamma L_k}}{1 + \Gamma_s^k(f) S_{11}^{k-1}(f) e^{-2\gamma L_k}} \quad (3.26)$$

where $S_{11}^{k-1}(f)$ is the scattering parameter at the $(k-1)^{th}$ section due to the first $(k-2)$ sections; $\Gamma_s^k(f)$ is the reflection coefficient; γ is the complex frequency-dependent propagation parameter [23]; and L_k is the length of the k^{th} section. The losses due to relaxation and conductivity for a TEM mode propagation, $\gamma(f)L$ are given by [25]

$$\gamma(f)L = i2\pi fL \frac{\sqrt{\epsilon_r^*(f)}}{c} \quad (3.27)$$

However, an assumption must be made about the reflection at the end of the probe (i.e., section $k=0$): for an open-ended probe, $S_{11}^0(f) = 1$; for a short-circuited probe $S_{11}^0(f) = -1$; and for a matched probe $S_{11}^0(f) = 0$.

The reflection coefficient between the different sections k of the transmission line is

$$\Gamma_s^k(f) = \frac{Z_{k-1}(f) - Z_k(f)}{Z_{k-1}(f) + Z_k(f)} \quad (3.28)$$

where $Z_k(f)$ is the impedance of the transmission line at section k and is given by

$$Z_k(f) = \frac{Z_{0,k}}{\sqrt{\epsilon^*(f)}} \quad (3.29)$$

$Z_{0,k}$ being the characteristic impedance of the transmission line at section k .

Equation (3.26) is recursive; therefore, to evaluate $S_{11}(f)$ for the whole system (i.e., at the M^{th} section), it is necessary to subsequently compute $S_{11}^k(f)$ for $k=1$, for $k=2, \dots, k=M$ [38].

The practical usefulness of the TL modeling will be discussed thoroughly in the following chapters. However, it is useful to anticipate one major application, which is the extraction of the Cole-Cole parameters of materials. The approach proposed for the accurate evaluation of the Cole-Cole parameters is the combination of multiple strategies, and it comprises three major steps:

- First, the calibrated $S_{11}(f)$ is evaluated (either through direct VNA measurements or through the TD/FD combined approach);
- Secondly, the used measurement cell is accurately modeled as a TL, and the considered material is parameterized through the Cole-Cole model;
- Finally, through the minimization of the deviations between the measured $S_{11}(f)$ and the reflection scattering parameter of the implemented TL model, the Cole-Cole parameters of the material are obtained.

These steps are summarized in the diagram in Fig. 3.19 and will be described in detail in the following subsections.

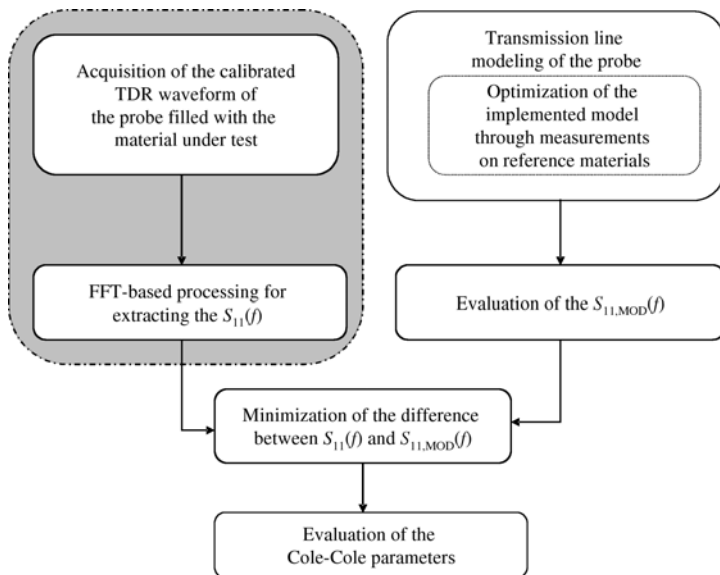


Fig. 3.19 Schematization of the TL-based procedure for extracting the Cole-Cole parameters. The activities enclosed in the gray-colored area can be substituted by direct VNA measurements of the $S_{11}(f)$

References

- [1] Exploring the architectures of network analyzers. Agilent Application Note 1287-2, USA (2000)
- [2] Applying error correction to network analyzer measurements. Agilent Application Note 1287-3, USA (2002)
- [3] Network analyzer basics. USA (2004)
- [4] Time domain reflectometry theory. Agilent Application Note 1304-2, Palo Alto, CA (2006)
- [5] Time domain analysis using a network analyzer. Agilent Application Note 1287-12, USA (2007)
- [6] Agilent millimeter-wave network analyzers 10 MHz to 110 GHz, with extensions to 1.05 THz. USA, technical overview (2010)
- [7] TDR100 instruction manual - revision 2/10. Logan, UT (2010), <http://www.campbellsci.com/documents/manuals/tdr100.pdf> (cited December 27, 2010)
- [8] <http://www2.tek.com> (2011)
- [9] Abou-Khousa, M.A., Baumgartner, M.A., Kharkovsky, S., Zoughi, R.: Novel and simple high-frequency single-port vector network analyzer. *IEEE Trans. Instrum. Meas.* 59(3), 534–542 (2010)
- [10] Andrews, J.R.: Time domain reflectometry (TDR) and time domain transmission (TDT) measurement fundamentals. Application Note AN-15, Boulder, CO (2004)

- [11] Artacho, J.M., Fornies-Marquina, J.M., Letosa, J., Garcia, M., Bottreau, A.M.: Direct deconvolution signal in time domain reflectometry. *IEEE Trans. Magn.* 31(3), 1610–1613 (1995)
- [12] Ball, J.A.R.: Characteristic impedance of unbalanced TDR probes. *IEEE Trans. Instrum. Meas.* 51(3), 532–536 (2002)
- [13] Blonquist, J.M., Jones, S.B., Robinson, D.A.: Standardizing characterization of electromagnetic water content sensors: part 2. evaluation of seven sensing systems. *Vadose Zone J.* 4, 1059–1069 (2005)
- [14] Callegaro, L.: The metrology of electrical impedance at high frequency: a review. *Meas. Sci. Technol.* 20(2), 1–14 (2009)
- [15] Cataldo, A., Catarinucci, L., Tarricone, L., Attivissimo, F., Trotta, A.: A frequency-domain method for extending TDR performance in quality determination of fluids. *Meas. Sci. Technol.* 18(3), 675–688 (2007)
- [16] Cataldo, A., Cannazza, G., De Benedetto, E., Tarricone, L., Cipressa, M.: Metrological assessment of TDR performance for moisture evaluation in granular materials. *Measurement* 42(2), 254–263 (2009)
- [17] Cataldo, A., Catarinucci, L., Tarricone, L., Attivissimo, F., Piuze, E.: A combined TD-FD method for enhanced reflectometry measurements in liquid quality monitoring. *IEEE Trans. Instrum. Meas.* 58(10), 3534–3543 (2009)
- [18] Cataldo, A., Monti, G., De Benedetto, E., Cannazza, G., Tarricone, L.: A noninvasive resonance-based method for moisture content evaluation through microstrip antennas. *IEEE Trans. Instrum. Meas.* 58(5), 1420–1426 (2009)
- [19] Cataldo, A., Monti, G., De Benedetto, E., Cannazza, G., Tarricone, L., Catarinucci, L.: Assessment of a TD-based method for characterization of antennas. *IEEE Trans. Instrum. Meas.* 58(5), 1412–1419 (2009)
- [20] Feng, W., Lin, C.P., Deschamps, R.J., Drnevich, V.P.: Theoretical model of a multisection time domain reflectometry measurement system. *Water Resour. Res.* 35(8), 2321–2331 (1999)
- [21] Friel, R., Or, D.: Frequency analysis of time-domain reflectometry (TDR) with application to dielectric spectroscopy of soil constituents. *Geophysics* 64(3), 707–718 (1999)
- [22] Heimovaara, T.J.: Frequency domain analysis of time domain reflectometry waveforms: 1. measurement of the complex dielectric permittivity of soils. *Water Resour. Res.* 30(2), 189–199 (1994)
- [23] Heimovaara, T.J.: Frequency domain modeling of TDR waveforms in order to obtain frequency dependent dielectric properties of soil samples: a theoretical approach. In: *Proceedings of the 2nd International Symposium and Workshop on Time Domain Reflectometry for Innovative Geotechnical Applications* (2001)
- [24] Heimovaara, T.J., Bouten, W., Verstraten, J.M.: Frequency domain analysis of time domain reflectometry waveforms: 2. a four-component complex dielectric mixing model for soils. *Water Resour. Res.* 30, 201–209 (1994)
- [25] Heimovaara, T.J., Huisman, J.A., Vrugt, J.A., Bouten, W.: Obtaining the spatial distribution of water content along a TDR probe using the SCEM-UA bayesian inverse modeling scheme. *Vadose Zone J.* 3, 1128–1145 (2004)
- [26] Huisman, J.A., Bouten, W., Vrugt, J.A., Ferrè, P.A.: Accuracy of frequency domain analysis scenarios for the determination of complex permittivity. *Water Resour. Res.* 40 (2004)
- [27] Huisman, J.A., Lin, C.P., Weihermuller, L., Vereecken, H.: Accuracy of bulk electrical conductivity measurements with time domain reflectometry. *Vadose Zone J.* 7(2), 426–433 (2008)

- [28] ISO, Guide to expression of uncertainty in measurement (1995)
- [29] Jones, S.B., Or, D.: Frequency domain analysis for extending time domain reflectometry water content measurement in highly saline soils. *Soil Sci. Soc. Am. J.* 68, 1568–1577 (2004)
- [30] Jones, S.B., Wraith, J.M., Or, D.: Time domain reflectometry measurement principles and applications. *Hydrol. Process.* 16(1), 141–153 (2002)
- [31] Kelleners, T.J., Robinson, D.A., Shouse, P.J., Ayars, J.E., Skaggs, T.H.: Frequency dependence of the complex permittivity and its impact on dielectric sensor calibration in soils. *Soil Sci. Soc. Am. J.* 69, 67–76 (2005)
- [32] Mohamed, A.M.O.: Principles and applications of time domain electrometry in geoenvironmental engineering. Taylor & Francis Group, UK (2006)
- [33] Nicolson, A.M.: Forming the fast Fourier transform of a step response in time-domain metrology. *Electron Lett.* 9(14), 317–318 (1973)
- [34] Oswald, B., Benedickter, H.R., Bachtold, W., Fluhler, H.: A single-rod probe for time domain reflectometry measurements of the water content. *Vadose Zone J.* 3, 1152–1159 (2004)
- [35] Piuze, E., Cataldo, A., Cannazza, G., De Benedetto, E.: An improved reflectometric method for soil moisture measurement exploiting an innovative triple-short calibration. *IEEE Trans. Instrum. Meas.* 59(10), 2747–2754 (2010)
- [36] Rapuano, S., Harris, F.J.: An introduction to FFT and time domain windows. *IEEE Instrum. Meas. Mag.* 10(6), 32–44 (2007)
- [37] Robinson, D.A., Jones, S.B., Wraith, J.M., Or, D., Friedman, S.P.: A review of advances in dielectric and electrical conductivity measurement in soils using time domain reflectometry. *Vadose Zone J.* 2(4), 444–475 (2003)
- [38] Robinson, D.A., Schaap, M.G., Or, D., Jones, S.B.: On the effective measurement frequency of time domain reflectometry in dispersive and nonconductive dielectric materials. *Water Resour. Res.* 41(2), W02,007.1–W02,007.9 (2005)
- [39] Sakaki, T., Rajaram, H.: Performance of different types of time domain reflectometry probes for water content measurement in partially saturated rocks. *Water Resour. Res.* 42(7) (2006)
- [40] Selker, J.S., Graff, L., Steenhuis, T.: Noninvasive time domain reflectometry moisture measurement probe. *Soil Sci. Soc. Am. J.* 57(4), 934–936 (1993)
- [41] Timlin, D.J., Pachepsky, Y.A.: Comparison of three methods to obtain the apparent dielectric constant from time domain reflectometry wave traces. *Soil Sci. Soc. Am. J.* 60(4), 970–977 (1996)
- [42] Zegelin, S.J., White, I., Jenkins, D.R.: Improved field probes for soil water content and electrical conductivity measurement using time domain reflectometry. *Water Resour. Res.* 25(11), 2367–2376 (1989)

Chapter 4

Quantitative and Qualitative Characterization of Liquid Materials

*'Science exists, moreover, only as a journey toward truth.
Stifle dissent and you end that journey.'*
John Charles Polanyi

Abstract. In this chapter, broadband microwave reflectometry (BMR)-based methods for measuring simultaneously the levels and the dielectric characteristics of liquid materials are presented.

First, an approach based solely on time domain reflectometry (TDR) measurements and on the analysis of TDR waveforms is described.

Secondly, a further enhancement of this method is accomplished by resorting to the combination of TDR with frequency domain reflectometry (FDR). Also this method provides, in one shot, the level and the dielectric permittivity of the considered liquids (this time, the complete spectral signature is obtained in terms of Cole-Cole parameters). This approach is considered the optimal solution especially when dealing with dispersive media. In this second measurement method, the accuracy is enhanced also through the adoption of a transmission line (TL) modeling of the measurement cell and through the realization of a custom-made fixture that allows performing short-open-load (SOL) calibration measurements.

Finally, BMR-based measurements of the dielectric characteristics are extended to edible liquids: in particular, vegetable oils are considered.

Reported results show that all the proposed methods have strong potential for possible practical implementation in the field of industrial monitoring.

It will be evident how, in all the considered approaches, the design of the probe is crucial for enhancing the final measurement accuracy.

4.1 Introduction

In recent years, dielectric spectroscopy measurements performed through broadband microwave reflectometry (BMR) have become an effective tool for extracting information on the qualitative and quantitative status of materials, thus opening interesting perspectives for several monitoring applications.

With regards to the fluid processing-related industry, measurement and control of liquid parameters play an important role in industrial applications, for example, in the petrochemical industrial processing. In this field, additional stringent requirements frequently deal with the spatial localization of non-miscible-layered liquids and with the depth estimation of different layers of liquid. As an example, during the refinery industrial processing, a portion of water is often present in the bottom of the tanks, as a non-miscible fraction, and its continuous monitoring is crucial. For this purpose, typically, various flow meters are used for fiscal and quality purposes; nevertheless, the a-priori knowledge of the permittivity of the involved fluid components, and the associated sample calibration are mandatory for the practical implementation of such methods.

Starting from these considerations, in this chapter, first, a time domain-based approach for the simultaneous estimation of the dielectric characteristics of liquid materials and of their level is presented. It is shown that the analysis of time domain reflectometry (TDR) data allows, in one shot, the measurement of liquid levels, the determination of multiple interfaces in layered media, as well as the evaluation of dielectric properties. Experimental results demonstrate the robustness and reliability of the proposed method. As reported in [21], which compares the performance of different liquid level sensors, TDR fares well with respect to other sensing technologies.

Secondly, an enhancement of the simultaneous measurements of liquid levels and dielectric permittivity is achieved through the implementation of the TD/FD combined approach described in subsection 3.6.4. The proposed combined approach allows the evaluation of the Cole-Cole parameters of the considered samples. Indeed, accuracy enhancements are obtained also through some novel strategies that include i) an appropriate probe design; ii) the realization and the adoption of a custom-made fixture for allowing calibration measurements to be performed; and, most importantly, iii) a targeted optimization routine that renders the method extremely robust. Results deriving from simple TDR technique are compared with those achieved, in frequency domain, both through the fast Fourier transform (FFT)-based processing of TDR data and through direct measurements with vector network analyzer (VNA). The comparison between the reference and the frequency-domain extrapolated values of permittivity and levels shows a very good agreement.

Finally, in this chapter, the estimation of the Cole-Cole parameters through BMR is applied to edible liquids: in particular, an interesting test-case for vegetable oils is presented. Also in this case, starting from TDR measurements, the proposed approach allows the accurate estimation of the Cole-Cole parameters of the considered oils, thus providing a method useful for qualitative and anti-adulteration control purposes (which are regarded as crucial issues in the specific sector).

The common important feature of the proposed approaches is the possibility of automating the necessary data-processing, thus providing results in real time. On such bases, the proposed procedures can be considered as excellent candidates for qualitative and quantitative liquid monitoring applications, with relevant

perspectives in the field of industrial monitoring, which not only does require accuracy and reliability, but also low cost and portability of the involved devices.

4.2 Estimation of Levels and Permittivities of Industrial Liquids Directly from TDR

In this section, a TDR-based method for simultaneous quantitative and qualitative monitoring of liquids is described. As outlined in the previous chapters, the level of liquids in tanks can be inferred from the travel time of the electromagnetic signal along the probe. The basic idea concerns the use of a perfectly-matched coaxial probe immersed in a lossless non-dispersive liquid. Under these circumstances, the unknown dielectric characteristics can be evaluated from (3.14), as

$$\epsilon_r \cong \epsilon_{\text{app}} \cong \left(\frac{1 - \rho}{1 + \rho} \right)^2 \quad (4.1)$$

where ρ is the reflection coefficient in time domain.

The quantitative measurement of liquid level is based on the spatial localization of different interfaces. This task can be performed simply by considering the reflection coefficient (or, even better, its derivative) versus the apparent distance. In fact, the clear peaks occurring at significant discontinuities are associated with a local maximum (or minimum) of the reflection coefficient derivative curve; hence, they spatially localize the points associated with different interfaces. For example, in the TDR waveform of the system schematized in Fig. 4.1, a strong drop of the reflection coefficient would be clearly detectable at the air-liquid interface (due to the different dielectric constant of air and of the liquid).

Once the dielectric characteristics of the liquid are known, the level of the liquid (or height, H) can be evaluated directly from (3.5), which is rewritten here for convenience:

$$H = \frac{H_{\text{app}}}{\sqrt{\epsilon_{\text{app}}}} \quad (4.2)$$

where H is the physical length of the probe portion immersed in the liquid under test (LUT), and H_{app} is the corresponding apparent distance.

To summarize, the adopted measurement method comprises the following steps:

1. first, the apparent liquid level (H_{app}) is evaluated from the derivative of the measured TDR waveform;
2. secondly, using (4.1), the measured reflection coefficient value is used to calculate the apparent dielectric constant value of the considered medium; finally,
3. equation (4.2) allows retrieving the liquid level, H .

In spite of the simplicity of the listed steps, there are some important aspects that must be considered to obtain accurate results: these aspects are thoroughly discussed in subsection 4.2.2.

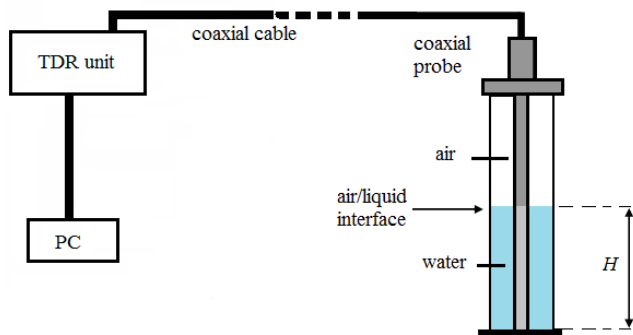


Fig. 4.1 Setup for TDR-based liquid level measurements: the probe is immersed in the liquid, and it is connected to the TDR instrument (which, in turn, is controlled through a computer)

4.2.1 Probe Design and Realization

As aforementioned, coaxial probes are the wisest choice for applications on liquids. This probe configuration can guarantee the insertion into the liquid samples, the mechanical stability, the electromagnetic continuity with the connection to the coaxial cable, as well as an adequate impedance matching. This strongly enhances the overall performance of the measurement method. The first aspect to take into account is the minimization of the impedance mismatches along the line (i.e., TDR unit, coaxial cable and probe in air), so that (4.1) can be considered reasonably valid.

The schematic configuration of the used probe is shown in Fig. 4.2. The designed coaxial probe is made up of a central cylindrical conductor and of a coaxial stainless steel conductive shield. The values of the outer diameter of the inner conductor (a) is 10 mm, whereas the inner diameter of the hollow outer conductor (b) is 23 mm: these dimensions allow a good 50Ω -matching, according to (3.14). The outer conductor is perforated, so as to allow fluid circulation when the coaxial probe is immersed in the liquid (four series of holes with a diameter of 8 mm and 3 cm-spaced, are made longitudinally along the external hollow conductor). The 1 cm-thick metallic flange facilitates the positioning of the probe in the tank/sample holder (hence, it can be customized in order to fit the required operating conditions). The longitudinal cross-section scheme, reported in Fig. 4.2, clearly shows the other design details. The probe-head and the outer conductor are 6 cm and 43.5 cm long, respectively. The inner conductor is centered on the coaxial probe-head, through a 2 cm-teflon ring, while the lower part of the coaxial probe (probe-end point) is open-ended.

The adopted 50Ω -matched coaxial probe shows very good performance in terms of impedance mismatching minimization. This can be seen from Fig. 4.3, which shows that the measured reflection coefficient associated to the probe in air is approximately zero.

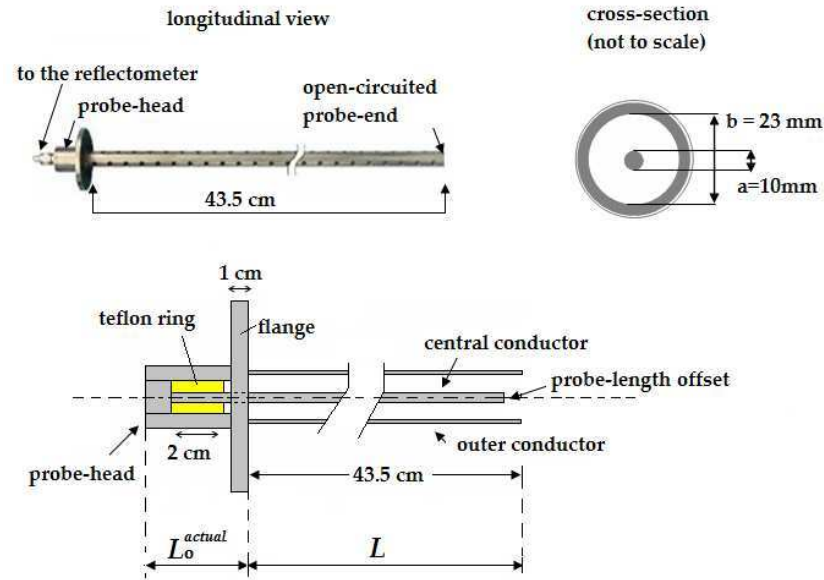


Fig. 4.2 Coaxial probe picture, dimensional scheme of cross-section, and longitudinal geometric scheme

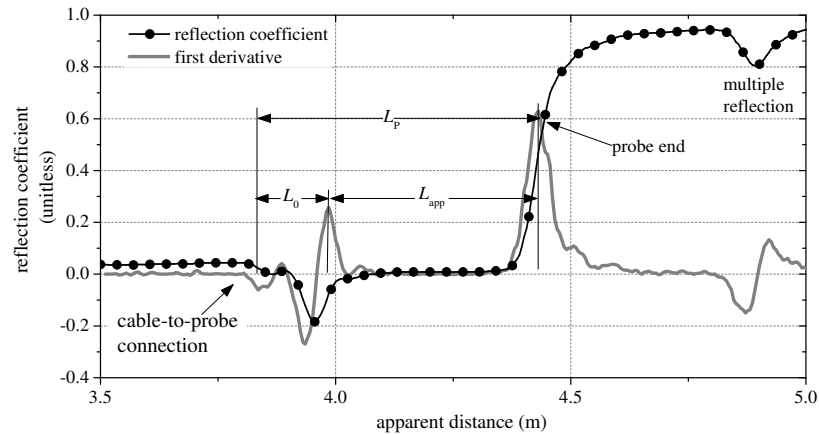


Fig. 4.3 TDR waveform and derivative of data for the coaxial probe in air

4.2.2 Sources of Errors and Compensation Strategies in TD

The overall contribution to the uncertainty in TDR measurements can be associated to some error sources that are related to the specific measurement setup (and, consequently, to the electromagnetic characteristics of the signal propagating along the transmission line). Once the error components are characterized, the related effects can be de-embedded from measurements.

The overall uncertainty affecting TDR measurements can be mostly attributed to the following causes:

1. the undesired impedance variations introduced by the non-ideal cable-to-probe connection, by the teflon ring inserted in the probe-head, etc.;
2. the non-ideal $50\ \Omega$ -matching of the coaxial cable and of the probe;
3. the effects of losses and signal dissipation in the coaxial cables (which increase as the cable length increases);
4. the assumptions of lossless and non-dispersive liquid; and, finally,
5. the periodical presence of parasitic multiple reflections in TDR waveforms, caused by the signal traveling back and forth along the transmission line [1].

Although the errors sources listed above refer to the specific setup, they can be present in most BMR-based measurement systems.

The aspects listed in points 1)–3) can be attributed to the non-ideal characteristics of TDR equipment and the related effects mainly cause systematic errors, both in the estimation of the apparent distances and in the evaluation of the reflection coefficient values. On the other hand, the aspects listed in points 4) and 5), are mainly related to the intrinsic limitation of the method itself, which can be circumvented through the approach described in Sect. 4.3

4.2.2.1 Minimization of Errors in the Evaluation of Apparent Distance

Error sources described in point 1) basically lead to an overestimation of the apparent distances; hence, they can be considered systematic. These effects can be minimized by calibration measurements on ‘reference distances’.

As seen in subsection 3.6.1, it is important to evaluate L_0 (which, as reported in Figs 4.2 and 4.3, refers to the probe-head portion of the probe) through preliminary calibration measurements (in air and in de-ionized water), thus individuating the portion of the waveform L_{app} that refers to the effective sensitive portion of the probe, L .

4.2.2.2 Minimization of Errors in the Evaluation of the Amplitude of the Reflection Coefficient

The parasitic effects described in points 2) and 3) are mainly related to an attenuation and dissipation of the electromagnetic signal, which can be due both to the

cables and to the material under investigation itself. The related error contribution basically affects the dielectric constant estimation described by (4.1). However, a separate calibration procedure can help discriminating the attenuations due to the sample under investigation from that due to the measurement setup. In fact, the coaxial cable loss attenuation constant, A , can be found through the following procedure [4]: measuring the reflection coefficient when the distal end of the probe is open-circuited and short-circuited (i.e., $\rho_{\text{meas}}^{\text{oc}}$ and $\rho_{\text{meas}}^{\text{sc}}$), and comparing the results with the theoretical values (i.e., $\rho_{\text{ideal}}^{\text{oc}} = +1$ and $\rho_{\text{ideal}}^{\text{sc}} = -1$), the reflection coefficient amplitudes can be corrected, according to

$$A = \exp(2\alpha L_{\text{cable}}) \quad (4.3)$$

$$\rho_{\text{corr}} = A\rho_{\text{meas}} \quad (4.4)$$

where $\alpha [\text{m}^{-1}]$ is the attenuation coefficient of the coaxial cable, and $L_{\text{cable}} [\text{m}]$ is the length of the coaxial cable. The constant A accounts for signal losses over a path of length $2L_{\text{cable}}$, and equals 1 for ideal cables. For the specific 3 m-long coaxial cable used in the measurements reported in this section, the evaluated A is 1.06.

4.2.2.3 Intrinsic Limitation of the Proposed Method

Finally, the implications of points 4) and 5) can be considered as intrinsic limitations of the proposed method itself and of the considered measurement setup, respectively.

Generally, the presence of a steady curve portion in the TDR waveform indicates that the liquid can be considered as a lossless dielectric. Conversely, when dissipative liquids are considered (such as electrolyte solutions or water-like liquids), the ohmic and polarization losses cause a strong variation of the reflection coefficient at the probe-portion filled with liquid. This problem can be circumvented through the estimation of the static electrical conductivity, or through the consideration of the FD approach (as detailed in the following section).

As for the parasitic effects of multiple reflections described in point 5), they can be caused, for instance, by the connection between the TDR unit and the cable, by the cable-to-probe connection, and by the plastic ring insertion in the probe head. They cause a periodical presence of parasitic multiple reflections of TDR waveforms. For example, in Fig. 4.3, it can be noticed that the effects of parasitic multiple reflections are clearly detectable at longer distance after the probe-end point (approximately 4.9 m). Considering the distance where it occurs, this effect is attributable to the repetition of the reflection occurring at the probe head section; however, this does not play a dominant role in terms of error contribution for the considered application.

4.2.3 Validation of the Method on Dielectric Liquids

The TDR-based method was tested on four liquids (with different levels), which were representative of ‘high’ (de-ionized water), ‘medium’ (acetone), and ‘low’ (diesel oil and fuel) permittivity values. These liquids have negligible ionic conductivity and relaxation effects in the considered frequency range (0–1.7 GHz). The liquids were placed inside a cylindrical sample holder, and their level (H_{ref}) was measured directly from the reading of the 1000 ml-graduated sample holder.

TDR measurements were performed through the HL1500; the number of measurement averages for the acquisition was 10, and the number of acquired points was 2048. The TDR waveforms for the considered liquids are shown in Fig. 4.4. The significant reflections, clearly shown by the derivative curves, correspond to coaxial cable-to-probe connection, to the air-liquid interface, and to the probe-end point. The distance differences between the probe-end peaks and the air-liquid interface peaks (located through the analysis of derivative data for each sample), give the apparent liquid lengths.

It is important to point out that, for evaluating the dielectric constant from (4.1), the reflection coefficient value should be retrieved from the steady-state portion of the TDR waveform, as long as the low-loss non-dispersive liquid assumption can be considered valid.

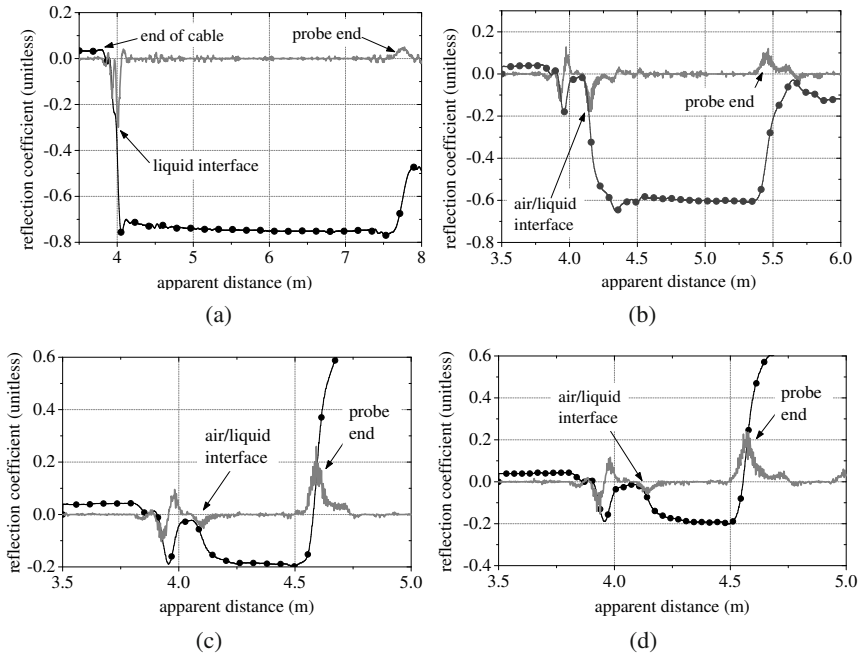


Fig. 4.4 TDR waveform (black line with dots) and derivative of data (gray line). **a** for a 41.3 cm level of de-ionized water sample [probe completely full]. **b** for 27.2 cm level of acetone sample. **c** for 32.1 cm level of fuel sample. **d** for 27.8 cm level of diesel oil sample

For each liquid the following data were evaluated:

- 1. the TDR-measured apparent liquid level, H_{app} ;
- 2. the measured reflection coefficient, ρ_{meas} ;
- 3. the corrected reflection coefficient according to (4.4), ρ_{corr} ;
- 4. the square root of the calculated dielectric constant $\sqrt{\epsilon_{app}}$; and, finally,
- 5. the actual liquid level, H_{meas} .

To provide a simple performance assessment of the method, the relative percentage difference between reference and measured liquid levels was calculated:

$$\Delta H = |H_{ref} - H_{meas}| 100 / H_{ref} \cdot \tag{4.5}$$

The results for level and dielectric constant estimation are summarized in Table 4.1: it is worth noting that the experimental results for the level measurements show a very good agreement with the reference levels; similarly, the measured dielectric constant values agree with those reported in [18].

Table 4.1 Summarized results obtained from TDR measurements for the estimation of levels and dielectric constants of liquid samples reported in Fig. 4.4 (de-ionized water, acetone, fuel, and diesel oil)

H_{ref} (cm)	probe end point (cm)	probe-to-liquid interface point (cm)	H_{app} (m)	ρ_{meas}	ρ_{corr}	$\sqrt{\epsilon_{app}}$	H_{meas} (cm)	ΔH (%)
<i>deionized water</i>								
41.3	776.5	401.0	375.5	-0.75	-0.80	8.97	41.8	1.2
<i>acetone</i>								
27.2	546.5	416.7	129.8	-0.61	-0.65	4.71	27.6	1.5
<i>fuel</i>								
32.1	459.0	411.0	48.0	-0.18	-0.19	1.47	32.6	1.5
<i>diesel oil</i>								
27.8	457.2	415.0	42.7	-0.19	-0.20	1.50	28.1	1.1

4.2.3.1 Measurements on Stratified Liquids

The proposed measurement system was also validated for measurements of the levels of stratified liquids (which can be particularly useful in the field of petrochemical, chemical, or agro-food, industrial processing control purposes). In this case, measurements were performed with the probe-end termination short-circuited.

A 27.5 cm-high diesel oil layer was considered on a 9.5 cm-high tap water sample: the corresponding TDR waveform is reported in Fig. 4.5. The measured

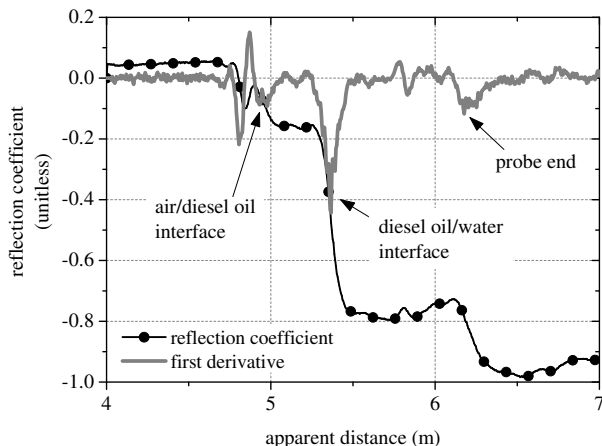


Fig. 4.5 TDR waveform and derivative of data for a diesel oil-tap water layered sample (short-circuited probe-termination)

apparent height for tap water, H_{app}^{water} , was 81.1 cm, and the corrected reflection coefficient was -0.8, corresponding to the expected value of dielectric constant ($\epsilon_{water} \cong 80$). Also the third reflection related to diesel oil-water interface could be directly evaluated as difference between the total coaxial probe length, the coaxial probe in air portion and the diesel oil distance.

4.3 Estimation of Levels and Permittivities of Industrial Liquids Using the TD/FD Approach

The simple TD approach described in the previous section provides adequately accurate results as long as the investigated liquids can be considered non-dispersive and lossless. Conversely, when the dependence of permittivity on frequency or the effect of losses cannot be neglected, to enhance the measurement accuracy, specific dielectric models (such as the Cole-Cole formula) have to be adopted for describing permittivity.

This can be achieved adopting a frequency-domain approach, thus considering the reflection scattering parameter, $S_{11}(f)$. As mentioned in Sect. 3.4, this parameter can be obtained either through direct frequency-domain measurements with a VNA or through an appropriate fast Fourier transform (FFT)-based processing of TDR data [5, 15, 17, 26].

On such bases, the approach proposed herein for the simultaneous estimation of liquid levels and of permittivity (in terms of Cole-Cole parameters), relies on FD data and on the transmission line (TL) modeling of the measurement cell (i.e., probe + LUT). In particular, the measurement cell is modeled as a function of the

‘unknown’ Cole-Cole parameters of the liquid filling the probe and of the ‘unknown’ liquid levels. Through the minimization (over the unknown variables) between the measured scattering parameter ($S_{11,MEAS}$) and the scattering parameter of the TL model ($S_{11,MOD}$), the proposed procedure provides the accurate evaluation of the Cole-Cole parameters and of liquid levels. Furthermore, this procedure can be extended to stratified liquids [22].

As will be detailed later, an additional accuracy enhancement was obtained by realizing an *ad-hoc* fixture that would allow performing short-open-load (SOL) calibration measurements, which are essential to reduce the effect of systematic errors (as seen in subsection 3.6.2).

Experimental measurements were performed considering different levels of layered samples (fuel/tap water). Since both fuel and tap water exhibit a strong dispersive behavior (especially, the imaginary part of their complex permittivity), a complete spectral picture of the frequency-dependent dielectric properties can be obtained through the five-parameter Cole-Cole formula.

4.3.1 Transmission Line Modeling of the Measurement Cell

The approach proposed herein is based on the adoption of a TL model of the measurement cell. As aforementioned, the complex relative permittivity of fuel and water, ϵ_r^* , can be appropriately modeled through the Cole-Cole formula. Such a function, both for fuel and water, is incorporated in the $S_{11}(f)$ multiple-reflection model described by (3.26), through (3.27)-(3.29). The TL model is parameterized also as a function of the unknown liquid levels.

On such bases, as reported in in subsection 3.6.4, the minimization (over the unknown variables) of the squared difference between the measured, $S_{11,MEAS}(f)$, and the modeled scattering parameters, $S_{11,MOD}(f)$, leads to the estimation of the Cole-Cole parameters and of the corresponding liquid levels. For the adopted

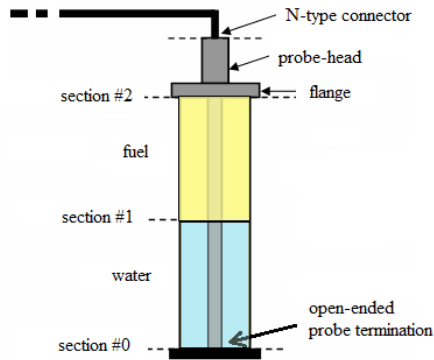


Fig. 4.6 Schematic representation of the measurement cell and of the corresponding main sections used for modeling the $S_{11}(f)$

measurement setup, the considered multi-section TL model comprises three sections: section 0 is the probe termination, section 1 corresponds to the probe portion filled with water, and section 2 corresponds to the portion filled with fuel.

To estimate the input scattering parameter $S_{11}^{k=2}(f)$ of this multi-section TL model, the value of the reflection coefficient at the termination has to be assumed. The used probe has an open-ended configuration and, therefore, $S_{11}^{k=0} = 1$ is assumed. Starting from this value and using (3.26), firstly for section 1 and then for section 2, the input scattering parameter can be obtained. It is worth noting that $\Gamma^{k=1} = 1$, due to the open-ended termination, while $Z_{0,k} = 50 \Omega$ for all the remaining sections (due to the specific probe design).

The proposed model was implemented within the commercial microwave circuit simulator AWR Microwave Office (MWO), which also makes optimization routines directly available. In particular, the chosen objective function to be minimized is the sum of the squared magnitude of the differences between the measured and the MWO-modeled scattering parameters.

This way, since the Cole-Cole formula is included in the modeled scattering parameter, along with the liquid level, the minimization of the objective function successfully provides an accurate estimation of the five dielectric parameters (over the considered frequency range) and of the levels of liquids.

It must be pointed out that the optimization is rather complex because of the large number of parameters involved: the fuel level (the water level is constrained to the difference between the known probe length and the fuel level), four Cole-Cole parameters for the fuel (the static conductivity is constrained to 0 Sm^{-1}), and five Cole-Cole parameters for the water. The optimum Cole-Cole parameters and levels for fuel and water are evaluated through the following three-step optimization procedure:

1. the Cole-Cole parameters for water and fuel are fixed at reasonable *initial guess* values (the dielectric properties of water are well known once the temperature is measured), thus the fuel level is optimized. This gives a reasonable initial guess for the fuel level;
2. starting from the previous values, all parameters are optimized through a *random optimization* procedure that should take the objective function close to the global minimum and should guarantee that the subsequent optimization step does not fall into a local minimum;
3. using the previous results as the new starting inputs, a simplex optimization procedure is applied, which forces the objective function to the final global minimum.

The robustness and efficiency of the proposed procedure will be shown in the next subsections.

4.3.2 Measurement Setup and Enhanced Probe Design

As aforementioned, the probe configuration design plays a crucial role in terms of measurement accuracy. In fact, any impedance mismatch in the TL may affect the

evaluation of the liquid dielectric properties and levels. To circumvent this problem, the optimal strategy should simultaneously involve a suitable calibration procedure and a good impedance matching of each component of the measurement setup.

In this regard, the most critical component to be designed is the probe-head section, which should guarantee a perfectly matched cable-to-probe connection, as well as the mechanical stability of the probe central conductor. Additionally, the probe-head structure should be included in the SOL calibration measurements, in order to de-embed its effect and to accurately derive the response related only to the probe section filled with the sample under test. As a matter of fact, all these requirements were considered in the design of the enhanced configuration of the coaxial probe. Fig. 4.7 shows the 433 mm long coaxial probe, the 160 mm long probe-head portion as well as the calibration structure that exactly reproduces the internal probe-head portion: all these components are virtually $50\ \Omega$ -matched, as explained in the following. For this probe, the inner and outer diameters of the probe conductors ($a = 9\text{ mm}$ and $b = 21\text{ mm}$, respectively) were chosen, once again, to ensure a $50\ \Omega$ -matched characteristic impedance when the probe is in air, according to (3.14).

The chosen dimensions limit the frequency bandwidth of the probe to about 6 GHz, when the dielectric material considered is air. However, when the probe is inserted into a different material, this limit decreases proportionally to the square root of the dielectric permittivity of the material. In particular, for the considered cases, the liquid with the highest permittivity is water, which limits the useful bandwidth of the probe to approximately 700 MHz.

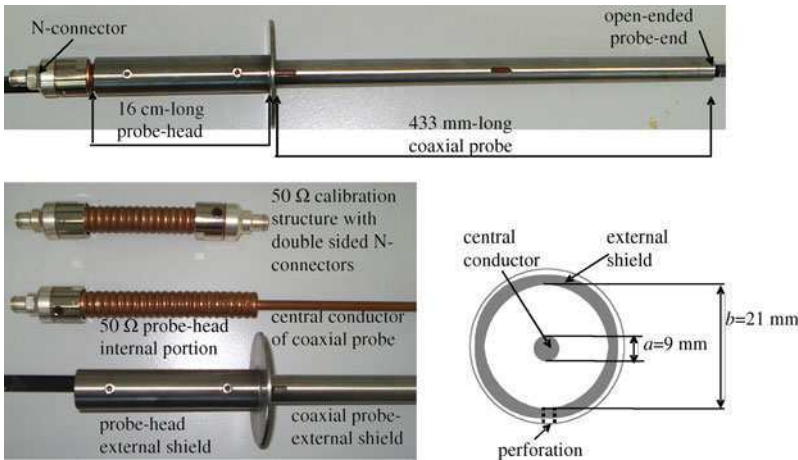


Fig. 4.7 Coaxial probe external configuration, details of calibration structure, internal probe head and inner probe conductor, external probe head shield and external probe shield, cross-section probe dimensions [22]

The probe-head internal portion is made up of a $50\ \Omega$ foam-dielectric coaxial cable (Cellflex LCF78-50JA), contained in the stainless steel outer conductor that is ground contacted. The 433 mm-long inner conductor of the probe is obtained removing the same length of the external shield and foam dielectric of the Cellflex cable.

As aforementioned, to perform a SOL calibration at the exact section where the sensing element begins (section #2 of Fig. 4.6), a calibration structure reproducing the internal probe-head portion was specifically realized. This structure terminated with an N-type connector (thus ensuring the connection to N-type SOL standards).

For the time-domain measurements, the HL1500 unit was used. Comparative frequency domain measurements were performed through the Agilent E8363B VNA, whose upper operating frequency is 40 GHz. The probe was connected to the TDR and to the VNA instrument through a 3 m-long RG213 coaxial cable.

The HP85032B N-type SOL standard calibration kit was used for calibration measurements, both for VNA and TDR measurements. In particular, the SOL kit standards were connected at the end of the ‘calibration structure’ (which was connected to the instrument through the 3 m-long cable as well). In this way, all the parasitic effects caused by the probe-head (and, consequently, also of the cable) were adequately compensated for.

4.3.3 Experimental Validation of the Method

To assess the method, measurements were performed on stratified liquids, namely fuel/tap water layered samples. Three samples were considered. All measurements were performed at room temperature ($26 \pm 1^\circ\text{C}$). The three samples differed in the relative level of fuel and water, as shown in Table 4.2. First, the apparent dielectric

Table 4.2 Reference level of fuel (H_f^{ref}) and tap water (H_w^{ref}), for the three considered samples

	H_f^{ref} (mm)	H_w^{ref} (mm)
Sample #1	283.0 ± 0.5	150.0 ± 0.5
Sample #2	219.0 ± 0.5	214.0 ± 0.5
Sample #3	335.0 ± 0.5	98.0 ± 0.5

constant and the levels were estimated through the time-domain approach presented in the previous section.

Secondly, the dielectric permittivity and the levels were evaluated by resorting to the proposed TL modeling and optimization procedure. For comparison, this TL-based approach was applied separately to two sets of data: to the scattering

parameter derived directly from VNA measurements ($S_{11,MEAS}^{yna}$) and to the scattering parameter derived from the FFT of TDR data ($S_{11,MEAS}^{fft}$).

In this way, it was demonstrated that the measurement accuracy in the evaluation of levels and dielectric permittivity is substantially improved with respect to the simple time-domain approach. Additionally, it was also shown that the TD/FD combined approach can provide as much accuracy as direct VNA measurements.

Finally, it is important to highlight that, for all the TDR and VNA measurements, the SOL calibration procedure (with the calibration structure connected at the end of the feeding coaxial cable) was performed, according to the calibration error model reported in subsection 3.6.2 [5]. Additionally, also the TDR measurements were calibrated, according to the time-domain calibration procedure described in subsection 4.2.2.

4.3.3.1 Time-Domain Approach

As mentioned in the previous section, the apparent dielectric permittivity of fuel, $\epsilon_{app,f}$, was extrapolated from the amplitude of the first reflection in the TDR waveform, caused by the air-to-fuel impedance change. As an example, Fig. 4.8 shows the TDR waveform (together with its derivative), when the probe was immersed in sample #1. As highlighted in the figure, the significant reflection points are associated to the level estimation derived from the distance difference between peaks of the derivative curve. Based on the $\epsilon_{app,f}$ evaluation and measuring the apparent distance associated to the fuel, the fuel level (H_f^{td}) was determined from (4.2).¹

The water level, H_w^{td} , was therefore simply derived from the difference between the overall probe length and the estimated actual fuel level. Table 4.3 summarizes the results obtained solely from the TDR waveforms analysis described in the previous section [6, 7]. The deviation between reference values and the TDR-estimated values is also reported.

Table 4.3 Summarized results, obtained through the TD-based approach, for the three considered samples. The apparent permittivity of fuel ($\epsilon_{app,f}$), the estimated level of fuel (H_f^{td}), and the estimated level of tap water (H_w^{td}) are reported. Deviations of estimated levels from reference levels are also reported

	$\epsilon_{app,f}$	H_f^{td} (mm)	H_w^{td} (mm)	deviation (mm)
Sample #1	2.23	281	152	± 2
Sample #2	2.22	219	214	0
Sample #3	2.23	331	102	± 4

¹ The apex *td* indicates that results were obtained from time-domain measurements only.

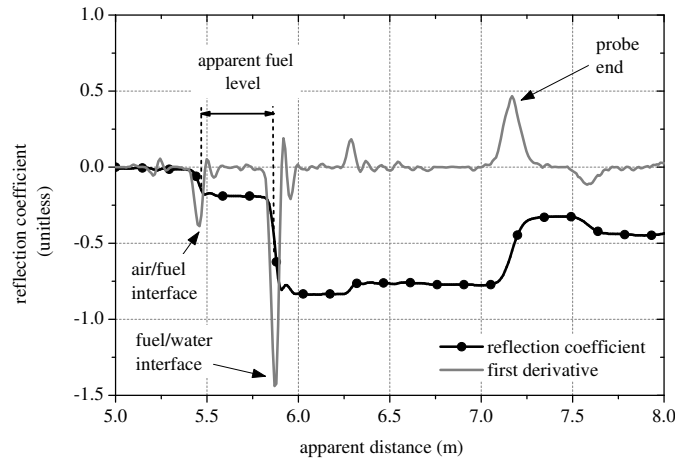


Fig. 4.8 Reflection coefficient (and corresponding first derivative) acquired with the probe immersed in sample #1

4.3.3.2 Frequency-Domain Approach

For a preliminary validation of the minimization algorithm, the reference parameters for the three samples of liquids were used to generate the ideal scattering parameters: the modeled $S_{11}(f)$ would correspond to those that would be measured under ideal conditions, that is without any uncertainty due to imperfect calibration, imperfect equipment, noise, etc.(see Table 4.4). These ideal scattering functions were considered as the input for the subsequent optimization routine, thus obtaining the extrapolated results reported in Table 4.4. Analysis of the data reported in Table 4.4

Table 4.4 Fuel level (H_f), water level (H_w), and Cole-Cole parameters extrapolated from ‘simulated’ frequency-domain measurements and compared to reference values

	Sample #1		Sample #2		Sample #3	
	Ref.	Extr.	Ref.	Extr.	Ref.	Extr.
$\epsilon_{s,f}$	2.35	2.35	2.35	2.35	2.35	2.35
$\epsilon_{\infty,f}$	2.02	2.03	2.02	2.13	2.02	1.99
$f_{r,f}$ (GHz)	13.0	12.1	13.0	6.6	13.0	14.9
β_f	0.25	0.25	0.25	0.20	0.25	0.25
H_f (mm)	283.0	283.0	219.0	219.0	335.0	334.9
$\epsilon_{s,w}$	79.8	79.8	79.8	79.8	79.8	79.7
$\epsilon_{\infty,w}$	5.2	6.1	5.2	6.1	5.2	3.9
$f_{r,w}$ (GHz)	17.3	17.1	17.3	17.1	17.3	18.5
β_w	0.00	0.00	0.00	0.00	0.00	0.02
$\sigma_{0,w}$ (mS m ⁻¹)	2.58	2.58	2.58	2.59	2.58	2.44
H_w (mm)	150.0	150.0	214.0	214.0	98.0	98.1

shows that, due to the limited measurement bandwidth (from 10 MHz to 700 MHz), the evaluation of ϵ_∞ and of f_r is somewhat less accurate. On the other hand, both the ϵ_s and, most importantly, the liquid levels are estimated with high accuracy. This demonstrates that the proposed setup is definitely suitable to estimate the static permittivity and level of fuel.

When ϵ_∞ and f_r are of interest, the probe design should be modified, and a coaxial probe with smaller radius should be adopted in order to achieve larger working bandwidths, without any modification in the optimization procedure (this case will be considered in Sect. 4.4).

After the proposed optimization technique was tested on the idealized data, demonstrating its reliability and accuracy, it was applied to ‘real’ measurements performed on the same samples. In particular, the procedure was implemented considering as input first the scattering parameter directly measured by the VNA, and successively, the one obtained through the FFT-based algorithm of TD data (i.e., the TD/FD combined approach) [5]. The obtained results are reported in Table 4.5 and Table 4.6 for VNA and FFT data, respectively. Analysis of the two tables demonstrates that the optimization procedure can suitably estimate fuel and water levels with a maximum deviation within the uncertainty in the evaluation of the reference levels. In particular, it is important to point out that the TD/FD combined approach does not cause substantial accuracy decrease with respect to the VNA measurements. This confirms that a low-cost TDR system, associated to the

Table 4.5 Fuel static permittivity, fuel level, and water level extrapolated for the three samples using frequency-domain minimization routine, applied on VNA measurements. Deviations from reference levels are also reported

	$\epsilon_{s,f}^{vna}$	H_f^{vna} (mm)	H_w^{vna} (mm)	deviation (mm)
Sample #1	2.37	283.5	149.5	± 0.5
Sample #2	2.24	219.5	213.5	± 0.5
Sample #3	2.17	335.1	97.9	± 0.1

Table 4.6 Fuel static permittivity ($\epsilon_{s,f}^{fft}$), fuel level (H_f^{fft}), and water level (H_w^{fft}) extrapolated for the three samples using frequency-domain minimization routine, applied on FFT of TDR measurements. Deviations from reference levels are also reported

	$\epsilon_{s,f}^{fft}$	H_f^{fft} (mm)	H_w^{fft} (mm)	deviation (mm)
Sample #1	2.21	282.7	150.3	± 0.3
Sample #2	2.18	219.3	213.7	± 0.3
Sample #3	2.16	334.7	98.3	± 0.3

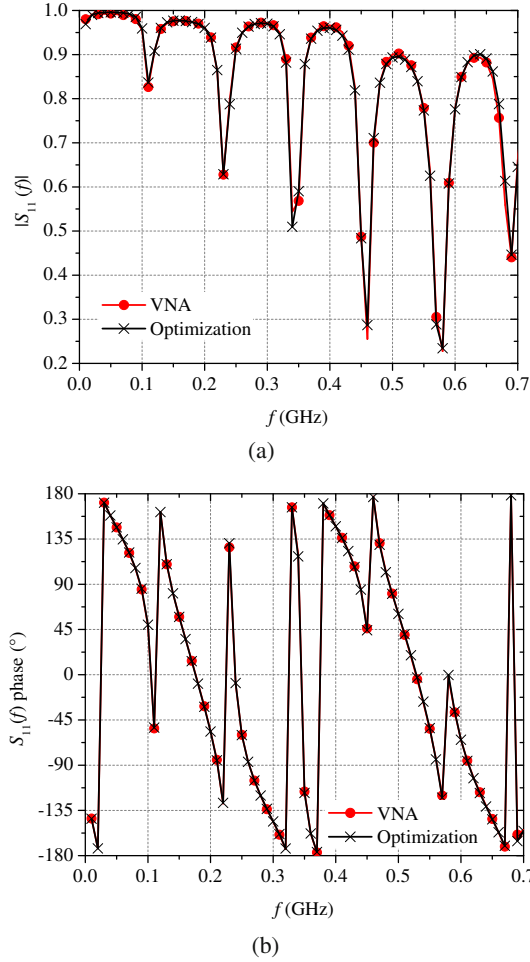


Fig. 4.9 Reflection scattering parameter for sample #1 as obtained from VNA measurements and evaluated through the optimization procedure. **a** magnitude. **b** phase

proposed procedure, is the key issue for the practical implementation in industrial-related applications. On a side note, the decreasing trend of static permittivity from sample #1 to sample #3 can be explained by the steady increase of room temperature during the experimental session. However, temperature increase was so small to cause only minimal changes in static permittivity, not detectable in the TDR traces, which only allow an approximate average permittivity (ϵ_{app}) to be estimated. As a matter of fact, this confirms the suitability of the frequency-domain approach also

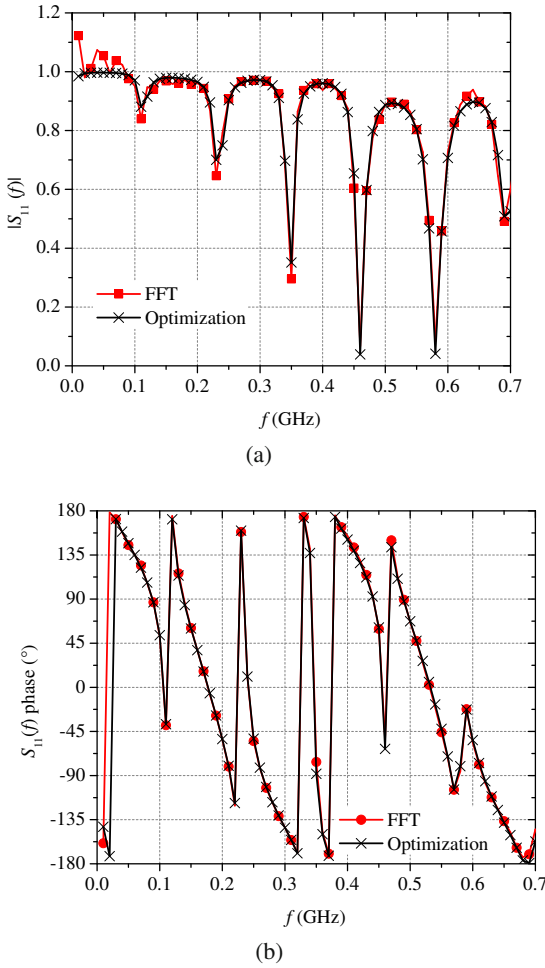


Fig. 4.10 Reflection scattering parameter for sample #1 as obtained from FFT of TDR measurements and evaluated through the optimization procedure. **a** magnitude. **b** phase

for sensing small deviations from the standard reference status, even when they are caused by the temperature variations.

As an example, Fig. 4.9 and Fig. 4.10 compare the optimized $S_{11}(f)$ for sample #1, with measurements obtained from VNA and from the TD/FD combined approach, respectively.

It is worth noting that, although the $S_{11}(f)$ directly obtained from VNA measurements, as expected, appears to be less noisy than the $S_{11}(f)$ obtained from the TD/FD combined approach, this does not have any relevant impact on the accuracy in the evaluation of quantitative and dielectric parameters.

4.3.3.3 Validation of the Robustness of the Procedure

It is important to point out that the adopted optimization procedure converges to a final solution that depends on the initial estimates and on the intermediate convergence point of the random part of the optimization procedure itself. To assess the robustness of the overall procedure, it was repeatedly applied to the same sample, slightly varying the initial guesses for the Cole-Cole parameters of water and fuel. The obtained results, in terms of extrapolated fuel levels, show dispersion within 0.1 mm, thus demonstrating the robustness of the procedure. To summarize the obtained results and to compare the different methods, Table 4.7 compares the fuel levels extrapolated from the time-domain and from the two frequency-domain approaches, with the reference values.

Table 4.7 Reference and extrapolated fuel levels, in time-domain and frequency-domain approaches, for the three samples

	reference	time domain	Fuel level (mm)	
			frequency domain (VNA)	frequency domain (TD/FD combined approach)
Sample #1	283.0	281	283.5	282.7
Sample #2	219.0	219	219.5	219.3
Sample #3	335.0	331	335.1	334.7

The total time required for the optimization (encompassing the steps outlined) was of the order of 10 minutes.

Indeed, the time required for optimization might be dramatically reduced by using a customized software routine rather than resorting to the commercial circuit simulator.

It is worth mentioning that, in a practical monitoring application, after the first run of the optimizer has been completed and initial Cole-Cole parameters and liquid levels have been estimated, the continuous monitoring simply requires the optimizer to track the small changes in dielectric parameters and level that occur in time. This means that the further optimizations will only require a few iterations of the simplex algorithm, which however should not take more than a few seconds².

² As a matter of fact, different minimization methods, such as the globalized bounded Nelder-Mead (GBNM), can be alternatively used. Nevertheless, this would probably improve the efficiency of the first run, but would probably have no relevant impact in the subsequent continuous monitoring, when the optimization routine should just track smooth temporal variations in liquid levels and permittivities.

4.4 Dielectric Spectroscopy of Edible Liquids: The Vegetable Oils Case-Study

As previously discussed, the in situ evaluation of the Cole-Cole parameters is not an easy task, especially when reference data are missing. This is the case, for example, with vegetable oils, for whose dielectric characteristics only scarce reference data are available [19, 23]. In fact, the complexity of the intrinsic characteristics of vegetable oils, such as density and viscosity, makes the investigation of this kind of material rather challenging, nonetheless interesting. Additionally, since quality control of vegetable oils is becoming more stringent (especially for avoiding adulteration), the estimation of these dielectric parameters may be used as a reliable indicator for certifying the product quality.

It is worth pointing out that although highly sophisticated methods for the analysis of edible oils are available, many of them are not easily applicable for routine or continuous monitoring (e.g., gas chromatography [20] and liquid chromatography [9]), whereas others (e.g., Fourier transform infrared (FTIR) [25], Raman spectroscopy [14], and nuclear magnetic resonance (NMR) [24]) are rather complex and highly expensive. On the other hand, other simpler methodologies that are commonly adopted for routine analysis (such as those based on chemical titrations), do not provide much information. Additionally, these methods of analysis require skilled operators, and, most importantly, they cannot provide any information about the possible presence of adulterants. As a matter of fact, all of aforementioned methods are affected by some limitations: in particular, they cannot be performed on the process line and they are very laborious.

On such bases, not only does the presented case study aim at providing a preliminary assessment of the use of microwave dielectric spectroscopy for the characterization of vegetable oils, but it also investigates the possibility of adopting a suitable measurement procedure for a rapid and reliable evaluation of dielectric parameters. This is done in view of possible practical applications, which may be useful, for example, in the on-line monitoring of the characteristics of oils throughout a production process.

The approach proposed for the accurate evaluation of the Cole-Cole parameters is based on a procedure similar to the one described in the previous section, and it comprises three major steps:

- First, the TDR waveforms are acquired and processed in order to obtain the corresponding reflection scattering parameter, $S_{11}(f)$;
- Secondly, the measurement cell (i.e., probe and filling liquid) is accurately modeled as a TL, in which the dielectric characteristics of the considered liquid are parameterized through the Cole-Cole formula;
- Finally, the Cole-Cole parameters of the LUT are evaluated by minimizing the deviations between 1) the measured reflection scattering parameter, $S_{11}(f)$,

obtained from the TD/FD approach; and 2) the modeled reflection scattering parameter obtained from the implemented TL model of the probe plus LUT, $S_{11,MOD}(f)$.

It is worth pointing out that, for this specific monitoring purpose, the TL model includes has to include not only the Cole-Cole parameters of the LUT as minimization variables, but also some lumped circuit elements that account for additional parasitic effects that cannot be compensated for through traditional SOL calibration procedures.

This procedure was first tested and validated on well-referenced liquids, and successively it was applied for the evaluation of the Cole-Cole parameters of oils. The main steps of the procedure are similar to those in the diagram in Fig. 3.19 and will be described in detail in the following subsections.

To define the performance characteristics of this combined approach (particularly, in terms of repeatability and uncertainty), a rigorous metrological validation was also carried out through measurements on well-referenced materials.

TDR measurements on vegetable oils were carried out through the TDR80E04. However, in view of possible practical implementation, it is worth underlining that the procedure described herein also apply for portable TDR instrumentation.

4.4.1 *Design of the Measurement Cell and Transmission Line Modeling*

Although the SOL calibration is the first strategy for reducing the systematic error contributions, a further accuracy enhancement must take into account the parasitic effects associated with the measurement cell. For this purpose, an accurate TL modeling of the specific measurement cell represents a successful key for a further enhancement of the final measurement accuracy. The implemented TL model must include all the undesired effects (e.g., undesired impedance mismatches) that inevitably influence the measurements.

A picture of the probe designed for this specific application is shown in Fig. 4.11.

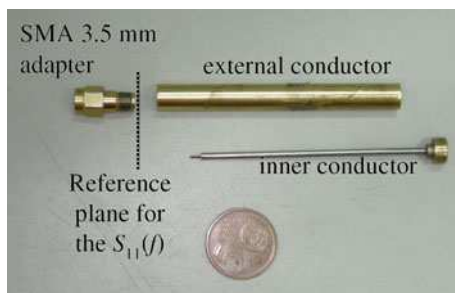


Fig. 4.11 Picture of the used coaxial probe

The probe was short-circuited at the distal end; the schematic configuration of the probe is shown in Fig. 4.12.

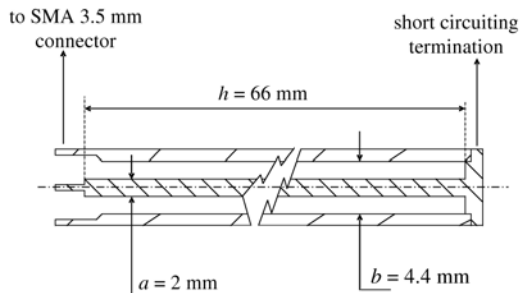


Fig. 4.12 Schematic configuration of the used coaxial probe.

The TL model of the measurement cell was implemented in the MWO simulator. The basic TL model includes a length of short-circuited coaxial probe, with the physical dimensions of the actual probe, filled with a material characterized through its relative permittivity and loss tangent (whose frequency-dependent variation is described by (2.38)).

Preliminary TDR measurements on well-referenced materials showed that two major parasitic effects were apparent in the acquired waveforms: one is caused by the transition probe/SMA connector, whereas the other is due to the non-ideality of the short circuit at the end of the probe. Therefore, to take into account these parasitics, the TL model was appropriately adjusted; in particular, the introduction of some lumped circuit elements appropriately resembled the contributions noticed in the actual measurements.

In order to obtain a TL model where the only variable parameters would be the Cole-Cole parameters of the LUT, the first step was the optimization of the model (i.e., the individuation of the values of the added lumped elements). For this purpose, preliminary measurements were carried out on three well-referenced materials, namely 1,1,1-trichloroethane, ethyl acetate, and air: for these materials, the Cole-Cole parameters were taken from the related literature [3] and were considered as known values. Through an optimization procedure detailed in Sect. 4.3.1, the squared deviations between the measured $S_{11}(f)$ and the modeled $S_{11,MOD}(f)$ were minimized, thus estimating the values of the lumped elements that appropriately described the parasitics of the measurement cell.

Minimization was performed over a frequency range³ that goes up to 4 GHz. As an example, Fig. 4.13 shows the comparison between the measured $S_{11}(f)$ and the

³ Preliminary minimization routines were performed over different frequency ranges, and the 0-4 GHz frequency range proved the optimal frequency range both in terms of minimum of the objective function of the minimization and in terms of appropriateness of the optimized circuit elements.

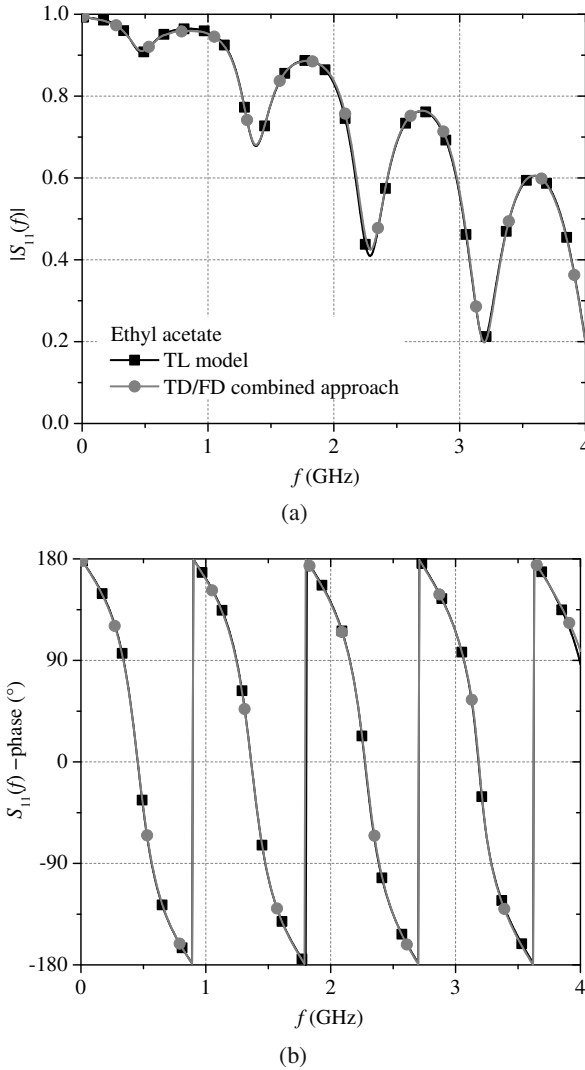


Fig. 4.13 Comparison between the modeled scattering parameter (*black squares*) and the measured $S_{11}(f)$ (*grey dots*), for ethyl acetate. **a** magnitude. **b** phase. The *rmse* between the TL-modeled $S_{11}(f)$ and the measured $S_{11}(f)$ is 0.006, over the 0-4 GHz frequency range [8]

modeled $S_{11, \text{MOD}}(f)$ (after the minimization procedure was carried out) for ethyl acetate: it can be seen that the reflection scattering parameter obtained from the TL model closely agrees with the measured scattering parameter, both in magnitude and phase. The root mean square error (*rmse*) between $S_{11}(f)$ and $S_{11, \text{MOD}}(f)$ was evaluated as a figure of merit, and its value was 0.006.

The final TL model and the values of the added lumped (parasitic) elements are shown in Fig. 4.14. In the implemented model, TL_1 represents the SMA 3.5 mm adapter; TL_2 represents the probe filled with the LUT; C_1 , L_1 represent the non-ideal transition adapter/probe; and R_1 , R_2 , L_2 represent the non-ideal short circuit at the end of the probe. C_1 is proportional to the real part of the dielectric permittivity of the considered liquid, $\text{Real}(\epsilon_{\text{liquid}}^*)$.

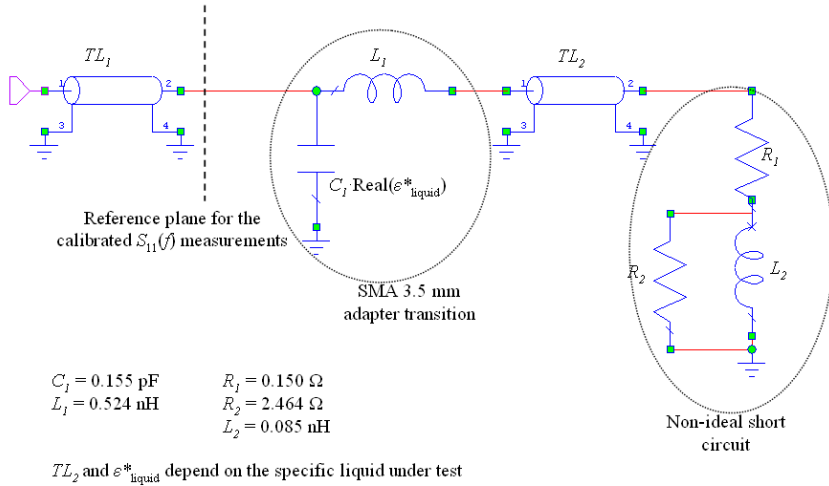


Fig. 4.14 Transmission line model (as implemented in MWO) of the used measurement cell [8]

4.4.1.1 Validation of the Method through Measurements on Well-Referenced Materials

The appropriateness of the TL model in estimating the Cole-Cole parameters of the LUTs was verified through further measurements on 1,1,1-trichloroethane and ethyl acetate. In this case, starting from the implemented TL model (now including all the evaluated parasitic components), the Cole-Cole parameters of the liquid were considered as the minimization variables. TDR measurements (along with the corresponding frequency domain processing and minimization) were repeated ten times for each considered material (each time, by emptying and refilling the probe).

In this way, it was possible to assess the repeatability of measurements and to reduce random errors contributions. The four evaluated Cole-Cole parameters are summarized in Table 4.8 and Table 4.9 (static conductivity is negligible for both liquids); each set of parameters was evaluated as the average of the results of ten minimizations over the ten measurements. In order to identify a figure of merit for the

metrological performance of the entire measurement procedure, the type A evaluation of the uncertainty (u_A) was conducted for each Cole-Cole parameter, according to the following expression [16]:

$$u_A = \sqrt{\frac{1}{n(n-1)} \sum_{i=1}^n (x_i - \bar{x})^2} \tag{4.6}$$

where n is the number of measurements, x_i is the result of each evaluated parameter, and \bar{x} is the average of the n repetitions. In the measurements reported herein, the number of repetitions n is 10.

Table 4.8 Comparison between the reference and the evaluated Cole-Cole parameters (at 20.0°C) for ethyl acetate. The experimental uncertainties for the evaluated values are also reported

ethyl acetate			
parameter	reference value [3, 11]	averaged evaluated value	experimental uncertainty
ϵ_s	6.04 ± 0.02	6.00	0.01
ϵ_∞	2.48 ± 0.09	2.71	0.10
f_r (GHz)	36.2 ± 0.8	29.6	1.0
β	0.06 ± 0.01	0.00	0.00

Table 4.9 Comparison between the reference and the evaluated Cole-Cole parameters (at 20.0°C) for 1,1,1-trichloroethane. The experimental uncertainties for the evaluated values are also reported

1,1,1-trichloroethane			
parameter	reference value [3, 11]	averaged evaluated value	experimental uncertainty
ϵ_s	7.20 ± 0.10	7.25	0.02
ϵ_∞	2.08 ± 0.02	2.12	0.15
f_r (GHz)	28.9 ± 0.6	26.7	0.9
β	0.030 ± 0.002	0.00	0.00

From Table 4.8 and Table 4.9 the calculated values of the static permittivity (ϵ_s) closely agree with those reported in the literature; additionally, the corresponding experimental uncertainty (u_A) is remarkably low. Similarly, the values obtained for ϵ_∞ and for f_r are in good agreement with the literature values (which were obtained

through VNA-based measurements), despite being affected by a higher uncertainty. The higher uncertainty is most probably due to the fact that the relaxation frequencies of 1,1,1-trichloroethane and of ethyl acetate are much higher than the upper limit individuated for the optimization of the model (i.e., 4 GHz) and even higher than the frequency limit of the used TDR instrument (i.e., 15 GHz). In fact, additional measurements on ethanol (whose f_r is in the order of 1 GHz) [12], provided accurate results for all the four Cole-Cole parameters, thus validating the appropriateness of the proposed procedure. The four Cole-Cole parameters for ethanol and the related experimental uncertainties are reported in Table 4.10.

Table 4.10 Comparison between the reference and the evaluated Cole-Cole parameters (at 20.8°C) for ethanol. The experimental uncertainties for the evaluated values are also reported

ethanol			
parameter	reference value [12]	averaged evaluated value	experimental uncertainty
ϵ_s	25.04 ± 0.04	24.57	0.02
ϵ_∞	4.481 ± 0.027	4.15	0.05
f_r (GHz)	0.856 ± 0.004	0.92	0.01
β	0.00	0.00	0.00

4.4.2 Experimental Results for Vegetable Oils

When the proposed procedure was first applied to vegetable oils, the resulting values of the dielectric parameters were affected by a relatively high uncertainty. Additionally, the obtained results were rather different from the data available in the literature. In particular, the values of the relaxation frequencies were systematically overestimated.

The reason for this discrepancy could be mostly attributable to some intrinsic properties of the oils: these characteristics make the minimization over the four Cole-Cole parameters⁴ rather troublesome. In fact, oils are known to exhibit a relaxation frequency⁵ lower than 1 GHz; additionally, their dielectric properties anticipate a low value of the dielectric increment ($\epsilon_s - \epsilon_\infty$).

On such bases, to reduce the number of variables to optimize, the values of the static permittivity were assessed through an alternative method, and the minimization routine was performed over the remaining three Cole-Cole parameters (i.e., β , ϵ_∞ , and f_r). The evaluation of the ϵ_s of the oils was performed through independent capacitive measurements carried out with an LCR meter. This strategy was deemed as the best solution to obtain accurate results over the whole considered frequency range.

⁴ For vegetable oils, static electrical conductivity is practically zero.
⁵ As reported in [19], vegetable oils exhibit a first dielectric relaxation at approximately 1 MHz; however, this first relaxation was not considered in the analysis reported herein.

4.4.2.1 Evaluation of the Static Permittivity through LCR Measurements

LCR measurements were performed using the same coaxial probe, but removing the short circuit at the distal end. The probe (filled with the LUT) was considered as a cylindrical capacitor whose capacitance (C_{liquid}) ideally depends on the liquid filling the space between the cylindrical plates⁶, according to the following equation:

$$C_{\text{liquid}} = 2\pi\epsilon_0\epsilon_s^{\text{liquid}} \frac{h}{\ln(b/a)} \quad (4.7)$$

where ϵ_0 is the permittivity of free space; $\epsilon_s^{\text{liquid}}$ is the static permittivity of the LUT; h is the length of cylindrical plates (i.e., the length of the probe); a is the external diameter of the inner conductor; and b is the inner diameter of the external conductor.

The measured capacitance (C_{meas}) can be regarded as the parallel equivalent of three separate contributions:

$$C_{\text{meas}} = C_{\text{liquid}} + C_{\text{par}} + C_{\text{fr}} \quad (4.8)$$

where C_{par} is the parasitic capacitance (mostly due to the SMA adapter used to connect the probe), and C_{fr} is the capacitance due to the fringing field at the probe end [13]. LCR-based capacitive measurements with the probe in air at increasing frequencies showed that, after a slight initial decrease, above 1 kHz the measured capacitance was constant, thus indicating that the effect of parasitic and fringing capacitances was stable; therefore, measurements at 1 kHz were used to estimate the value of $C_{\text{par}} + C_{\text{fr}}$. This way, capacitance measurements on the materials under test could be corrected, thus obtaining C_{liquid} and the ϵ_s of the liquid sample.

Successively, the LCR-based approach for the evaluation of ϵ_s was validated through preliminary measurements on reference materials (i.e., ethyl acetate, 1,1,1-trichloroethane, chloroform); measurements were repeated ten times for each considered material, thus compensating for random errors contributions. Results for the evaluation of the values of ϵ_s are summarized in Table 4.11 and are compared to the literature values. The LCR-based method was used for the evaluation of the ϵ_s values of oils; also in this case, measurements were repeated ten times for each type of oil.

4.4.2.2 Evaluation of the Remaining Cole-Cole Parameters for Vegetable Oils

The values of the static permittivity were considered as known (fixed) values in the subsequent minimization routines carried out on FFT-transformed TDR data, employing the previously described approach: as expected, since these minimizations

⁶ LCR impedance measurements at low frequencies (i.e., at 1 kHz), confirmed the capacitor-like behavior of the probe; in fact, the phase angle of the impedance was -90° .

Table 4.11 Comparison between the reference and the LCR-evaluated values of ϵ_s , for the reference materials (at 20.0°C). Experimental uncertainty is also reported

material	reference value	bibliographic reference	averaged evaluated value	experimental uncertainty
chloroform	4.82 ± 0.02	[2, 11]	4.81	0.02
ethyl acetate	6.04 ± 0.02	[3, 11]	6.04	0.02
1,1,1-trichloroethane	7.20 ± 0.10	[3, 11]	7.42	0.04

were performed only on three Cole-Cole parameters, the accuracy of the final results was enhanced.

Also in this case, TDR measurements were repeated ten times for each type of oil; for each measurement, the minimization routine was performed and the corresponding values of ϵ_∞ , f_r and β were evaluated. The minimization procedure over the Cole-Cole parameters was performed on the 0–1 GHz frequency range; in fact, this frequency range was found to adequately include the major dielectric response of oils.

Ten different types of vegetable oils were considered: in particular, four olive oils with different acidity values (ranging from 0.3% to 4.0%) and six other kinds of vegetable oils (i.e., peanut, sunflower, corn, castor, various seed, and soybean).

Table 4.12 summarizes the Cole-Cole parameters for the ten oils (each set of parameters was calculated as the average of ten repetitions), and the corresponding standard deviation (σ). The obtained results for the Cole-Cole parameters of the considered vegetable oils are in good agreement with the few data available in the literature [10, 19, 23]. It is worth noting that, for the results obtained for oils, the standard deviation was reported (rather than the experimental uncertainty), so as to provide an indicator of the metrological performance of the method, when used without performing a series of repeated measurements.

As expected, from Table 4.12, it is apparent that β , ϵ_∞ , and ϵ_s change slightly among the different oils. Conversely, f_r seems to change significantly between one type of oil and another. To better evidence this trend, for each oil, Fig. 4.15 shows the expanded uncertainty range $\pm 2.26\sigma$; where σ is the standard deviation corresponding to the Gaussian probability distribution (which, in turn, was verified through the χ -square test). The expanded uncertainty was evaluated considering the t -distribution of Student, and 2.26 is the t -score that corresponds to a confidence level of 95% and to nine degrees of freedom [16]. On the basis of the obtained results, the proposed technique can be useful for quality monitoring of oils: for example, by measuring the relaxation frequency, it might be possible to discriminate different kinds of oil. Additionally, using the averaged relaxation frequency as a reference value (i.e., the expected value that the considered oil should exhibit), any deviation may be associated with the possible presence of adulterants.

Table 4.12 Averaged Cole-Cole parameters for the ten types of vegetable oil (at 20.0°C). Standard deviation values are also reported

type of oil	ϵ_s	σ_{ϵ_s}	ϵ_∞	σ_{ϵ_∞}	f_r (MHz)	σ_{f_r} (MHz)	β	σ_β
olive (ac.=0.3%)	3.08	0.01	2.39	0.01	315	11	0.33	0.01
olive (ac.=1.2%)	3.14	0.01	2.38	0.01	288	9	0.36	0.02
olive (ac.=1.6%)	3.19	0.03	2.36	0.01	259	4	0.40	0.01
olive (ac.=4.0%)	3.19	0.03	2.34	0.02	249	5	0.42	0.02
peanut	3.05	0.01	2.40	0.01	334	5	0.28	0.01
sunflower	3.12	0.04	2.40	0.01	292	5	0.31	0.01
corn	3.11	0.02	2.41	0.01	309	6	0.29	0.02
castor	4.69	0.01	2.56	0.01	122	2	0.42	0.01
various seeds	3.10	0.02	2.43	0.01	371	5	0.27	0.01
soybean	3.09	0.01	2.41	0.02	390	7	0.30	0.02

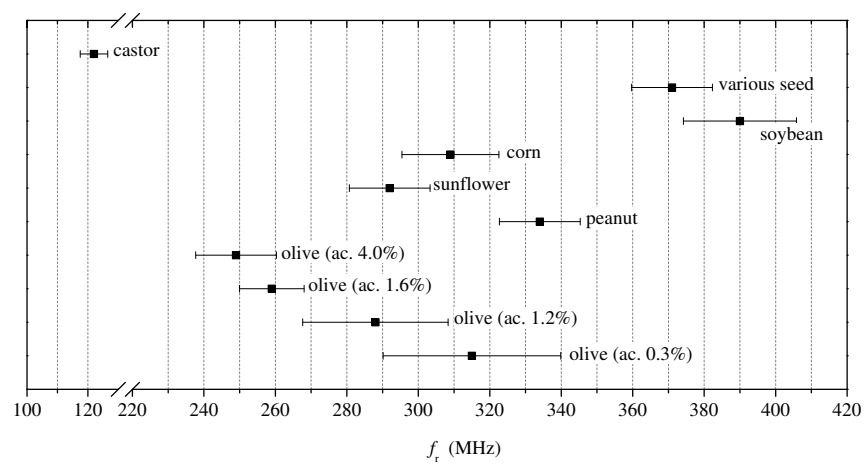


Fig. 4.15 Summarized comparative results of the averaged values of f_r for the considered oils. The corresponding expanded uncertainty bars (with a confidence level of 95%) are also reported

On a side note, it is important to point out a few aspects related to the used probe. Generally, a short probe provides several benefits: a lower attenuation of the electromagnetic signal is achieved, small volumes of liquid are required, and, finally, a higher mechanical stability between inner and outer conductors can be ensured. On the other hand, short probes do not provide enough electrical length for the electromagnetic signal in the LUT at low frequencies: this may represent an issue when determining the value of the static permittivity, ϵ_s . In this regard, the choice of the optimal length of the probe should start from preliminary considerations of

the intended purposes. As a matter of fact, the choice of the most appropriate probe length should guarantee an optimal trade-off of contrasting effects, such as an adequate performance at low frequency and the need to limit the quantity of oil required for performing the tests. This alternative solution may as well be regarded as a practical alternative for avoiding the use of the LCR meter for evaluating the static permittivity.

4.4.2.3 Results on Mixtures of Oils

After the validation of the proposed procedure for quality-control of pure olive oils, the successive phase was to extend the methodology to more complex systems (such as mixtures of oils), so as to test the method also for anti-adulteration control purposes.

On such bases, the proposed procedure was applied for the evaluation of the Cole-Cole parameters of some mixtures of oils (M1, ..., M4). In particular, to reproduce some typical adulteration cases, the mixtures were prepared by mixing a *new* olive oil with sunflower oil, in different volumetric percentages. Measurements were performed one single time for each mixture; this was done to mimic a typical practical case in which the personnel in charge of control have to rely on single-shot measurements. Summarized results are reported in Table 4.13. Also in this case, it is apparent that the parameter that is more sensitive to the change in the composition of the mixture is the relaxation frequency. More specifically, it can be seen that starting from pure olive oil, the relaxation frequency value increases proportionally to the percentage amount of sunflower oil. On the other hand, the remaining Cole-Cole parameters do not exhibit significant changes.

On a final note, it is worth noting that results show that the difference in f_r for the considered oil mixtures is of the order of a few MHz (see Table 4.13). This figure is comparable to the achievable uncertainty for measurements on pure oils, when single-shot measurements are performed (see Table 4.12). Overall, it appears that a further minimization of the uncertainty on f_r evaluation would be necessary to make the method more effective. This could be achieved, for example, exploiting enhanced probe geometries, as currently under development. Moreover, suitable

Table 4.13 Relaxation frequencies for the olive-sunflower oil mixtures

Mixture	Sunflower oil percentage (%)	f_r (MHz)
olive oil	0	245
M1	10	250
M2	20	257
M3	30	259
M4	40	263
Sunflower oil	100	295

data analysis techniques (such as Principal Component Analysis, PCA) might be employed to distinguish adulterated oils from pure olive oils on the basis of the whole combined set of Cole-Cole parameters.

4.4.2.4 Considerations on Possible Practical Implementation

Results show that different oils exhibit different dielectric characteristics, particularly in terms of relaxation frequency. The uncertainty value associated with the evaluation of the relaxation frequency provides a self-consistent parameter for testing the performance and the suitability of dielectric spectroscopy for quality control of vegetable oils.

For this purpose, results may be collected in a database (together with the associated confidence intervals) and used as reference values for successive ‘offline’ measurements on unknown oils.

Most importantly, results on mixture of oils demonstrate that dielectric spectroscopy is sensitive to the presence of adulterants in oils. In practical applications, provided that some reference dielectric data are given for specific unadulterated oil, the possible presence of adulterants may be inferred, for example, as a deviation between reference and measured dielectric data. The major advantage of employing this method would be that the personnel in charge of control may perform the check directly in situ, without overwhelming the few available laboratories with unnecessary requests. In other words, if the dielectric spectroscopy-based analysis gives a ‘positive’ result (i.e., adulterant might be present), then further specific analyses may be required from dedicated laboratories; on the other hand, if the result is negative, then there is no need to carry out additional expensive and time-consuming analyses.

References

- [1] High precision time domain reflectometry. Agilent Application Note 1304-7, USA (2003)
- [2] Akhadov, Y.Y.: Dielectric properties of binary solutions. Pergamonj, Oxford (1980)
- [3] Buckley, F., Maryott, A.A.: Tables of dielectric dispersion data for pure liquids and dilute solutions. National Bureau of Standards Circular 589 (1958)
- [4] Castiglione, P., Shouse, P.J.: The effect of ohmic losses on time-domain reflectometry measurements of electrical conductivity. *Soil Sci. Soc. Am. J.* 67, 414–424 (2003)
- [5] Cataldo, A., Catarinucci, L., Tarricone, L., Attivissimo, F., Trotta, A.: A frequency-domain method for extending TDR performance in quality determination of fluids. *Meas. Sci. Technol.* 18(3), 675–688 (2007)
- [6] Cataldo, A., Tarricone, L., Attivissimo, F., Trotta, A.: A TDR method for real-time monitoring of liquids. *IEEE Trans. Instr. Meas.* 56(8), 1616–1625 (2007)
- [7] Cataldo, A., Vallone, M., Tarricone, L., Attivissimo, F.: An evaluation of performance limits in continuous TDR monitoring of permittivity and levels of liquid materials. *Measurement* 41(7), 719–730 (2008)

- [8] Cataldo, A., Piuze, E., Cannazza, G., De Benedetto, E.: Dielectric spectroscopy of liquids through a combined approach: evaluation of the metrological performance and feasibility study on vegetable oils. *IEEE Sens. J.* 9(10), 1226–1233 (2009)
- [9] El-Hamdy, A.H., El-Fizga, N.K.: Detection of olive oil adulteration by measuring its authenticity factor using reversed-phase high-performance liquid chromatography. *J. Chromatogr.* 708(2), 351–355 (1995)
- [10] Fenske, K., Misra, D.: Dielectric materials at microwave frequencies. *Appl. Microw. Wirel.* 12, 92–100 (2000)
- [11] Folgero, K., Friiso, T., Hilland, J., Tjomsland, T.: A broad-band and high-sensitivity dielectric spectroscopy measurement system for quality determination of low-permittivity fluids. *Meas. Sci. Technol.* 6(7), 995–1008 (1995)
- [12] Gregory, A.P., Clarke, R.N.: Tables of complex permittivity of dielectric reference liquids at frequencies up to 5 GHz. *Tech. Rep.* (2001)
- [13] Gregory, A.P., Clarke, R.N.: Traceable measurements of the static permittivity of dielectric reference liquids over the temperature range 5–50°C. *Meas. Sci. Technol.* 15(7), 1506–1516 (2005)
- [14] Guimet, F., Ferre, J., Boque, R.: Rapid detection of olive-pomace oil adulteration in extra virgin olive oils from the protected denomination of origin Siurana using excitation-emission fluorescence spectroscopy and three-way methods of analysis. *Analytica Chimica Acta* 544, 143–152 (2005)
- [15] Heimovaara, T.J.: Frequency domain modeling of TDR waveforms in order to obtain frequency dependent dielectric properties of soil samples: a theoretical approach. In: *Proceedings of the 2nd International Symposium and Workshop on Time Domain Reflectometry for Innovative Geotechnical Applications* (2001)
- [16] ISO. Guide to expression of uncertainty in measurement (1995)
- [17] Jones, S.B., Or, D.: Frequency domain analysis for extending time domain reflectometry water content measurement in highly saline soils. *Soil Sci. Soc. Am. J.* 68, 1568–1577 (2004)
- [18] Lide, D.R.: *CRC Handbook of chemistry and physics*, 89th edn. CRC Press/Taylor and Francis, Boca Raton, FL (2009)
- [19] Lizhi, H., Toyoda, K., Ihara, I.: Dielectric properties of edible oils and fatty acids as a function of frequency, temperature, moisture and composition. *J. Food. Eng.* 88(2), 151–158 (2008)
- [20] Morchio, G., DiBello, A., Mariani, C., Fedeli, E.: Detection of refined oils in virgin olive oil. *Rivista Italiana Sostanze Grasse* 66, 251–257 (1989)
- [21] Nemerich, C.P.: Time domain reflectometry liquid levels sensors. *IEEE Instr. Meas. Mag.* 4(4), 40–44 (2001)
- [22] Piuze, E., Cataldo, A., Catarinucci, L.: Enhanced reflectometry measurements of permittivities and levels in layered petrochemical liquids using an ‘in-situ’ coaxial probe. *Measurement* 42(5), 685–696 (2009)
- [23] Ramu, T.S.: On the high frequency dielectric behavior of castor oil. *IEEE Trans. Electr. Insul.* 14(3), 136–141 (1979)
- [24] Sacchi, R., Adeo, F., Polillo, L.: ¹H and ¹³C NMR of virgin olive oil. An overview. *Magn. Reson. Chem.* 35(13), 133–145 (1997)
- [25] Tay, A., Singh, R.K., Krishnan, S.S., Gore, J.P.: Authentication of olive oil adulterated with vegetable oils using fourier transform infrared spectroscopy. *Lebensmittel Wissenschaft und-Technologie* 35, 99–103 (2002)
- [26] Weerts, A.H., Huisman, J.A., Bouten, W.: Information content of time domain reflectometry waveforms. *Water Resour. Res.* 37(5), 1291–1299 (2001)

Chapter 5

Qualitative Characterization of Granular Materials and Moisture Measurements

‘There are two possible outcomes: if the result confirms the hypothesis, then you’ve made a measurement. If the result is contrary to the hypothesis, then you’ve made a discovery.’
Enrico Fermi

Abstract. This chapter focuses on broadband microwave reflectometry (BMR) applications for monitoring water content (θ) and static electrical conductivity (σ_0) of granular materials, with particular emphasis on applications for soil measurements. First, a TDR-based method for inferring θ from measurements of the apparent dielectric permittivity is presented. This approach, which relies on the individuation of so-called *calibration curves*, is discussed in detail and the related metrological assessment is provided. Successively, a more accurate method that takes into account the frequency-dependence of the dielectric permittivity of the moistened granular material (considering the permittivity of each single constituent) is presented. This application is also used as test-case for validating an innovative calibration procedure that is particularly useful when the traditional short-open-load (SOL) calibration cannot be performed. Furthermore, the adoption of antennas in place of the traditional probes is discussed (thus assessing the possibility of guaranteeing a non-invasive approach). Finally, two innovative strategies for enhancing and simplifying TDR-based measurements of static electrical conductivity σ_0 (typically used in soil science) are presented.

5.1 Introduction

Measuring water content of granular materials represents one of the major practical applications of broadband microwave reflectometry (BMR), especially for soil moisture measurements.

Indeed, reflectometric techniques have become increasingly attractive solutions for soil moisture sensing, with applications that focus on environmental monitoring purposes [60] and agricultural water management [18, 51]. In fact, mostly thanks to the versatility of the technique, a wide variety of monitoring tasks can be effectively performed through BMR [14].

Although other moisture sensing techniques could arguably provide as much measurement accuracy, their use is often hindered by practical limitations¹. Conversely, BMR holds considerable potential for practical implementation; in particular, time domain reflectometry (TDR)-based systems have become competitive with respect to other techniques, such as capacitive methods and ultrasonic sensors.

TDR-based systems can be customized according to the operating conditions, thus providing high adaptability to the specific application. Such a feature, combined with low-cost instrumentation and with an adequate measurement accuracy, has contributed to the spread of TDR in soil science, not only for moisture content evaluation but also for determining the moisture content profile [23, 29]. On such bases, relevant research effort has been dedicated to developing innovative TDR probes, enhanced measurement procedures, and sound theoretical modeling [38].

The typical TDR-based instrumental setup for in situ moisture sensing includes a portable reflectometer and a three-rod probe that can be easily inserted in the soil (or granular material in general) under investigation, thus acting as measurement cell. As mentioned in the previous chapters, despite having some shortcomings with regards to calibration, this probe configuration is widely used for TDR-based moisture content measurements.

The present chapter is structured as follows. First, the evaluation of θ through TDR-measurements of the apparent dielectric constant, ϵ_{app} , is considered. In particular, the adoption of the so-called *calibration curves*, which relate ϵ_{app} to θ , is discussed: the metrological analysis of this method demonstrates that it can ensure accurate results, provided that for each different material a specific calibration curve is individuated.

Secondly, the adoption of an enhanced approach that also takes into account the frequency-dependence of the dielectric permittivity of the investigated material is fully described. Similarly to the previously reported applications, the proposed method relies on the combination of TDR, frequency domain reflectometry (FDR), and a transmission line (TL) modeling of the measurement setup. Most importantly, this application was also used as a case-study for testing an innovative FD-based calibration technique that relies on three short-circuits applied at different probe sections. This calibration procedure is particularly important when multi-rod probes are used; in fact, in this case, traditional short-open-load (SOL) calibration is often practically unfeasible, due to the impossibility of connecting standard loads to the electrodes.

Successively, a noninvasive approach for moisture monitoring is also assessed: this method focuses on the possibility of adopting antennas as sensing elements. More specifically, the antenna is placed on the top surface of the material under test (MUT), and the shift in the resonant frequency of the antenna is associated to the corresponding moisture content of the sample.

¹ As an example, the gamma ray attenuation method is accurate but highly costly, and the presence of a radioactive source requires competent handling thus making the method unappealing for routine applications [45].

Finally, the last section of this chapter describes an enhanced TDR-based method for measuring static electrical conductivity (σ_0), especially useful for granular materials, such as soil. In particular, two innovative approaches for simplifying and ‘speeding-up’ the time-consuming preliminary procedures that have to be carried out for TDR-based estimation of σ_0 are presented. The first method relies on the combination of the TDR measurements with a transmission-line modeling (TLM) of the measurement cell; the second method simply relies on a couple of independent capacitance measurements (ICM) performed through an LCR meter.

5.2 Dielectric Models for the Estimation of Water Content

Basically, in BMR, the value of the volumetric water content, θ , is inferred from permittivity measurements². In fact, the relative permittivity of water (approximately 80) is considerably higher than the typical relative permittivity of many granular materials of interest (e.g., soil); therefore, the presence of water changes considerably the overall dielectric permittivity of the MUT.

Different methods can be adopted for deriving θ from TDR measurements. The simplest approach is based on the evaluation of θ from measurement of the apparent dielectric constant (ϵ_{app}) of the considered material [10].

A simple approach for TDR-based soil moisture monitoring relies on the use of empirical material-specific calibration curves that provide the functional relationship $\theta - \epsilon_{\text{app}}$ [10]. These curves must be determined through preliminary measurements on samples moistened at pre-fixed known moisture levels (θ_{ref}): a known volume of the considered material is moistened with fixed amounts of water and, for each level of moisture, the corresponding ϵ_{app} is retrieved from measurement of the apparent length. The points ($\theta_{\text{ref}}, \epsilon_{\text{app}}$) are fitted through a polynomial, and the obtained curve is used as reference for the successive measurements on samples of the same material, with unknown moisture levels [10]. As aforementioned, this approach is simple and adequately accurate.

Another widespread approach relies on the adoption of empirical models, which fit empirical relationship to experimental data. These models have some shortcomings (such as the limited possibility of extrapolation outside the moisture range of the original set of experiments [14]); nevertheless, they are routinely used especially for soil-like materials.

In particular, for soils, one of the most widely used relationship between ϵ_{app} and θ is the Topp’s equation [46, 63]:

$$\epsilon_{\text{app}} = 3.03 + 9.3 \theta + 146 \theta^2 - 76.7 \theta^3. \quad (5.1)$$

² Volumetric water content is expressed as $\theta = V_{\text{wat}}/V_{\text{tot}}$, where V_{wat} is the volume of water, and V_{tot} is the total volume of the mixture. The corresponding gravimetric water content can be calculated as $(\rho_{\text{wat}}/\rho_{\text{b}}) \theta$, where ρ_{wat} is the density of water, and ρ_{b} is the bulk density of the moist granular material.

Topp's equation³ is sufficiently general (in fact, it appears to be independent of soil texture and structure, salinity and temperature) [52]. However, although (5.1) has proved suitable for a wide range of homogeneous soils, it is inappropriate for clayey soils [19] and for soils with high content of organic materials [56]. In these latter cases, a third degree polynomial may still be used, but the coefficients should be extrapolated through a fitting procedure [62].

Malicki et al. suggested that the influence of the soil matrix was remarkable and, for this reason, they suggested including either dry bulk density or porosity [42]. However, the empirical functions used in current research for TDR data conversion still remain anything but universal models [14].

A more accurate $\theta - \epsilon_{\text{app}}$ relationship can be obtained through *volumetric mixing models*, which take into account the volume fraction and the dielectric constant of each single constituent that is present in the MUT. The dielectric mixing models are, therefore, particularly useful for the characterization of heterogeneous materials, such as soils with low dry bulk density, a large amount of bound water, or a relatively large permittivity of the solid phase.

In this approach, soils are usually considered as three-phased systems (made up of soil particles, water and air) or as four-phased systems (considering that water close to the soil particles behaves differently) [43].

The typical expression of a three-phased mixing model is as follows

$$\epsilon_m^\beta = \theta \epsilon_w^\beta + (1 - \phi) \epsilon_s^\beta + (\phi - \theta) \epsilon_a^\beta \quad (5.2)$$

where the subscripts m, s, a, and w stand for measured, dry soil, air, and water, respectively; ϕ is the porosity; β is a parameter that depends on the spatial structure of the mixture and its orientation with the respect to the outer electric field [49].

The four-phased systems take into account that the water that is close to the soil particles has lower mobility than free water; hence, the thin layer of water that surrounds soil particles has a lower dielectric permittivity than free water [20]. The expression of a typical four-phase mixing model is the following [68]:

$$\epsilon_m^\alpha = (1 - \phi) \epsilon_s^\alpha + (\phi - \theta) \epsilon_a^\alpha + (\theta - \theta_{\text{bw}}) \epsilon_{\text{fw}}^\alpha + \theta_{\text{bw}} \epsilon_{\text{bw}}^\alpha \quad (5.3)$$

where the subscripts m, s, a, fw, and bw stand for measured, dry soil, air, free water and bound water, respectively; α is a parameter that takes into account the geometry of the media particles with respect to the applied electromagnetic signal; and θ_{bw} is the fraction of bound water, which can be obtained from

$$\theta_{\text{bw}} = n_m \delta \rho_b S_e \quad (5.4)$$

³ Practically, for estimating water content from TDR measurements of the apparent dielectric constant, the reciprocal of (5.1) is used:

$$\theta = 4.3 \times 10^{-6} \epsilon_{\text{app}}^3 - 5.5 \times 10^{-4} \epsilon_{\text{app}}^2 + 2.92 \times 10^{-2} \epsilon_{\text{app}} - 5.3 \times 10^{-2}.$$

where n_m is the number of monolayers of water molecules of thickness δ bounded to the soil particles; S_e is the soil specific area; and $\rho_b = \rho_s(1 - \phi)$ is the soil bulk density, ρ_s being the soil dry density [19]. For complex media, such as soil, $\alpha \approx 0.5$; nevertheless, in general, α is a fitting parameter [43].

A further enhancement of these models can be achieved by taking into account the frequency-dependence of the permittivity for each of the soil constituents [68]. In fact, when dealing with complex materials or when a high percentage of water is present in the medium, the dielectric mixing model should also consider the dependence of the dielectric characteristics on frequency and the effect of σ_0 [27]. Taking into account the frequency dependence of permittivity is usually accomplished with the so-called inverse modeling, which may be developed either directly in time domain [32] or in frequency domain [9, 33].

Dielectric mixing models have proved to be suitable in many practical applications and their perspectives for further use seem to be very promising, not only for soil-like materials, but for a variety of materials (e.g., materials for construction [14]).

5.3 Evaluation of Moisture Content Directly from TDR

In this section, the estimation of moisture content from TDR-measurement of the apparent dielectric constant is addressed. In particular, the adoption of $\epsilon_{app} - \theta$ calibration curves is described in detail, and the strategies for deriving accurate and reliable curves are discussed.

As aforementioned, for a given material, the $\epsilon_{app} - \theta$ calibration curve can be assessed as follows. Samples of the considered material are moistened at prefixed values of moisture (θ_{ref}), and the corresponding apparent dielectric constant (ϵ_{app}) is measured through the TDR method. The $(\epsilon_{app}, \theta_{ref})$ points are fitted through, thus obtaining a regression curve.

In this way, in successive moisture content measurements on the same type of material, it is enough to measure ϵ_{app} , and the corresponding moisture level is simply retrieved from the calibration curve, with a certain confidence level. However, it must be pointed out that calibration curves are specific for each kind of material; hence, different curves must be derived for different materials (also, for example, for different types of soil).

As a matter of fact, different procedures are used for the extrapolation of empirical calibration curves, which, as a result, are not readily comparable. In fact, the individuation of an optimal calibration curve for each of the materials under investigation is a key point to improve the accuracy of results. Despite the deep interest surrounding TDR, neither an assessment of standard measurement procedures, nor the corresponding metrological characterization has been thoroughly investigated.

To fill this gap, the strategies for obtaining accurate calibration curves were specifically investigated. Furthermore, the metrological performance of the method was assessed through a statistical analysis on the results obtained through the two TDR instruments considered in this book (namely, the HL1500 and the TDR80E04).

Measurements were carried out on the same samples through each instrument: starting from measurements on well-referenced siliceous sand samples, the analysis was extended to agrofood granular materials (i.e., bran and corn flour). The comparison of results and related uncertainty limitation led to a consistent assessment of the method from a metrological point of view.

As already mentioned on several occasions, a metrological characterization must involve the consideration of both systematic and random errors. To minimize and to compensate for systematic error effects, a preliminary calibration of the experimental setup is mandatory (as detailed in Sect. 3.6.1). Nevertheless, further residual uncertainty contributions are mainly related to random effects. Therefore, to evaluate the final uncertainty, a statistical analysis on repeated TDR-measurements of dielectric constant was approached. To carry out the analysis, the uncertainty propagation theory and the evaluation of the expanded uncertainty associated to the t -Student distribution were considered for the estimation of the final measurement uncertainty.

Once the uncertainty, associated to the ϵ_{app} evaluation, was quantified for each measurement point, results deriving from two sets of measurements (repeated with the same instrument in different times) were unified in a single $\theta - \epsilon_{\text{app}}$ fitting curve. Subsequently, a non-linear regression method was considered in order to obtain a specific $\epsilon_{\text{app}} - \theta$ regression (calibration) curve and the related uncertainty range corresponding to the confidence level of 95%. In this way, a robust method for the evaluation of the uncertainty limitation was provided, along with some practical hints for minimizing error contributions.

5.3.1 *Details on the Experimental Procedure*

The three materials considered for the comparative analysis were sand, corn flour, and bran; their mass densities were 1.53, 0.66 and 0.67 g cm^{-3} , respectively.

Each material was placed inside a ‘large box’ (approximately $1 \text{ m} \times 1 \text{ m} \times 0.3 \text{ m}$) and was moistened at pre-established levels, according to the volumetric method reported in [47]. To achieve the pre-established moisture levels, an appropriate volume of water was weighed through an electronic balance (with an uncertainty of 0.1 g), and added to the MUT. Material and water were then mixed, so as to ensure a homogeneous moisture level: this was verified through preliminary TDR measurements of the dielectric constant in different points of the material contained in the ‘large box’. Successively, a sample was removed from the box, placed inside a cylindrical sample holder (with a diameter of 7 cm, graduated up to 2000 ml) and characterized. Preliminary measurements confirmed that boundary effects due to the used holder were negligible. As a matter of fact, this is one of the advantages of TDR method over other well-known moisture content measurement methods, such as capacitive method or ultrasonic sensor. In fact, in the last two cases, the involved low-frequency range requires the use of large boxes intended to prevent interferences caused by boundary effects.

TDR measurements were performed through a 15 cm-long commercial three-rod probe (CS630, Campbell Scientific).

Before proceeding with the detailed discussion on the proposed experimental and metrological approaches, let us briefly summarize the key-points of the procedure. After a specific probe calibration (as reported in subsection 3.6.1), for each of the pre-established moisture levels (θ_{ref}) at which the samples were moistened, the corresponding ϵ_{app} value was evaluated. This way, the functional relationships between the apparent dielectric constant and the corresponding moisture level were identified through an appropriate fitting of the data. The overall uncertainty of ϵ_{app} was evaluated so as to draw a preliminary comparison between the different performances of the used TDR instruments and to understand to which extent results depend either on the instrument or on other experimental conditions.

Successively, the fitted data were used to extrapolate specific calibration curves, for each considered material and for each instrument. Simultaneously, an evaluation of the overall uncertainty in the estimation of θ from the calibration curves was done through the non-linear regression method. This was done to provide a comprehensive panorama of the measurement system as a whole and to validate a general method which, in turn, can be applied also for other types of materials.

As reported in [3] and according to the calibration procedure described in Sect. 3.6.1, a ten-measurement set was preliminarily carried out with the three-rod probe-footnotemark immersed first in air and then in demineralized water.

5.3.2 *Uncertainty Evaluation for Apparent Dielectric Permittivity Measurement and Individuation of the Calibration Curves*

The evaluation of the apparent dielectric constant from TDR measurements relies on (3.5), which is reported here for convenience:

$$\epsilon_{\text{app}} = \left(\frac{L_{\text{app}}}{L} \right)^2 \quad (5.5)$$

where L_{app} is the apparent probe length in the MUT and L is the length of the probe in air. To take into account the uncertainty sources, a ten-measurement set of the apparent length L_{app} was acquired for each sample. For each set of measurements, both the mean apparent length $\overline{L_{\text{app}}}$ and the standard deviation $\sigma_{L_{\text{app}}}$ were calculated⁴, then the expanded uncertainty $U_{L_{\text{app}}}$ was evaluated through the t -Student distribution, according to the relation:

$$U_{L_{\text{app}}} = 2.26\sigma_{L_{\text{app}}} \quad (5.6)$$

³ A coaxial geometry for the probe would guarantee a reliable matched transmission line. Nevertheless, three-rod probes are definitely more practically usable when investigating granular materials, thanks to the easier insertion in the MUT.

⁴ $\sigma_{L_{\text{app}}}$ is the standard deviation corresponding to the Gaussian distribution, which was verified through the χ -square test.

where 2.26 is the t -score associated with a confidence level of 95% and nine degrees of freedom. Once $\overline{L}_{\text{app}}$ and $U_{L_{\text{app}}}$ were both known for each of the ten-measurement sets, referring to U_L as the expanded uncertainty of the probe electrical length in air, the measurement uncertainty was evaluated using the uncertainty propagation theory [34], according to the following equation:

$$U_{\varepsilon_i} = \sqrt{\left[\left(\frac{\partial \varepsilon_i}{\partial L_{\text{app}(i)}} U_{L_{\text{app}(i)}} \right)^2 + \left(\frac{\partial \varepsilon_i}{\partial L} U_L \right)^2 \right]} =$$

$$= \sqrt{\left[\left(2 \frac{\overline{L}_{\text{app}(i)}}{L^2} U_{L_{\text{app}(i)}} \right)^2 + \left(2 \frac{\overline{L}_{\text{app}(i)}}{L^3} U_L \right)^2 \right]} \quad (5.7)$$

In the above equation, U_{ε_i} is the propagated uncertainty associated to the i -th measurement of the ε_{app} value. Finally, data with corresponding uncertainty bars were fitted in a $\theta - \varepsilon_{\text{app}}$ curve.

To determine the $\varepsilon_{\text{app}} - \theta$ relationship, the experimental data were fitted, thus obtaining the optimal calibration curve. As also reported in many related papers, third order polynomial curves prove to be a good fitting of experimental data:

$$\theta = B_0 + B_1 \varepsilon_{\text{app}} + B_2 \varepsilon_{\text{app}}^2 + B_3 \varepsilon_{\text{app}}^3 \quad (5.8)$$

where B_0 , B_1 , B_2 and B_3 are the regression coefficients. This way, (5.8) represents the calibration curve: in correspondence of each measured dielectric constant value ε_{app} , the curve provides the corresponding θ .

To characterize the extrapolated value of θ from a metrological point of view, the associated uncertainty was evaluated through the non-linear regression theory [34]. Hence, the variance analysis for the single values expected from the previous equation was conducted according to

$$\text{var}[\theta] = \sigma^2 \left(1 + \frac{1}{n} + \sum_i \left(\frac{\partial \theta}{\partial B_i} \right)^2 \text{var}[B_i] + 2 \sum_{ij} \left(\frac{\partial \theta}{\partial B_i} \frac{\partial \theta}{\partial B_j} \right) \text{cov}[B_i, B_j] \right) \quad (5.9)$$

where $\text{var}[\theta]$ is the variance of the moisture level; σ^2 is the variance between experimental and fitted data; n is the number of experimental points; $i, j = 0, 1, 2, 3$; and $\text{cov}[B_i, B_j]$ is the covariance between B_i and B_j parameters.

For a confidence level of 95%, the equations associated to the lower and upper confidence limits for the regression curve are given by the following equations: alpha

$$L_{\text{low}} = (B_0 + B_1 \varepsilon_{\text{app}} + B_2 \varepsilon_{\text{app}}^2 + B_3 \varepsilon_{\text{app}}^3) - t_{n-4, 1-\frac{\alpha}{2}} \sqrt{\text{var}[\theta]} \quad (5.10)$$

$$L_{up} = (B_0 + B_1 \varepsilon_{app} + B_2 \varepsilon_{app}^2 + B_3 \varepsilon_{app}^3) + t_{n-4, 1-\frac{\alpha}{2}} \sqrt{\text{var}[\theta]} \quad (5.11)$$

where α is the significance level (5%) [34].

5.3.3 Measurement Results and Instrumental Performance Comparison

Preliminarily, to validate the practical implementation of the proposed methodology, repeatability tests were carried out on the considered material samples (sand, bran, and corn flour), with both the HL1500 and the TDR80E04. For each instrument, two series of measurements were performed, in different times, on each MUT: as expected, both for the HL1500 and for the TDR80E04, a good agreement between the first and the second series of measurements was observed.

The repeated measurements were grouped to extrapolate specific fitting curves for each instrument. The resulting fitting curves were unified in a single ‘global’ curve for each material and for each instrument (Fig. 5.1), and the corresponding uncertainty values were calculated for each measured ε_{app} . Particularly, to verify the adequacy of the normal function distribution in describing the uncertainty distribution, the t -Student distribution was considered for the whole series of measurement data: the hypothesis was confirmed assuming a confidence level of 95% [34]. This way, in Fig. 5.1, to each measured ε_{app} value the corresponding absolute uncertainty bar ($U_{\varepsilon_{app}}$) is associated, exhibiting a maximum percentage relative standard uncertainty lower than 10% for the HL1500, and lower than 5% for the TDR80E04. As expected, the uncertainty affecting ε_{app} measured through the HL1500 is higher than the uncertainty affecting the ε_{app} obtained through the TDR80E04. The metrological characterization of the proposed method involves the analysis of regression curves on each material sample and for both HL1500 and TDR80E04. The associated confidence intervals are reported in Figs 5.2–5.4, in terms of lower and upper limits of global calibration curves (L_{low} and L_{up}), as calculated from (5.10) and (5.11).

The graphs show the good agreement between measurements conducted through the HL1500 and through the TDR80E04; the corresponding value of the confidence band allows deducing the final uncertainty in moisture level evaluation. Results related with regression curves for lower and upper limits of confidence bands are summarized in Table 5.1. It is worth pointing out that even though in some cases

Table 5.1 Absolute uncertainty range of regression curve for each considered material, associated to a confidence level of 95%, calculated for the two TDR instruments

	HL1500 $L_{up}(L_{low})$	TDR80E04 $L_{up}(L_{low})$
sand	0.056	0.024
bran	0.020	0.037
corn flour	0.031	0.022

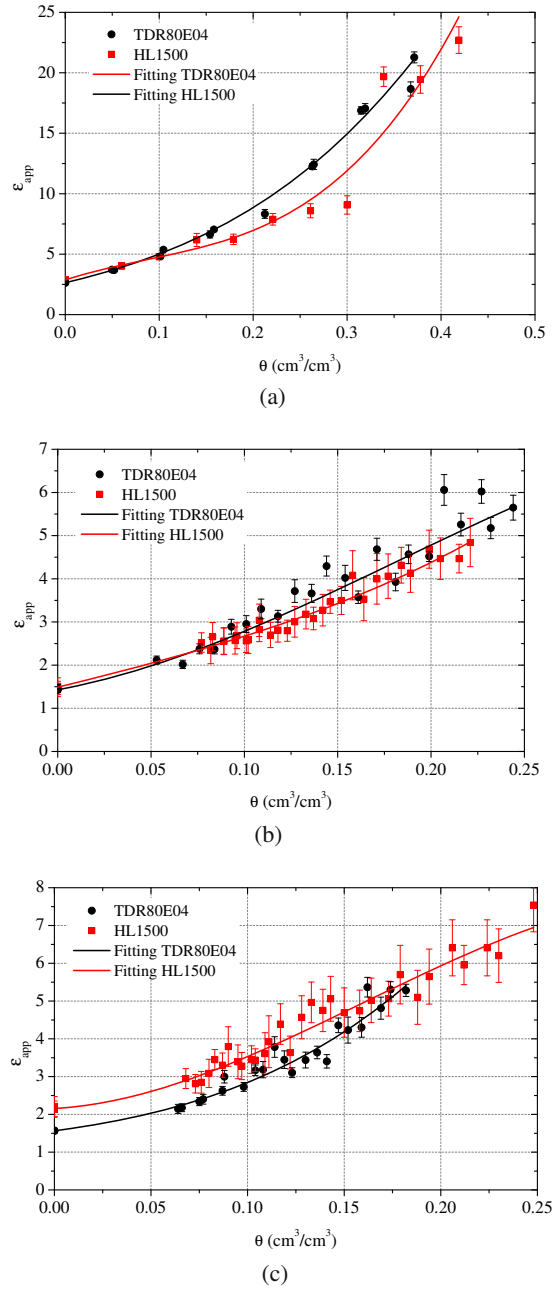


Fig. 5.1 Comparison between global fitting curves obtained using HL1500 and TDR80E04. **a** for sand. **b** bran. **c** corn flour. Absolute uncertainty bars are also reported

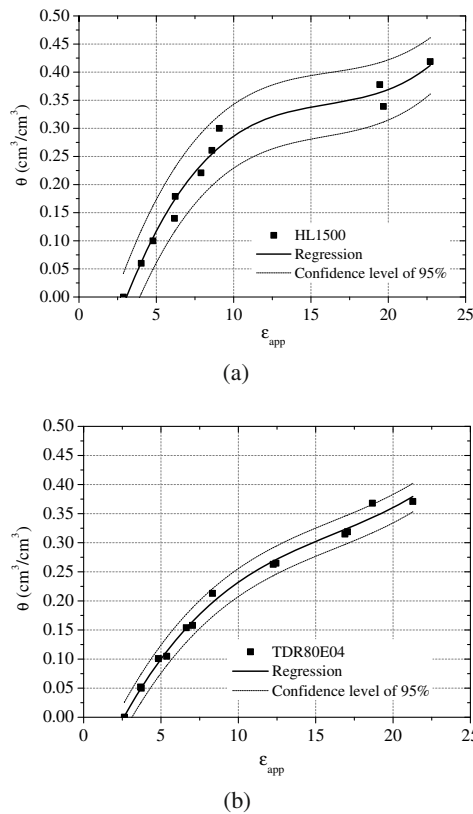


Fig. 5.2 Global regression curve for sand. **a** obtained using HL1500. **b** obtained using TDR80E04. Related confidence limits, associated to the 95% of probability occurrence, are also reported

it appears that the distribution of the HL1500 measurement points is narrower than the TDR80E04 measurement points distribution around their respective extrapolating polynomial, this is merely due to the fact that upper and lower limits mainly indicate how well the regression curve fits the experimental points, and should not be attributed to a better performance of the HL1500.

5.3.3.1 Consideration on Practical Implementation

As expected, TDR80E04 exhibits a better performance in terms of accuracy than its less-expensive portable counterpart, the HL1500. Nevertheless, the adoption of the

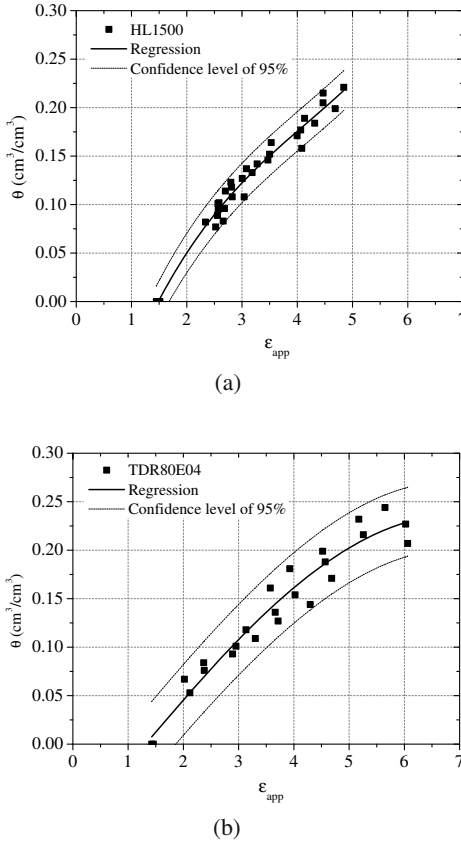


Fig. 5.3 Global regression curve for bran. **a** obtained using HL1500. **b** obtained using the TDR80E04. Related confidence limits, associated to the 95% of probability occurrence, are also reported

low-cost portable HL1500, in conjunction with the proposed measurement procedure, guarantees adequate performance, thus allowing a reliable monitoring of the water content. These results are achieved thanks to the strategies described in Sect. 3.6.1, such as a preliminary calibration procedure making the approach extremely robust, as well as techniques of waveform interpretation and compensation of residual error contributions.

As already demonstrated in the cases of liquid materials, this is particularly important in view of possible industrial implementation, which not only does require accuracy and reliability, but also low cost and portability.

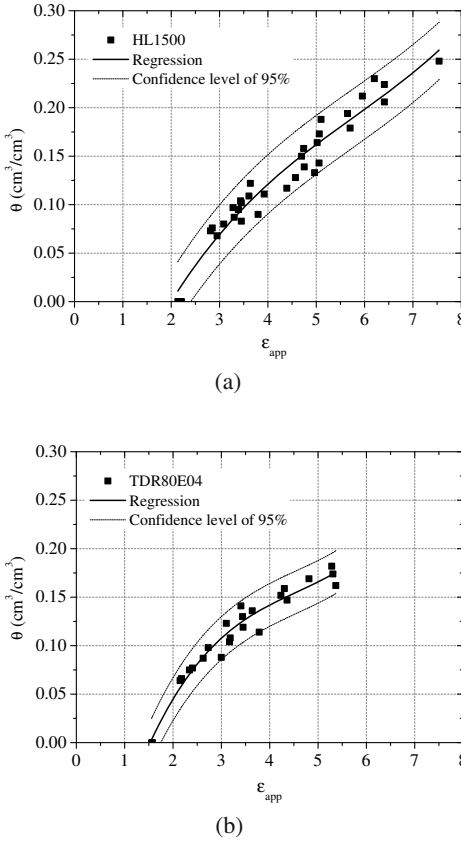


Fig. 5.4 Global regression curve for corn flour. **a** obtained using the HL1500. **b** obtained using the TDR80E04. Related confidence limits, associated to the 95% of probability occurrence, are also reported

5.4 Moisture Content Measurements through TD/FD Combined Approach and TL Modeling

5.4.1 Moisture Content Measurements through Dielectric Mixing Model

As mentioned in Sect. 5.2, a further enhancement of the accuracy in the estimation of moisture content can be achieved by considering the dielectric permittivity of each of the soil constituents (i.e., air, water, and soil particles) and their dependence on frequency.

In the proposed method, the three-rod probe (i.e., the 15 cm-long Campbell Scientific CS630 [3], connected to the HL1500) inserted in the moistened soil (considered as a dispersive material) is modeled as a transmission-line. In particular, considering a TEM mode propagating along the open-terminated probe, the frequency-dependent reflection coefficient $S_{11,MOD}(f)$ at the beginning of the rods (section A in Fig. 5.5)) can be simply written as [50]

$$S_{11,MOD}(f) = e^{-2ik^*(f)l} \quad (5.12)$$

where l is the rod length, $i^2 = -1$, and $k^*(f) = 2\pi f(\mu_0\epsilon_0\epsilon_{sc}^*(f))^{1/2}$ is the complex propagation constant, associated to μ_0 and ϵ_0 , and to the complex relative permittivity of the soil $\epsilon_{sc}^*(f)$.

The key point for the implementation of Eq. (5.12) is the choice of an appropriate mixing model for $\epsilon_{sc}^*(f)$, thus accurately representing the dielectric characteristics of the soil-medium.

As well known, the frequency-dependent dielectric permittivity of a homogeneous material can be suitably described by the Debye equation [26]. Conversely, the heterogeneity of soil dictates the use of more complex models that could provide a more truthful representation of the dielectric behavior. Various models have been used to describe mixtures; nevertheless, no complete model is available that can describe the dielectric properties of soil [31]. A detailed review of the advances in soil mixing models can be found in [55].

The experiments reported in this section focused on sandy soils, for which the effect of bound water is negligible; therefore, a three-phased dielectric mixing model is enough to adequately describe the dielectric properties [68]. More specifically, for sand moistened at a volumetric water content, the corresponding complex relative permittivity $\epsilon_{sc}^*(f)$ can be suitably described through the following equation [68]:

$$\epsilon_{sc}^*(f) = [(1 - \phi)\epsilon_{sp}^\alpha + \theta(\epsilon_{wc}^*(f))^\alpha + (\phi - \theta)\epsilon_a^\alpha]^{1/\alpha} - i\frac{\sigma_0}{2\pi f\epsilon_0} \quad (5.13)$$

where ϕ is the porosity of sand; ϵ_{sp} is the relative permittivity of the sand particles (assumed constant with frequency); $\epsilon_{wc}^*(f)$ is the frequency-dependent complex relative permittivity of water; ϵ_a is the relative permittivity of air (assumed equal to 1); σ_0 is the static electrical conductivity of the moistened sand; and α is a fitting parameter that takes into account the geometry of the sand particles.

5.4.2 Triple-Short Calibration Procedure

The adoption of dielectric mixing models for moisture content estimation has several major advantages; nevertheless, its measurement accuracy is strongly related to the adoption of a frequency-domain calibration (FDC) procedure, which typically involves the use of coaxial electrical standards, such as short-open-load (SOL). Generally, for performing a calibration, the electrical standards should be connected to the section that corresponds to the beginning of the material under test (i.e., the

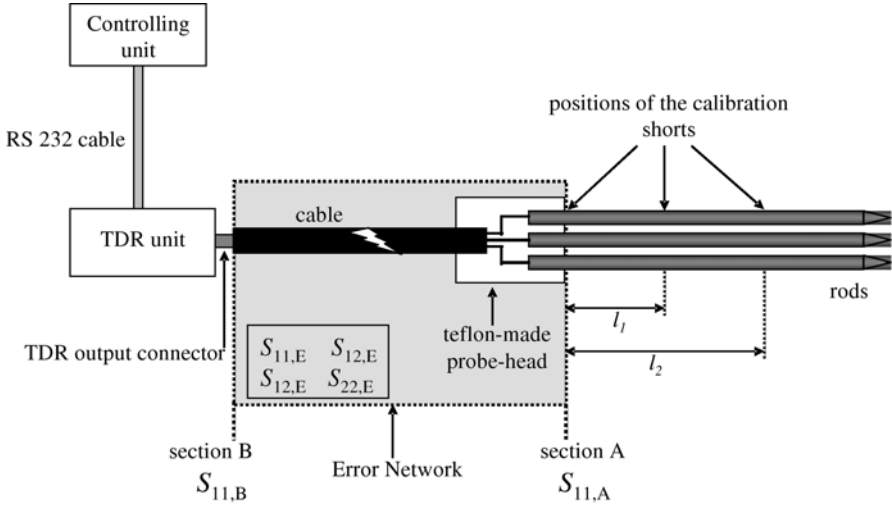


Fig. 5.5 Schematic representation of the experimental setup. The rectangle highlights all the effects that are included in the error network (not to scale) [48]

beginning of the probe rods, section A in Fig. 5.5). Unfortunately, the structure of commercial three-rod probes does not allow such a calibration because the open and matched loads insertion would require detaching the rods from the probe head and the exact knowledge of the value of the matching impedance. As a matter of fact, SOL standards for three-rod probes are not commercially available, and even in-house solutions for calibration fixtures mimicking *open* and *load* conditions are difficult to be reproduced.

To overcome such a limitation, an innovative calibration procedure that does not require either the *open* or the *load* conditions was specifically developed. In fact, the proposed calibration method relies only on the short-circuit conditions obtained at three different sections along the probe (triple short calibration - TSC) [48].

The TSC procedure was tested and validated through preliminary measurements on well-referenced materials. Successively, it was applied to sandy soil brought at different levels of moisture. Results show that the combination of a frequency-dependent dielectric mixing modeling, of a minimization routine, and of the proposed TSC procedure is the key strategy for obtaining accurate TDR moisture content evaluations while reducing the complexity of the calibration phase. Another possible alternative solution for allowing traditional SOL calibration could be to design and realize a custom-made probe, similarly to the case presented in Sect. 4.3. However, the TSC procedure presented herein can be readily applied to commercially available multi-rod probes.

As aforementioned, to effectively enhance the accuracy in the estimation of soil moisture content, the reflection coefficient $S_{11,MEAS}(f)$ at section A of the probe (see Fig. 5.5) must be evaluated. In fact, it is worth mentioning that, similarly to the previously-discussed cases, TDR intrinsically measures the reflection

coefficient along the whole transmission chain (i.e., starting from the instrument output connector, up to the probe end). As a direct consequence, the resulting response is inevitably affected by all the parasitics and losses introduced by the cable, connections, section transitions, and probe-head portion. A calibration procedure allows reducing the influence of these parasitics.

As well known, the aim of the calibration procedure is to assess the three scattering parameters that characterize the ‘error network’, depicted in Fig. 5.5, which models all systematic errors effects between the instrument output connector and the section corresponding to the beginning of the MUT [1]. Three short circuits were applied at different sections along the probe; in fact, these loads can be easily applied at whichever distance from the probe head.

For this specific configuration, the first short was directly applied to section A, whereas the other two shorts were applied at distances l_1 and l_2 from the probe head, respectively. When a short circuit condition is realized at a generic distance l from the probe head, the reflection coefficient at section A ($S_{11_{sc,A}}$) can be expressed as follows:

$$S_{11_{sc,A}} = -e^{-2i\beta l} \quad (5.14)$$

where $\beta = 2\pi f(\mu_0\epsilon_0)^{1/2}$ is the propagation constant in air. The ‘error network’, which is characterized by its scattering parameters $S_{11,E}$; $S_{12,E}$; and $S_{22,E}$, transforms such reflection coefficient at section A in a new one, namely $S_{11_{sc,B}}$, measured at the TDR connector (section B):

$$S_{11_{sc,B}} = S_{11,E} - \frac{S_{12,E}^2 e^{-2i\beta l}}{1 + S_{22,E} e^{-2i\beta l}} \quad (5.15)$$

Therefore, if the values of $S_{11_{sc,B}}$ corresponding to three different positions of the short circuit (namely, $l = 0$, $l = l_1$, and $l = l_2$) are measured, a system of three equations in three unknowns is obtained, from which the three error parameters $S_{11,E}$; $S_{12,E}$; and $S_{22,E}$ can be retrieved. In particular, after appropriate simplifications within the MathematicaTM software, the following expressions are obtained for the error network parameters:

$$S_{11E} = \frac{-iS_{11_{sc0,B}}(S_{11_{sc1,B}} - S_{11_{sc2,B}}) - S_{11_{sc2,B}}(S_{11_{sc0,B}} - S_{11_{sc1,B}})\cot(\beta l_1)}{A} + \frac{S_{11_{sc1,B}}(S_{11_{sc0,B}} - S_{11_{sc2,B}})\cot(\beta l_2)}{A} \quad (5.16)$$

$$S_{12E}^2 = \frac{2i(S_{11_{sc0,B}} - S_{11_{sc1,B}})(S_{11_{sc0,B}} - S_{11_{sc2,B}})}{A^2} \times \frac{(S_{11_{sc1,B}} - S_{11_{sc2,B}})\csc(\beta l_1)\csc(\beta l_2)\sin(\beta(l_1 - l_2))}{A^2} \quad (5.17)$$

$$S_{22E} = \frac{-i(S_{11_{sc1,B}} - S_{11_{sc2,B}}) + (S_{11_{sc0,B}} - S_{11_{sc1,B}}) \cot(\beta l_1)}{A} + \frac{(S_{11_{sc0,B}} - S_{11_{sc2,B}}) \cot(\beta l_2)}{A} \quad (5.18)$$

where A is given by

$$A = -i(S_{11_{sc1,B}} - S_{11_{sc2,B}}) - (S_{11_{sc0,B}} - S_{11_{sc1,B}}) \cot(\beta l_1) + (S_{11_{sc0,B}} - S_{11_{sc2,B}}) \cot(\beta l_2)$$

$S_{11_{sc0,B}}$, $S_{11_{sc1,B}}$, and $S_{11_{sc2,B}}$ are the reflection coefficients measured at section B for the short circuits located at $l = 0$, $l = l_1$, and $l = l_2$, respectively.

Once the error network is characterized by means of the TSC procedure, the measurements performed at section B ($S_{11,B}$) can be corrected so as to obtain the corresponding reflection coefficient at the beginning of the rods ($S_{11,A}$):

$$S_{11,A} = \frac{S_{11,B} - S_{11,E}}{S_{11,B}S_{22,E} + S_{12,E}^2 - S_{11,E}S_{22,E}}. \quad (5.19)$$

A crucial point of the TSC procedure is the optimal choice of the distances l_1 and l_2 .

The impedance along a line presents a periodic behavior, with a period equal to half wavelength. This means that at the frequency for which l_2 is equal to half wavelength, the distal short appears again as a short at section A, causing a singularity in the error network parameters (as a matter of fact, only two of the three loads remain independent). On the other hand, choosing very short distances for the three shorts would compromise measurement accuracy at low frequencies, because the phase differences between the shorts tend to vanish.

Since the TDR unit used for these measurements has an operating bandwidth of approximately 1.5 GHz, a distance l_2 equal to 10 cm was chosen, yielding a singularity exactly at the upper bound of the bandwidth. For symmetry, l_1 was set equal to 5 cm.

5.4.2.1 Evaluation of Moisture Content

Soil moisture content was evaluated through the minimization of the squared magnitude of the difference between the $S_{11,MOD}(f)$ modeled through (5.12) and (5.13), and the $S_{11,MEAS}(f)$ that was derived from TDR measurements and referred to the corresponding calibration section (i.e., section A in Fig. 5.5). The measurement cell is modeled as the portion of a transmission line, and the soil is characterized by means of an appropriate dielectric model. Subsequently, the reflection scattering parameter of the implemented model, $S_{11,MOD}(f)$, is evaluated as a function of the unknown value θ . Finally, through the aforementioned minimization routine

(in which $S_{11,MEAS}(f)$ is derived from the TD/FD combined approach), it is possible to retrieve the unknown value of moisture content. To carry out this minimization procedure, all the parameters in (5.13), with the exception of θ , should be known.

For this purpose, the sand porosity was preliminarily assessed through the so-called water saturation method⁵.

As for the complex permittivity of water, its frequency-dependent behavior was obtained through a Debye model; in turn, the dependence of the Debye parameters on temperature was taken into account through empirical expressions reported in the literature [35]. Static electrical conductivity was measured through the well-known Castiglione-Shouse method [8], which allows the estimation of σ_0 from TDR measurements (in particular, the same probe was used).

Finally, the two remaining unknowns (namely, ϵ_{sp} and α) were estimated as follows: two measurements were performed, on dry sand ($\theta = 0$) and on sand moistened at a known θ value (namely, 25%); successively, ϵ_{sp} and α were extracted through a preliminary minimization routine (which was performed over ϵ_{sp} and α , and considering θ as a known value). On a side note, it is worth mentioning that the value of ϵ_{sp} might also be directly measured through the TDR technique using, for example, the procedure reported in [54].

5.4.2.2 Preliminary Validation of the TSC Procedure

The proposed TSC procedure was preliminarily tested on bi-distilled water and ethanol. To this end, the three TDR measurements on the short circuits were used to derive the error network parameters, according to (5.16)-(5.18). Successively, the error correction procedure, based on (5.19), was applied to $S_{11,MEAS}(f)$ measured at section B for the two liquids. Fig. 5.6(a) shows, for the case of bi-distilled water, a comparison among the absolute values of the $S_{11}(f)$ at section B, obtained through the TD/FD combined approach [11]; the corrected S_{11} at section A; and the theoretical S_{11} behavior obtained through TL modeling of the rods immersed in water (characterized through its Debye model). Similarly, Fig. 5.6(b) shows the comparison for the case of ethanol.

In the TL modeling, for the probe rods, an effective length of 152 mm (including the fringing effect at the rods distal end) was always considered.

The analyzed frequency band was limited to 500 MHz, because the three-rod probe configuration and dimensions do not allow accurate and repeatable measurements above such frequency. The figures clearly show the effect of the adopted calibration and of the error correction procedures, yielding corrected reflection coefficients curves that are in close agreement with the ones expected from theory.

⁵ A known volume of water (v_w) was added to a known volume of dry sand (v_s); the volume of the sand included the pores. After the sand was saturated with water, the total volume of the mixture (v_{mix}) was measured. Eventually, the volume fraction of the pores was obtained as $(v_w + v_s) - v_{mix}$, from which the sand porosity could be easily derived.

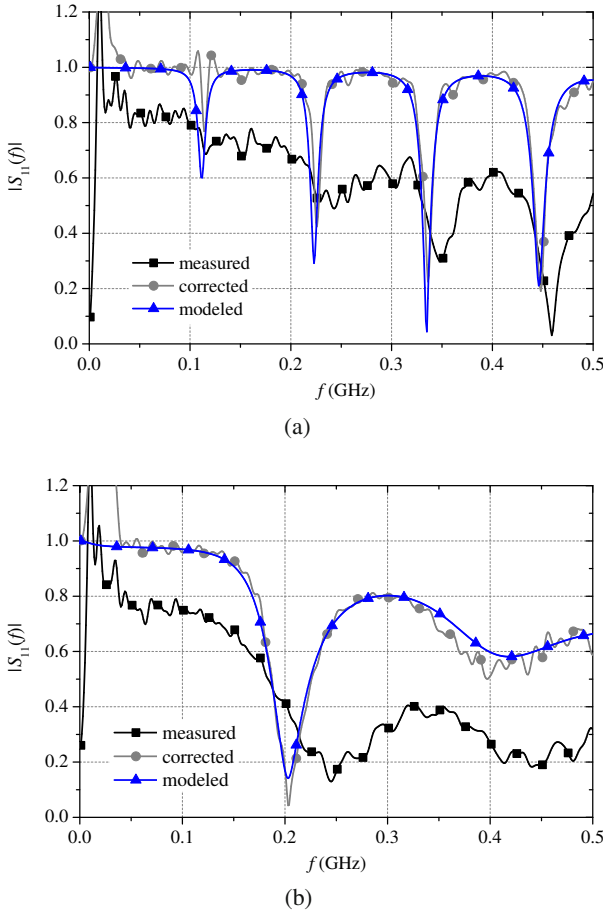


Fig. 5.6 Results for the preliminary test of the TSC procedure: comparison of the magnitudes of the measured, of the corrected, and of the modeled S_{11} . **a** for bi-distilled water at 25.6°C. **b** for ethanol at 25.4°C [48]

5.4.2.3 TSC Application Test-Case: Soil Moisture Estimation

Construction sand was used as test material; the sample was placed inside a cylindrical holder (with a diameter of 7.8 cm and a height of 25 cm). Preliminary measurements confirmed that boundary effects due to the used holder were negligible.

To verify the suitability of the proposed method for the estimation of θ , the sand sample was moistened at five prefixed water contents levels (θ), corresponding to 5%, 10%, 15%, 20%, and 25%. The probe was inserted in the sand and was not removed until all the experiments were carried out. Moistening was performed by adding the fixed amount of water from the top-surface of the sample; when the distribution of water appeared homogeneous (which took approximately 30 hours for

each moisture level) the TDR measurements could be carried out. To avoid variations in moisture profile along the probe, due to gravity effects, the cylindrical holder was kept horizontal during all measurements. The sample temperature was kept at $27 \pm 1^\circ\text{C}$ during all the experimental session.

For each moisture level, two TDR waveforms were acquired: one with a very long acquisition window and the other with a shorter one. The former was used for the evaluation of σ_0 through the Castiglione-Shouse method [8]; whereas the latter was used both for the estimation of the dielectric constant through the traditional TDR method [10] and for obtaining $S_{11,\text{MEAS}}(f)$ to be used in the subsequent minimization procedure. For the sake of example, Fig. 5.7 shows a typical TDR waveform (corresponding to the dry sand sample), acquired with a short acquisition window. Finally, to perform the aforementioned TSC, the TDR waveforms corresponding to three short-circuit conditions obtained at different sections of the probe were acquired. The short-circuit conditions were achieved by short-circuiting the probe rods (at the desired section) by means of a perforated copper slab with a ‘guillotine configuration’ (see Fig. 5.8). All the TDR waveforms measured at section B were preliminarily FFT-processed and corrected by means of (5.19), thus obtaining the $S_{11,\text{MEAS}}(f)$ at section A to be used in the minimization procedure.

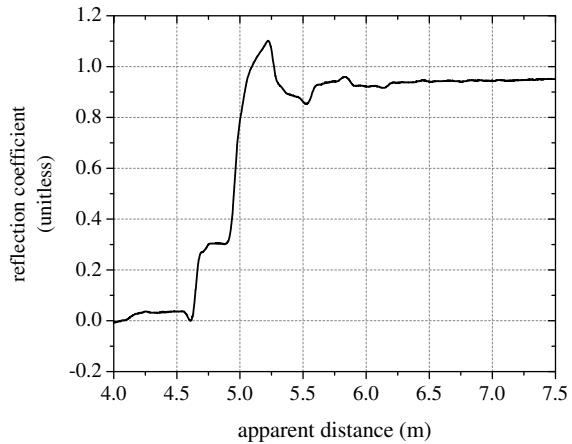


Fig. 5.7 Typical TDR waveform (for the dry sand sample) acquired with a short acquisition window [48]

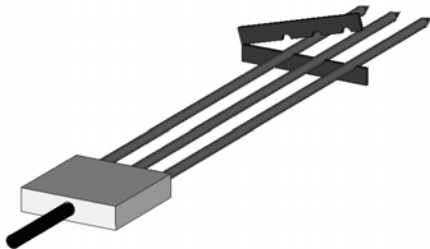


Fig. 5.8 Schematization of the perforated slab used for obtaining the short-circuit condition [48]

As aforementioned, the minimization procedure was initially applied to measurements on dry sand and on sand with $\theta = 25\%$, in order to estimate the values of ϵ_{sp} and α . The optimized values for such parameters, retrieved through a simplex optimization procedure, are $\epsilon_{sp} = 4.70$ and $\alpha = 0.624$. Moreover, sand porosity ϕ was measured to be 0.39.

Successively, the minimization procedure was applied to $S_{11,MEAS}(f)$ for each moistened soil sample, in order to retrieve the optimized value for the volumetric water content θ .

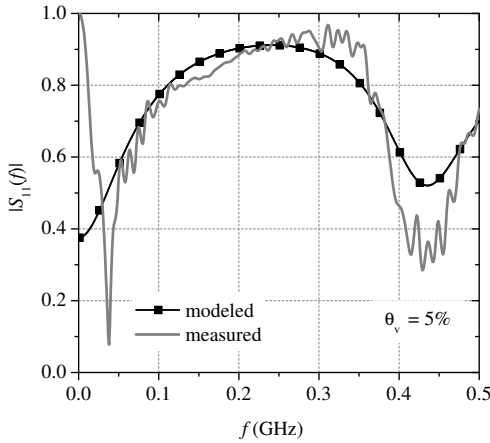
For each moistening step, the obtained results are summarized in Table 5.2, which reports the nominal moisture level, the moisture level estimated through the minimization procedure, and the evaluated static conductivity. Results in Table 5.2 show an excellent agreement between estimated and nominal moisture levels for high water content, with a slightly decreasing performance for low-humidity conditions. This last effect is attributable to the fact that low-humidity samples exhibit low permittivity values and would require longer probes to provide more electrical length for the TDR signal.

Table 5.2 Reference volumetric water content (θ_{ref}) and estimated volumetric water content (θ_{est}), for five moisture levels. The corresponding values of the static electrical conductivity (σ_0), evaluated through the Castiglione-Shouse method, are also reported [48]

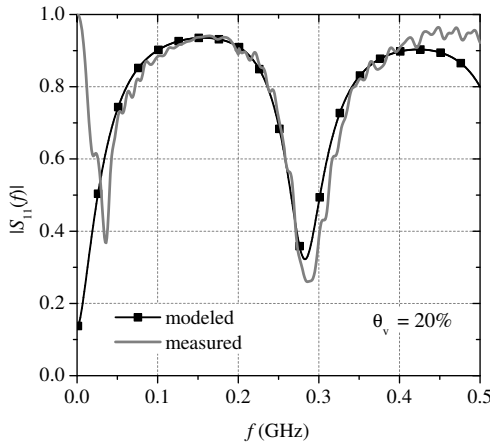
θ_{ref} (%)	θ_{est} (%)	σ_0 (mS m ⁻¹)
5.0	5.9	7.920
10.0	11.4	9.914
15.0	14.7	12.199
20.0	19.8	13.272
25.0	25.0	19.214

Fig. 5.9 shows a comparison between $|S_{11,MEAS}(f)|$ and $|S_{11,MOD}(f)|$, after optimization, for $\theta = 5\%$ [Fig. 5.9(a)] and for $\theta = 20\%$ [Fig. 5.9(b)]. A good agreement can be observed between the experimental and analytical curves over all the considered frequency range, with the exception of the low frequency band. Indeed, a fine tuning of the acquisition window length should suitably lead to a balance of some contrasting effects, thus preserving the accuracy of the frequency-domain data. In particular, as will be detailed in the following chapter, the optimal time windowing should balance 1) the frequency resolution; 2) the signal to noise ratio (SNR); and 3) the inclusion of a sufficient number of TDR multiple reflections so as to obtain a complete spectral picture.

Fig. 5.9 also clearly shows the higher noise in the experimental curves and the consequent worsening in the model fitting for lower humidity levels. Finally,



(a)



(b)

Fig. 5.9 Results for the described moisture evaluation method: comparison between $|S_{11,MEAS}(f)|$ and $|S_{11,MOD}(f)|$, after optimization, for the sand sample. **a** at $\theta = 5\%$. **b** at $\theta = 20\%$ [48]

Fig. 5.10 shows the permittivity spectra of the sand sample, for $\theta = 20\%$, as obtained from (5.13) after optimization. It can be seen that the imaginary part of the permittivity of the soil is not negligible in the low-frequency range and that it shows a markedly dispersive behavior.

On a side note, it is worth noting that for $\theta = 20\%$, the apparent dielectric constant (ϵ_{app}) directly evaluated from the time-domain TDR traces is 11.83. This result is due to the fact that ϵ_{app} incorporates the effect of both the real and the imaginary parts of the dielectric permittivity (ϵ_{sc}^*) in the frequency range of the test signal [39].

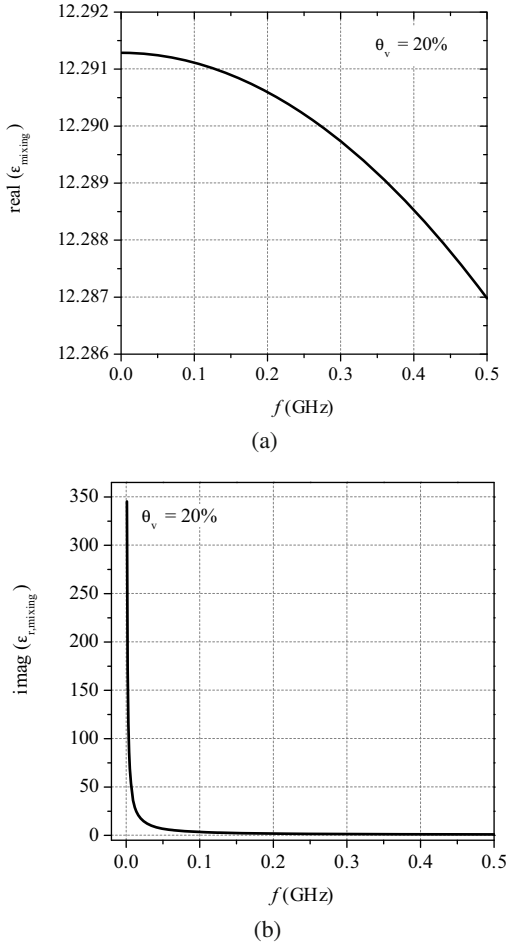


Fig. 5.10 Permittivity spectra, as obtained from the adopted dielectric mixing model after optimization, for the sand sample moistened at $\theta = 20\%$. **a** real part of permittivity. **b** imaginary part of permittivity [48]

5.5 Enhancements of TDR-Based Static Electrical Conductivity Measurement

Static electrical conductivity (σ_0) is a fundamental physical parameter that is extremely useful in many research and industrial areas. Two major fields in which the estimation of σ_0 is particularly important are soil science and the agro-food industry: in the former, σ_0 can be associated with several different properties such as salinity, solute transport, etc.; whereas in the latter, σ_0 may be used as an indicator of the quality status of the products.

However, the evaluation of the σ_0 of soils has proved to be a difficult task; and this is the case of granular materials in general [15]. The well-established four-point technique for electrical conductivity/resistivity measurements⁶ imposes stringent operating requirements that are not always easily achievable, especially when dealing with granular moistened materials⁷.

For this reason, there has been a growing interest toward alternative measurement techniques, such as the Sigma probe [25], the electromagnetic induction method [30], and TDR [46].

Indeed, the most attractive trait of the TDR-based approach is that the test-signal is a broadband electromagnetic signal: the value of the static electrical conductivity is extrapolated through appropriate analysis and processing of the TDR waveforms; hence, the DC-related limitations are overcome. It goes without saying that the additional advantages of using TDR relate to the possibility to simultaneously estimate several other material properties, such as dielectric permittivity [16], water content [17], salinity [53], and solute transport [36]. Finally, the wide availability of portable low-cost TDR instruments and the capability of obtaining accurate real-time, in situ monitoring make the TDR technique definitely attractive also in view of practical applications.

However, the accuracy of traditional TDR-based electrical conductivity measurements is strongly influenced by the preliminary calibration technique. In this regard, two innovative approaches for speeding up the preliminary calibration procedures required for the TDR-based measurement of σ_0 were assessed. The first method relies on the combination of the TDR measurement with a transmission-line modeling (TLM); the second method simply relies on a couple of independent capacitance measurements (ICM) performed through an LCR meter. The metrological performance of this last method is compared with that of the traditional one, thus validating its applicability. Experimental results and related uncertainty analysis on various samples demonstrate that the proposed method is suitable for a simpler and accurate estimation of the σ_0 , also when dealing with moistened soils.

5.5.1 Traditional TDR-Based Static Electrical Conductivity Measurement

Traditionally, TDR-based measurements of σ_0 of granular materials are carried out employing multi-rod probes.

⁶ In the four-point technique, a current is forced through the two amperometric electrodes, placed at the ends of the sample, and the corresponding voltage value is measured at the two voltmetric electrodes.

⁷ For example, good and electrically-stable contacts between the four electrodes and the sample are essential [67]. Nevertheless, unless very expensive materials are used for the electrodes (e.g., titanium, gold), electrochemical processes due, for example, to the presence of water in the soil, occur at the electrodes interfaces, thus rapidly degrading the electric contacts. Indeed, this kind of measurements should be performed in static conditions, therefore, as well known, the electrode polarization effect is an unavoidable limit that practically impairs the measurement feasibility.

TDR-based conductivity measurements rely on the Giese-Tiemann (G-T) method, which is based on the linear relation between σ_0 and the static conductance of the load, G_s [22]:

$$\sigma_0 = K_p G_s \quad (5.20)$$

where K_p is the probe constant. The value of G_s is evaluated from measurements of the reflection coefficient at longer times (i.e., when the TDR has achieved the steady state, approximately corresponding to the zero-frequency response), of the probe inserted in the MUT, ρ_∞ :

$$G_{s,G-T} = \frac{1}{Z_{TDR}} \frac{1 - \rho_\infty}{1 + \rho_\infty} \quad (5.21)$$

where Z_{TDR} is the output impedance of the used TDR instrument. The value of the probe constant can be estimated from the probe geometry:

$$K_p = \frac{\epsilon_0 c Z_p}{L} \quad (5.22)$$

where L is the length of the used probe, Z_p is the characteristic impedance of the probe, c is the velocity of light in vacuum, and ϵ_0 is the permittivity of vacuum. In (5.22), the evaluation of Z_p is not always an easy task. For this reason, to obtain more accurate estimation of the electrical conductivity, the proportionality constant K_p is usually determined empirically, through multiple preliminary calibration measurements on electrolyte solutions of known conductivity.

The G-T approach neglects the series resistance of the cable, connectors, and cable tester; as a result, for higher electrical conductivity values (i.e., $\sigma_0 > 0.2 \text{ S m}^{-1}$), this method underestimates σ_0 . For this reason, in [28], the series resistor model was introduced, thus considering the coaxial cable and the sample as two resistors in series. The G-T method was modified as follows:

$$\sigma_0 = \frac{K_p}{(1/G_s) - R_{\text{cable}}} \quad (5.23)$$

where R_{cable} is the resistance due to the cable. Castiglione-Shouse (C-S) proposed an alternative approach for taking into account cable resistance; their method required the correction of the measured reflection coefficient by scaling it with respect to the reflection coefficients measured with the probe in air, $\rho_{\infty,\text{air}}$, and short-circuited at the distal end, $\rho_{\infty,\text{sc}}$, respectively [8]:

$$\rho_{\infty,\text{scaled}} = 2 \frac{\rho - \rho_{\infty,\text{air}}}{\rho_{\infty,\text{air}} - \rho_{\infty,\text{sc}}} + 1. \quad (5.24)$$

However, Lin et al. argued that, despite providing accurate results, the C-S method is theoretically incorrect and that the series resistor model is indeed accurate [41]. In particular, Lin et al. suggested that the C-S scaling method actually accounts for

the errors due to imperfect amplitude calibration (and not for cable resistance) and that the C-S method overestimates σ_0 by a constant rate [40, 41]: this error can be compensated for if the probe constant is evaluated every time the measurement setup changes (even when the probes are identically manufactured). On the other hand, the probe constant in the series resistors model has to be determined only once for identical probes, also regardless of the cable length.

Finally, it is worth mentioning that for highly conductive media, because of the strong attenuation of the signal, it becomes difficult to measure simultaneously the apparent dielectric permittivity and the electrical conductivity. In [44], it was shown that for $0.4 \text{ S m}^{-1} < \sigma_0 < 0.75 \text{ S m}^{-1}$, a possible solution could be to insulate the rod-probes with a high-dielectric coating.

5.5.2 *Innovative Calibration Strategies: The TLM and the ICM Methods*

It is apparent from (5.20) and (5.21) that, once K_p is determined for the specific used experimental setup, σ_0 can be easily evaluated through a single TDR measurement on the considered sample. Therefore, the crucial step of this measurement method, and hence the related metrological performance, is strictly related to the accurate evaluation of K_p . Since the estimation of K_p is associated to a preliminary calibration, it goes without saying that the minimization of the systematic errors contributions is strictly related to this procedure; consequently, the evaluation of K_p strongly influences the resulting accuracy in the estimation of σ_0 .

Starting from these considerations, two alternative and innovative approaches for an accurate and simple evaluation of K_p were assessed [13]. Both these methods require only a couple of preliminary measurements: one in air and the other in a reference liquid material, such as water, at known temperature (thus avoiding the otherwise necessary calibration with several reference samples of known conductivity, as required by the traditional C-S method).

The first proposed method allows accurately estimating K_p through the suitable combination of TDR measurements with a specific TLM of the measurement setup.

On the other hand, the second proposed method leads to the accurate estimation of K_p through two ICMs performed through an LCR meter. As will be detailed later, the ICM method has the great advantage of being very rapid, without compromising the final accuracy.

The proposed approaches were validated through repeated σ_0 measurements: 1) on reference electrolyte solutions; 2) on sand samples progressively moistened with de-ionized water; and 3) on sand samples progressively moistened with salted water. The obtained results are compared with those achieved through the traditional C-S method.

Additionally, the performance comparison between C-S and ICM methods is evaluated through a rigorous metrological analysis, which, in turn, provides the measurement uncertainty in the final estimations of σ_0 .

5.5.2.1 TLM Method

In the TLM method, the TDR probe surrounded by the material is considered as a portion of transmission line in which a TEM mode propagates [22, 64, 69]. Considering the proportionality between the static capacitance and the conductance for such a line, and taking into account the relation between the static capacitance per unit length and the characteristic impedance, the following expression can be derived:

$$\sigma_0 = \frac{G_s \epsilon_0 c Z_p}{L}. \quad (5.25)$$

To apply (5.25), Z_p and L have to be accurately determined.

The probe length might be derived from a separate measurement or from the probe datasheet. Nevertheless, the fringing effect at the open end of the probe would be neglected. As for the evaluation of Z_p , for the adopted three-rod probe, an analytical formulation relates the impedance in air to the geometrical parameters of the probe [5]. However, this formulation can only give an approximate value of Z_p , essentially because the probe rods are not perfectly parallel, and their distance slightly varies along the probe. Therefore, these first approximations would limit the accuracy of σ_0 measurements. In order to overcome this limitation, a specific TLM of the experimental setup was developed [21]. This way, by using a suitably implemented optimization procedure it is possible to extrapolate the accurate values for Z_p and L .

More in detail, the experimental measurement system (TDR instrument, cable, and three-rod probe) was modeled through a three-section transmission line, plus some lumped elements in order to accurately take into account the parasitic effects arising from the TDR instrument-to-cable connection and from the probe-head (see Fig. 5.11). The analysis of measured TDR waveforms exhibited a purely inductive effect at the TDR instrument-to-cable connection and a more complex behavior (approximately resembled by a C-L cell) at the probe-head. The TLM was implemented within the microwave circuit simulator AWR Microwave Office (MWO), which allows computing the frequency dependent reflection coefficient at the input section. Subsequently, an inversion processing, based on inverse fast Fourier transform (IFFT), provides the corresponding TDR response.

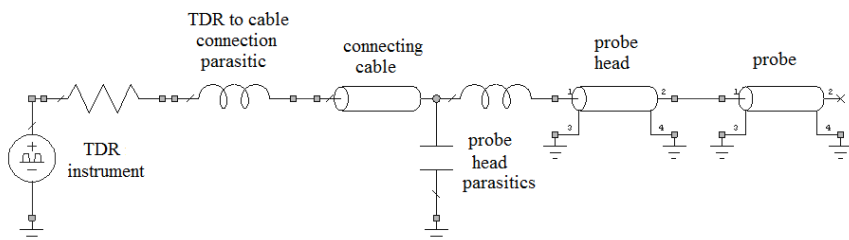


Fig. 5.11 TLM of the experimental setup [13]

The first step of the TLM method involves a couple of TDR measurements, which are performed on the probe in air and immersed in de-ionized water at a known temperature, respectively. Secondly, the same experimental conditions are simulated through the TL model described in Fig. 5.11. Therefore, by employing the simplex optimization procedure (available within MWO), the optimal values of probe length, characteristic impedance, and each parasitic element are evaluated, through the minimization between measured and simulated TDR waveforms.

In these simulations, the frequency dependent dielectric parameters of water are obtained through the well-known Debye modeling [35]. The optimized waveforms (together with the corresponding measured waveforms) are reported in Fig. 5.12(a) for probe in air, and in Fig. 5.12(b) for probe in water, respectively. An excellent fitting quality is observed. The optimized values obtained for Z_p and L are $172\ \Omega$ and 15.2 cm , respectively. It is worth noting that the nominal probe length is 15 cm and that the approximate characteristic impedance is $180\ \Omega$: this value was calculated from the nominal geometrical parameters. The slightly larger length obtained from simulations is attributed to the aforementioned fringing effect of the open-ended termination. As for the optimized value obtained for the characteristic impedance, in the simulation, the non-uniform geometry of the probe is appropriately considered [5]. The obtained values of Z_p and L led to a value of the probe constant, K_p , equal to 3.1 m^{-1} .

Once K_p is estimated, σ_0 can be evaluated through (5.25), measuring the static conductance G_s of the probe immersed in the MUT. In turn, G_s is related to the measured static reflection coefficient: in the TLM method, the ohmic losses of the connecting cable are compensated for through the series resistor-model [28]. Finally, non-idealities in the TDR instrument are corrected by dividing all the values of the measured static reflection coefficients by the one obtained with the output connector left open, whose corresponding ideal value is $+1$. The overall adopted procedure can be summarized in the following steps:

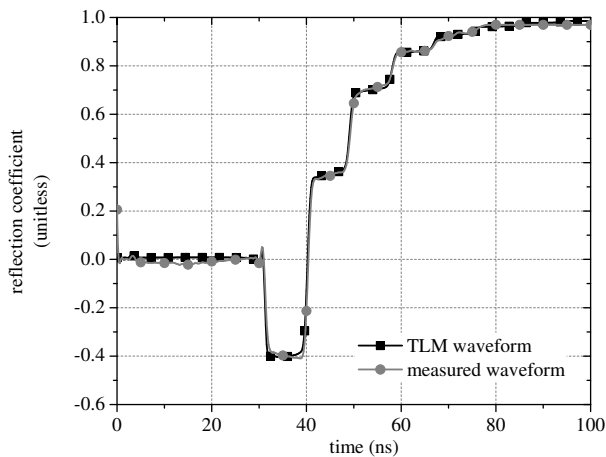
1. the static reflection coefficient, ρ_{oc} , with the TDR instrument output connector left open is measured.
2. The parasitic resistance, R_p , of the connecting cable is evaluated from the static reflection coefficient, ρ_{sc} (appropriately corrected through ρ_{oc}) measured with the probe in air short-circuited at its distal end, i.e.:

$$R_p = Z_0 \frac{1 + \frac{\rho_{oc}}{\rho_{sc}}}{1 - \frac{\rho_{oc}}{\rho_{sc}}} . \quad (5.26)$$

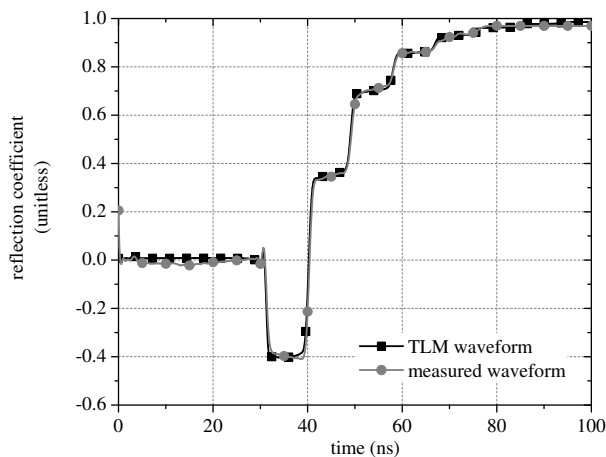
The resistance of the probe rods does not appear in (5.26) since it is negligible compared to the resistance of the cable.

3. The static reflection coefficient with the probe inserted in the MUT (ρ_{sample}), is measured, and the corrected reflection coefficient $\rho_{corr,TLM}$ is derived, i.e.:

$$\rho_{corr,TLM} = \frac{\rho_{sample}}{\rho_{oc}} . \quad (5.27)$$



(a)



(b)

Fig. 5.12 Comparison between measured and simulated TDR waveforms for the probe. **a** in air. **b** in de-ionized water [13]

4. The measured static resistance, R_{meas} , is evaluated by

$$R_{\text{meas}} = Z_0 \frac{1 + \rho_{\text{corr,TLM}}}{1 - \rho_{\text{corr,TLM}}} . \quad (5.28)$$

5. The probe static resistance is obtained subtracting R_p from R_{meas}
 6. Once the static resistance and, hence, the conductance, are evaluated, the static conductivity is finally obtained from (5.25).

It is important to emphasize that the proposed TLM method can virtually take into account every single parasitic contribution associated to a specific experimental setup. As a result, the influence of systematic error contributions is dramatically reduced.

5.5.2.2 ICM Method

Considering a TEM mode propagating through the three-rod probe, the characteristic impedance of the probe in air may be written as follows:

$$Z_p = \frac{1}{cC_0} \quad (5.29)$$

where C_0 is the capacitance per unit length of the probe in air. Combining (5.25) and (5.29), the following expression is obtained:

$$\sigma_0 = \frac{G_s \varepsilon_0}{C_{s0}} = G_s K_p \quad (5.30)$$

where $C_{s0} = C_0 L$ is the capacitance of the probe in air.

When the probe is inserted in a sample material, the quasi-static capacitance of the probe will include two contributions: 1) a parasitic capacitance, C_p , that is due to the connecting coaxial cable and to the probe-head; 2) the static capacitance of the probe filled with the MUT, C_s . Therefore, the total capacitance measured through an LCR meter, C_m , will be given by the following expression:

$$C_m = C_p + C_s = C_p + C_{s0} \varepsilon_s \quad (5.31)$$

where ε_s is the static permittivity of the material filling the probe.

Consequently, from ICMs on two materials with well-known static dielectric permittivity (ε_{s1} and ε_{s2} , respectively), it is possible to retrieve the value of C_p and, most importantly, of C_{s0} , according to

$$C_{s0} = \frac{C_{m2} - C_{m1}}{\varepsilon_{s2} - \varepsilon_{s1}} \quad (5.32)$$

where C_{m1} and C_{m2} are the LCR-measured capacitances in the two reference materials, respectively. Finally, from (5.30), it is possible to estimate K_p .

For the ICM method, the Agilent 4263B LCR meter was used directly connected to the TDR probe; and air [66] and pure water [24] were chosen as reference materials. LCR measurements were performed at a frequency of 100 kHz, with a measurement average of 256 and temperature kept constant at 25°C. LCR measurements showed that, at this frequency, the probe behaves just like a capacitor; in fact, the phase angle of the corresponding impedance resulted approximately -90° , thus confirming the validity of the approximations introduced using (5.31)⁸.

⁸ It is worth mentioning that, at 100 kHz, the dielectric behavior of air and water is practically static, thus dissipative and dispersive effects are avoided.

The advantage of the ICM method is that, thanks to the simplicity of the used equations, it leads very rapidly and without much effort to the estimation of K_p .

5.5.3 Validation of the Methods

The experimental setup for the reflectometry measurements includes the HL1500 TDR unit [4], the 15 cm-long three-rod probe (Campbell Scientific CS630) [3], and a 3.5 m-long 50 Ω -matched coaxial cable.

The first step was the evaluation of the probe constant $K_{p,C-S}$ to be used for subsequent measurements based on the C-S method. After preparing nine electrolyte solutions, the corresponding values of $\sigma_{0,ref}$ were measured through a conductivity meter and considered as reference values. The value of $K_{p,C-S}$ was evaluated from the linear fitting of the measurement points in the $G_s - \sigma_0$ plane, as shown in Fig. 5.13. The obtained value for $K_{p,C-S}$ is 2.9 m^{-1} , whereas the corresponding standard uncertainty evaluated according to the formulation described in [13] is $u_{Kp} = 0.2 \text{ m}^{-1}$.

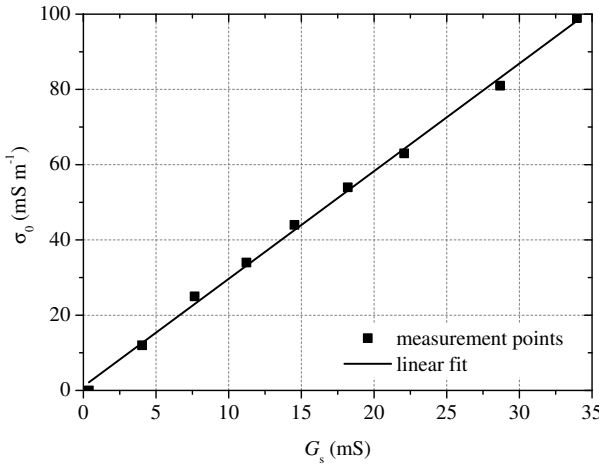


Fig. 5.13 $G_s - \sigma_{0,ref}$ regression curve obtained from the measurements on nine electrolyte solutions differing in reference electrical conductivities. The curve slope gives the K_p to be used for the estimation of σ_0 through the C-S method [13]

At the same time, TDR waveforms at longer distances were acquired on the same electrolyte solutions and were used to calculate G_s for each electrolyte solution, as the average value of TDR measurements in the considered long-distance range. Fig. 5.14 shows the typical TDR waveforms measured for the nine electrolyte solutions, which differed in reference values of electrical conductivity. It can be seen that the waveforms are quite stable in the distance range 750–1250 m; therefore,

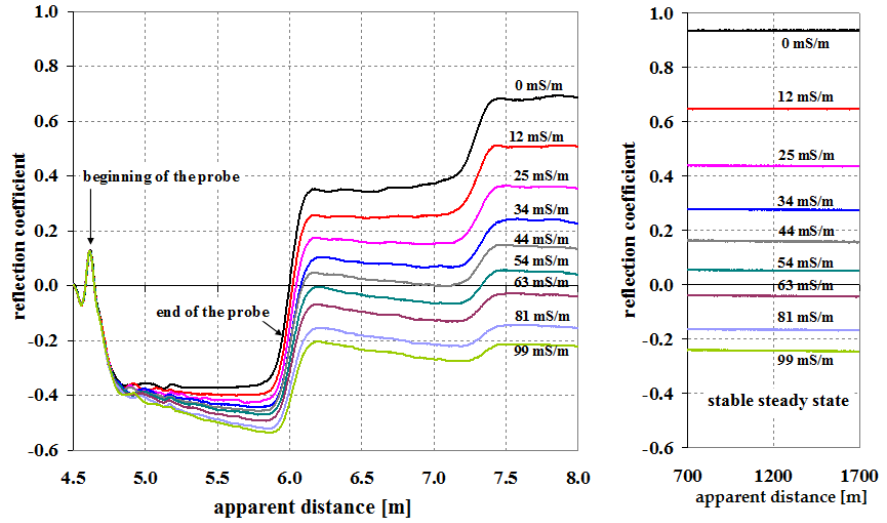


Fig. 5.14 TDR waveforms acquired at longer distances on nine electrolyte solutions differing in reference electrical conductivities (left). The behavior of the same waveforms at the steady-state condition is also reported (right) [13]

the static reflection coefficients and the corresponding evaluated uncertainties were referred to this range.

Successively, the values of the electrical conductivities ($\sigma_{0,TLM}$) of the electrolyte solutions were also evaluated through the TLM method using, however, the same TDR waveforms. To this purpose, preliminary TDR measurements with the probe in air and in pure water were performed in order to obtain the optimized values for the TLM model parameters, as discussed in the previous sections.

Furthermore, considering the TDR-probe in air and in pure water, and performing capacitance measurements, the probe constant deriving from the ICM method was estimated, as detailed in the previous sections. Results are summarized in Table 5.3, in which the measured C_m , and the estimated $K_{p,ICM}$ are reported along with the corresponding absolute standard uncertainties.

The electrical conductivities deriving from the ICM method, $\sigma_{0,ICM}$, were evaluated for the electrolyte solutions.

Table 5.4 shows the comparison between the experimental results for $\sigma_{0,TLM}$ and $\sigma_{0,ICM}$, obtained on the reference electrolyte solutions. The good agreement among results provides a useful preliminary validation of the two considered approaches.

After the preliminary validation of the method on reference electrolyte solutions, the described methods were used to measure the electrical conductivity of moistened sand. To this purpose, sand samples were watered at ten different moisture levels (ten samples were moistened with de-ionized water and ten with salted water), thus obtaining a wide range of experimental conditions. TDR waveforms at

Table 5.3 Results for LCR capacitance measurements on pure water and air. The corresponding literature values of static permittivities and the estimated K_p value are also reported, with associated standard uncertainties

material	C_m (pF)	ϵ_s	$K_{p,ICM}$ (m^{-1})
air	294.07 ± 2.85	1.0005 ± 0.0002	3.1 ± 0.1
water	517.13 ± 4.27	78.5 ± 0.1	

Table 5.4 Comparison between static electrical conductivities of electrolyte solutions (at different $\sigma_{0,ref}$) evaluated through the TLM ($\sigma_{0,TLM}$) and the ICM ($\sigma_{0,ICM}$) methods. The absolute standard uncertainty (only for the ICM method) is also reported

$\sigma_{0,TLM}$ (mSm^{-1})	$\sigma_{0,ICM}$ (mSm^{-1})
1.2	1.2 ± 0.1
12.6	12.3 ± 0.3
23.8	23.3 ± 0.6
35.0	34.2 ± 0.8
45.2	44.3 ± 1.1
56.7	55.5 ± 1.3
68.8	67.4 ± 1.6
89.3	87.5 ± 2.1
105.8	103.6 ± 2.5

longer distances were acquired on all the prepared samples, and the corresponding electrical conductivity values ($\sigma_{0,C-S}$, $\sigma_{0,TLM}$, and $\sigma_{0,ICM}$) were evaluated.

Table 5.5 and Table 5.6 summarize the results obtained for the σ_0 measurements (through the C-S, the TLM, and the ICM methods), on sand moistened with de-ionized water and on sand moistened with salted water, respectively. The obtained results show an overall good agreement among the values obtained through the three methods. In particular, considering the sand samples, it is worth noting that the uncertainty related to the ICM method is always lower than the uncertainty related to the C-S method: this is particularly evident for higher moisture levels.

It is important to note that the final uncertainty on $\sigma_{0,C-S}$ and $\sigma_{0,ICM}$ is mostly due to the uncertainty in the evaluation of the probe constant through the C-S method and through the ICM method, respectively. In fact, the percentage standard uncertainties are 7.5% and 2.3%, for $K_{p,C-S}$ and $K_{p,ICM}$, respectively. Conversely, the contributions of the uncertainty related to the other quantities involved (i.e., ρ_{sample} , ρ_{oc} , ρ_{sc}) hardly influences the final uncertainty of the calculated value of σ_0 . In fact, the maximum values of the percentage standard uncertainty for static reflection coefficients, not reported here for the sake of brevity, are in the order of 0.15%.

Table 5.5 Results obtained for measurements on sand samples mixed with deionized water, at ten different moisture levels. The estimated values for $\sigma_{0,C-S}$; $\sigma_{0,TLM}$; and $\sigma_{0,ICM}$ and for the corresponding standard uncertainties are compared

θ (%)	$\sigma_{0,C-S}$ (mS m ⁻¹)	$\sigma_{0,TLM}$ (mS m ⁻¹)	$\sigma_{0,ICM}$ (mS m ⁻¹)
0.0	-	0.0	-
2.0	0.6 ± 0.1	0.8	0.7 ± 0.1
4.0	1.4 ± 0.1	1.6	1.6 ± 0.1
6.0	2.6 ± 0.2	2.9	2.9 ± 0.1
9.1	3.6 ± 0.3	4.1	4.0 ± 0.1
12.1	4.2 ± 0.3	4.7	4.6 ± 0.1
15.1	5.7 ± 0.4	6.4	6.3 ± 0.1
18.1	7.3 ± 0.6	8.1	8.0 ± 0.2
21.1	11.5 ± 0.9	12.7	12.4 ± 0.3
24.4	15.7 ± 1.2	17.3	16.9 ± 0.4

Table 5.6 Results obtained for measurements on sand samples mixed with salted water, at ten different moisture levels. The estimated values for $\sigma_{0,C-S}$, $\sigma_{0,TLM}$ and $\sigma_{0,ICM}$ and for the corresponding standard uncertainties are compared

θ (%)	$\sigma_{0,C-S}$ (mS m ⁻¹)	$\sigma_{0,TLM}$ (mS m ⁻¹)	$\sigma_{0,ICM}$ (mS m ⁻¹)
0.0	-	0.0	-
2.0	0.8 ± 0.1	1.0	1.0 ± 0.1
4.0	2.5 ± 0.2	2.8	2.7 ± 0.1
6.0	4.1 ± 0.3	4.6	4.5 ± 0.1
9.1	6.3 ± 0.5	7.0	6.9 ± 0.2
12.1	9.9 ± 0.8	11.0	10.8 ± 0.3
15.1	14.3 ± 1.1	15.8	15.6 ± 0.4
18.1	20.2 ± 1.5	22.3	21.8 ± 0.5
21.1	30.7 ± 2.3	33.8	33.0 ± 0.8
24.5	41.5 ± 3.1	45.6	44.6 ± 1.1

Finally, it must be pointed out that the $K_{p,C-S}$ was evaluated through nine preliminary measurements on the electrolyte solutions, and it was found that $\mu_{Kp,C-S}$ increases dramatically when less than nine points were considered for the linear regression. Conversely, only two preliminary measurements were enough to obtain an accurate estimation of the probe constant through the ICM method. This is one of the major advantages of the described methods.

5.5.4 *Practical Considerations*

Preliminary results obtained comparing the traditional and the described methods highlighted similar performance in terms of estimation of the electrical static conductivity, both for the electrolyte solutions and for the moistened sand samples. However, it is important to underline that the two proposed approaches are advantageous in two major ways. In fact, the TLM method clearly discovers and compensates for the major parasitic effects that influence the final measurement accuracy. As for the ICM method, the simple requirement of two capacitance measurements simplifies and speeds up the entire procedure. Additionally, the addressed metrological validation clearly demonstrates that the uncertainty in the estimation of electrical conductivity through the ICM method is always smaller than (or, at worst, equal to) the uncertainty related to the traditional C-S method. On such basis, the described approaches represent a viable way toward a cost-effective and time-saving TDR monitoring of conductivity for quality control of both liquid and granular materials.

5.6 Noninvasive Moisture Content Measurements

In some monitoring or diagnostic applications, the noninvasive approach may represent a stringent requirement. Therefore, with regards to the BMR capabilities to satisfy such needs, much research effort has been paid to designing and realizing probes that could guarantee a noninvasive approach. For example, metallic strips have been investigated as possible surface-TDR probes [58]. Similarly, serpentine-shaped wires (attached to a planar acrylic pad) have also been considered as a noninvasive solution for BMR-based moisture monitoring [59].

Starting from these considerations, in this section, the possibility of noninvasive moisture monitoring through a suitable combination of BMR with the use of a microstrip antenna as sensing element is addressed. This method may become particularly suitable for monitoring applications in which the noninvasive approach is mandatory (e.g., construction materials, walls, architectonic structures, frescoes, etc.).

As will be detailed in the following subsections, the dielectric properties of the considered material are associated to the changes in the reflection scattering parameter of the antenna, $S_{11}(f)$, occurring when the antenna is placed in contact with the surface of the MUT [57]. More specifically, the changes in the resonant frequency (f_{res}) of the antenna can be associated to the moisture content of the MUT.

The main steps of the adopted method can be summarized as follows:

- a microstrip antenna (which can be specifically designed and realized) is placed on the surface of the MUT, and the TDR waveform of the system (antenna and MUT) is acquired [see Fig. 5.15];
- the $S_{11}(f)$ of the system is evaluated through the TD/FD combined approach described in Chapt. 3 [9];

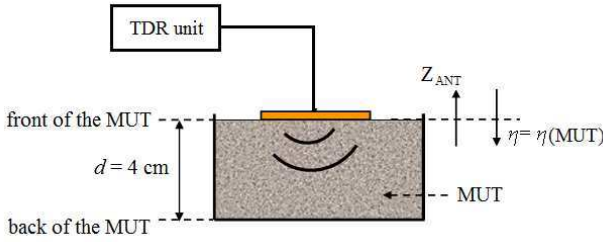


Fig. 5.15 Schematic diagram of the experimental setup used for the noninvasive measurements [12]

- the $S_{11}(f)$ is used to evaluate the resonant frequency of the system (occurring at the minimum of the $S_{11}(f)$ curve); and finally,
- the evaluated f_{res} is associated to the moisture level of the sample.

As well known, changes in the resonant frequency of the antenna could be directly determined through a vector network analyzer (VNA). However, as already mentioned, using a TDR instrument in place of a VNA can reduce the costs related to the experimental setup. In this regard, as also mentioned in previous cases, although the reported results were obtained through the TDR80E04 [61], a benchtop and expensive instrument, the proposed method can be equally implemented using affordable TDR instruments.

5.6.1 Basic Theory of Microstrip Antennas

Before proceeding with the detailed description of the experimental procedure, in this subsection the basic theoretical aspects behind the proposed method are addressed.

A microstrip antenna consists of a dielectric substrate with a radiating patch on one side and a ground plane on the other side [see Figs 5.16(a) and 5.16(b)]. This kind of antennas is inexpensive to be fabricated, and a high level of reproducibility can be achieved. As well known, an antenna is characterized by its resonant frequency, which is defined by the following equation [37]:

$$f_{\text{res}} = \frac{c}{2L_{\text{eff}}\sqrt{\epsilon_{\text{eff}}}} \quad (5.33)$$

where $c \cong 3 \times 10^8 \text{ m s}^{-1}$ is the speed of light in free space, L_{eff} is the effective length of the radiating patch, and ϵ_{eff} is the effective relative permittivity of the antenna. L_{eff} and ϵ_{eff} can be evaluated considering the following equations:

$$L_{\text{eff}} = L + 2\Delta L = L + \frac{2h}{\sqrt{\epsilon_{\text{eff}}}} \quad (5.34)$$

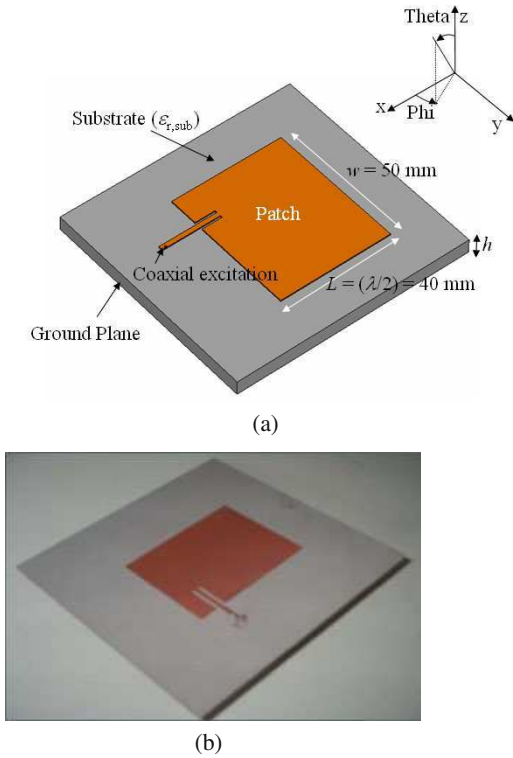


Fig. 5.16 **a** geometric configuration of the microstrip antenna. **b** photograph of the used antenna [12]

$$\epsilon_{\text{eff}} = \frac{\epsilon_{r,\text{sub}} + \epsilon_m}{2} + \frac{\epsilon_{r,\text{sub}} - \epsilon_m}{2} \left[1 + \left(10 \frac{h}{w} \right) \right]^{-1/2} \quad (5.35)$$

where $\epsilon_{r,\text{sub}}$ is the relative permittivity of the antenna substrate; h is its thickness; w and L are the width and the length of the radiating patch, respectively; and ϵ_m is the relative permittivity of the medium in which the antenna radiates [see Fig. 5.16] [65, 70].

Considering the previous formulas, when the antenna radiates in free space, then ϵ_m equals 1 (which is the relative permittivity of air), and the antenna will resonate at a specific frequency, $f_{\text{res}}^{\text{air}}$. On the other hand, when a different material is placed in front of the antenna, ϵ_m changes, and f_{res} will change accordingly. The direct implication is that the resonant frequency is closely related to the dielectric characteristics of the medium in which the antenna radiates.

As for the practical evaluation of f_{res} , it can be measured from the minimum of the magnitude of $S_{11}(f)$, which is given by

$$|S_{11}| = \left| \frac{\eta - Z_{\text{ANT}}}{\eta + Z_{\text{ANT}}} \right| \quad (5.36)$$

where $\eta = \sqrt{\mu_0/\epsilon_m}$ and Z_{ANT} is the antenna impedance. Equation (5.36) shows that $S_{11}(f)$ of the antenna is intrinsically associated to ϵ_m .

It is important to underline that in the previous equations the thickness of the material sample (d) in front of the antenna is assumed as semi-infinite. This assumption remains valid as long as the power fed into the antenna is sufficiently low. In this way, the antenna is not affected by what is beyond the back of the MUT (i.e., only the reflections at the front-face of the MUT have to be considered) [see Fig. 5.15].

It is worth pointing out that Eqs. (5.33) - (5.35) represent a simplified model for describing the dependence of the resonant frequency on the relative dielectric permittivity. Indeed, a more accurate model should also take into account the effect of dielectric losses (by considering the complex relative permittivity of the material in which the antenna radiates) and the thickness of the MUT [6]. Nevertheless, as confirmed by the experiments reported in the following subsection, (5.33) - (5.35) provide sound qualitative information on the dependence of f_{res} on ϵ_m .

5.6.2 *Experimental Validation of the Method: Measurements on Moistened Sand Samples*

The used antenna is a simple and inexpensive $\lambda/2$ -resonant microstrip antenna realized on an RF35 substrate with a coaxial/transmission-line excitation [see Fig. 5.16]; its working frequency (in air) is approximately 2 GHz.

The antenna was fed through an SMA connector, thus allowing performing the SOL calibration measurements as required by the TD/FD combined approach [11].

5.6.2.1 Validation of the Method on Reference Materials

Preliminary measurements with the antenna used as probe were performed on seven well-referenced materials: air, butan-1-ol, n-hexane, chlorobenzene, 2-heptanol, 2-propanol, and iso-propoxyethanol. This was done for validating the theoretical model described by Eqs. (5.33)-(5.35), thus verifying the direct relation between ϵ_m and the corresponding f_{res} .

The reference liquids were placed inside the box; the antenna was placed in contact with each of them, and the corresponding resonant frequency ($f_{\text{res-ref}}$) was measured. The frequency-dependent permittivities of the reference liquids were measured according to the procedure described in Chapt. 3 and compared with reference values reported in [7] and [24]. A good agreement between measured and theoretical data was observed [12].

5.6.2.2 Measurements on Sand Samples

After the validation of the reference-model, the proposed method was tested on three different types of construction sand, differing in granulometry (ranging from approximately 1 mm to 4 mm) and composition (sand #1 and sand #2 were siliceous sands, whereas sand #3 was a calcareous sand). Moisture measurements were performed on sand samples brought at increasing (pre-established) levels of moisture, through the gravimetric method. Each gravimetric water content progressively achieved was then associated to the corresponding volumetric water content (θ) through the mass density of the sand. It is important to underline that samples were moistened almost up to water saturation level. In this way, for each type of sand, a wide range of reference moisture levels was obtained (referred to as s_1, s_2, \dots, s_6 , respectively).

The TDR80E04 was also used for performing ‘traditional’ comparative TDR measurement on the same samples. For this purpose, the apparent relative permittivity values of the reference samples, ϵ_{app} , were evaluated (directly in TD) through separate measurements of the apparent length (L_{app}) of the 15 cm-long three-rod probe (Campbell CS630) inserted into the MUT. The ϵ_{app} values were evaluated through (5.5) [2]. Successively, on the same sample, measurements were carried out using the antenna as a probe. For the measurements with the antenna, the sample was placed in a top-opened plastic box with dimensions 20 cm \times 20 cm \times 4 cm. Full-wave electromagnetic simulations of the radiation pattern of the antenna, confirmed that boundary effects caused by the box were negligible.

For all the samples (s_1, s_2, \dots, s_6) of each sand, the $S_{11}(f)$ of the antenna in contact with the MUT was evaluated.

As an example, the changes in the $S_{11}(f)$ magnitude curves for increasing values of moisture of the MUT for sand #3 are shown in Fig. 5.17: starting from the antenna in air, each curve refers to a different moisture level (θ) ranging from 0% (s_1) to the maximum considered moisture level (s_6).

To have a tentative value of the relative permittivity of the MUT, traditional comparative TDR measurement of the ϵ_{app} were performed, so as to associate these data to the f_{res} measured for the same sample. Results are summarized in Table 5.7.

As expected, as water content is increased, the value of ϵ_{app} progressively differs from the value of the theoretical ϵ_m . This behavior is mainly attributable to two main effects. The first is the fact that dielectric losses become more relevant as the amount of water is increased. In fact, the measured ϵ_{app} carries a strong contribution of the imaginary part of the relative permittivity (ϵ''), and cannot be merely assumed equal to ϵ' . In this case, the theoretical model should include a correction factor accounting for ϵ'' [6]. Secondly and more importantly, as discussed in [6] and as confirmed by measurements, the proposed method is best suited for monitoring materials whose corresponding relative permittivity does not exceed 10–12. For higher permittivity values, due to the intrinsic degradation of the resonant behavior of microstrip antennas, a strong attenuation of the resonance effect is observed. Therefore, the theoretical model described by Eqs. (5.33)–(5.35) becomes less accurate in describing the changes in the resonant frequency as a function of the permittivity. Deviation between ϵ_m and ϵ_{app} are highlighted, for sand #3, in Table 5.8.

Table 5.7 Resonant frequencies (f_{res}) associated to the pre-established water content level (θ) corresponding to the apparent permittivity values (ϵ_{app}), for each type of sand (#1, #2, #3) [12]

<i>sand #1 (granulometry $\leq 1 \text{ mm}$)</i>			
MUT	$\theta \text{ (cm}^3/\text{cm}^3\text{)}$	ϵ_{app}	$f_{\text{res}} \text{ (GHz)}$
s1	0.000	2.75	1.958
s2	0.031	3.22	1.955
s3	0.062	3.94	1.949
s4	0.093	4.72	1.944
s5	0.124	5.39	1.909
s6	0.156	6.55	1.885

<i>sand #2 (granulometry $2 \div 4 \text{ mm}$)</i>			
MUT	$\theta \text{ (cm}^3/\text{cm}^3\text{)}$	ϵ_{app}	$f_{\text{res}} \text{ (GHz)}$
s1	0.000	2.80	1.965
s2	0.034	3.13	1.958
s3	0.067	3.54	1.949
s4	0.101	4.85	1.941
s5	0.137	6.29	1.906
s6	0.171	7.30	1.906

<i>sand #3 (granulometry 2 mm)</i>			
MUT	$\theta \text{ (cm}^3/\text{cm}^3\text{)}$	ϵ_{app}	$f_{\text{res}} \text{ (GHz)}$
s1	0.000	3.91	1.949
s2	0.038	4.13	1.947
s3	0.076	4.66	1.930
s4	0.114	5.69	1.912
s5	0.153	8.33	1.891
s6	0.191	10.14	1.866

Results reported herein show that the proposed method provides good results for volumetric moisture content lower than 20% (e.g., in the considered cases $\epsilon_{\text{app}} \cong 10$). Fig. 5.18 shows the final calibration curves relating the resonant frequency of each moistened sample to the corresponding moisture level. The curve of sand #3 is evidently more linear than the curves referred to sand #1 and sand #2: this is attributed to the different granulometric and porosimetric characteristics of the considered sands. In fact, the grains of sand #3 have rather uniform dimensions (2 mm). Conversely, the grains of sand #1 and of sand #2 have different dimensions (in the ranges reported in Table 5.7). For this reason, for lower moisture levels sand

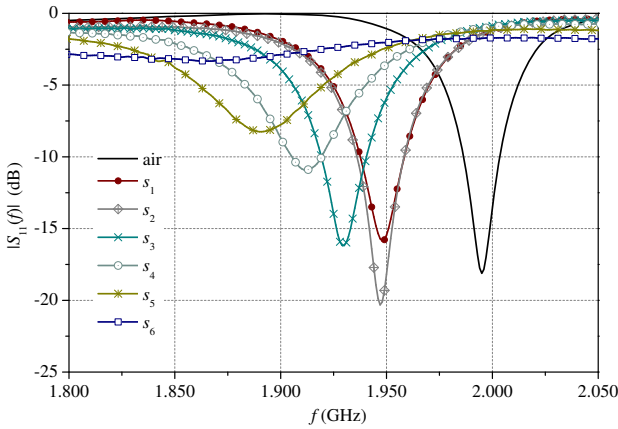


Fig. 5.17 Magnitude of $S_{11}(f)$, for increasing moisture levels (s_1 being dry sand) for sand #3 [12]

Table 5.8 Deviation between theoretical values relative permittivity (ϵ_m) and measured apparent permittivities (ϵ_{app}) corresponding to each moisture content level, for sand #3 [12]

moistened MUT	θ (cm^3/cm^3)	ϵ_m	$\Delta\epsilon = (\epsilon_m - \epsilon_{app})$
s1	0.000	5.18	1.27
s2	0.038	5.39	1.26
s3	0.076	7.19	2.53
s4	0.114	9.33	3.64
s5	0.153	11.8	3.47
s6	0.191	14.8	4.66

#1 and sand #2 show a similar behavior; on the other hand, as the moisture content increases, the two curves show a different trend, since granulometry and porosity start to affect differently the water absorption behavior.

5.6.2.3 Effect of Electrical Conductivity

Considering Fig. 5.17, as the water content is increased, two combined effects can be noticed: a shift of f_{res} towards lower frequencies, and a change in the value of the minimum of $|S_{11}(f)|$. The first is mainly attributable to a change of the real part of the permittivity, whereas the variation in the minimum of the $S_{11}(f)$ magnitude is influenced both by the real and by the imaginary parts of the relative permittivity of the watered material.

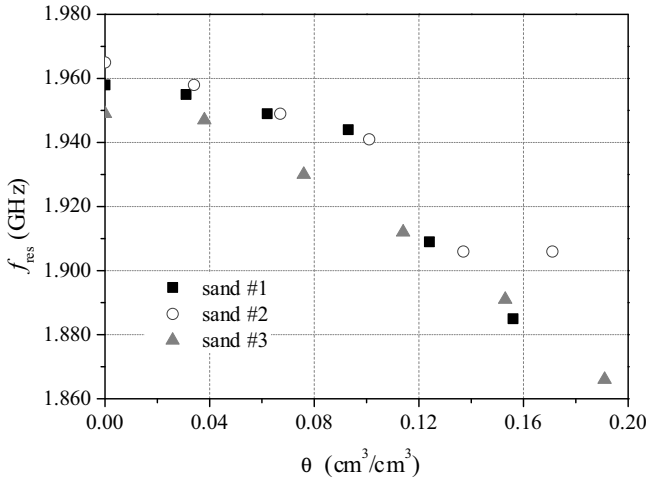


Fig. 5.18 Calibration curves relating the resonant frequency of the antenna (f_{res}) to the corresponding moisture content of the MUT (θ) for the three types of sand [12]

As a further validation of these results and to investigate how the imaginary permittivity influences the $S_{11}(f)$, full-wave simulations were performed through a commercial simulator, CST Microwave Studio. More specifically, the time-domain solver, based on the well-known Finite Integration Technique, was used. Simulations were performed by varying the value of the electrical conductivity of the MUT (σ_{MUT}), for several fixed values of the real part of the dielectric permittivity (ϵ_{MUT}).

Fig. 5.19 shows how the minimum of the $S_{11}(f)$ magnitude changes as a result of variations of σ_{MUT} . It can be seen that when the permittivity is higher than 3, an increase of the electric conductivity causes $|S_{11}(f)|$ to decrease. Simulation results in Fig. 5.19 are also compared to measurements performed on sand samples moistened with approximately the same amount of bi-distilled water ($\theta = 8\%$), with a conductivity ranging from 0 to 107 mS m⁻¹. The experimental trend is in good agreement with the simulations.

5.6.2.4 Sensing Volume

Another aspect that is worth taking into account is the sensing volume, which represents an issue also for traditional moisture content measurements. For a given antenna, the sensing volume mainly depends on the relative permittivity of the MUT. To assess how the relative permittivity of the MUT affects the sensing volume, full-wave simulations were performed through CST Microwave Studio. For different fixed values of dielectric permittivity, the thickness of the MUT was progressively increased, and the corresponding changes in the resonant frequency of the antenna were observed. Results of these simulations are shown in Fig. 5.20.

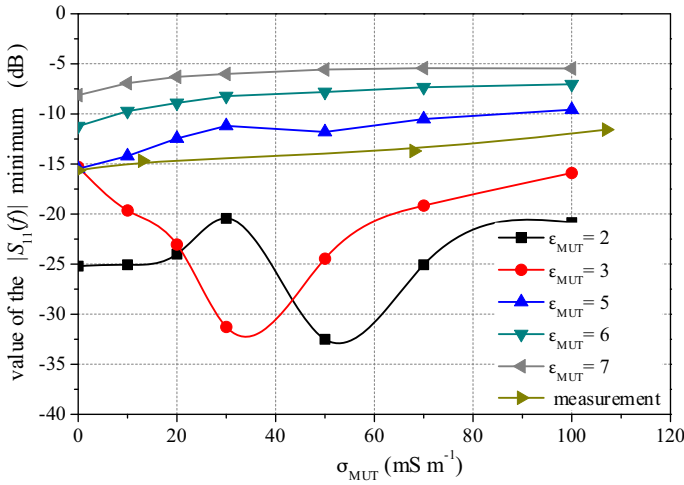


Fig. 5.19 Comparison between simulation results (for different fixed permittivity values) and experimental measurements performed on 8% -moistened sand #3 with a water conductivity ranging from 0 to 107 mS m⁻¹ [12]

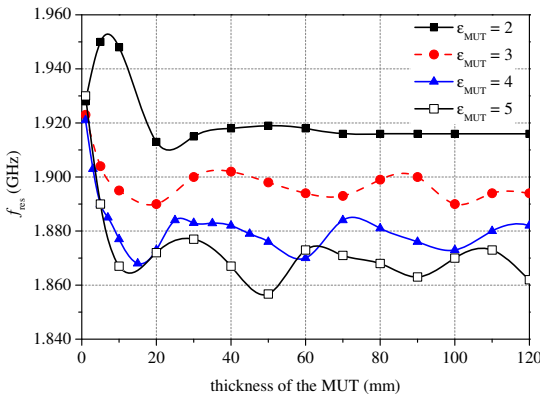


Fig. 5.20 Full-wave simulation results showing the change in the resonant frequency (f_{res}) as a function of the thickness of the MUT, for several fixed values of ϵ_{MUT} [12]

As a result, for an assumed dielectric permittivity, the predicted sensing volume can be associated to the maximum sample thickness beyond which no relevant changes in resonant frequency are present. It must be pointed out that simulations were performed considering a MUT with fixed transverse dimensions (20 cm \times 20 cm) and varying thickness; indeed, a more rigorous analysis of the sensing volume should consider infinite transverse dimensions. However, considering the directivity of the used (and simulated) antenna, the sensing volume analysis reported herein can be considered adequately accurate.

References

- [1] Network analyzer basics, USA (2004)
- [2] Time domain reflectometry theory. Agilent Application Note 1304-2, Palo Alto, CA, (2006)
- [3] TDR probes CS605, CS610, CS630, CS635, CS640, CS645 instruction manual - revision 2/09. Logan, UT (2009),
<http://www.campbellsci.com/documents/manuals/tdr-probes.pdf>
 (cited December 27, 2010)
- [4] TDR100 instruction manual - revision 2/10. Logan, UT (2010),
<http://www.campbellsci.com/documents/manuals/tdr100.pdf>
 (cited December 27, 2010)
- [5] Ball, J.A.R.: Characteristic impedance of unbalanced TDR probes. *IEEE Trans. Instrum. Meas.* 51(3), 532–536 (2002)
- [6] Bogosanovich, M.: Microstrip patch sensor for measurement of the permittivity of homogeneous dielectric materials. *IEEE Trans. Instrum. Meas.* 49(5), 1144–1148 (2000)
- [7] Buckley, F., Maryott, A.A.: Tables of dielectric dispersion data for pure liquids and dilute solutions. National Bureau of Standards Circular 589 (1958)
- [8] Castiglione, P., Shouse, P.J.: The effect of ohmic losses on time-domain reflectometry measurements of electrical conductivity. *Soil Sci. Soc. Am. J.* 67, 414–424 (2003)
- [9] Cataldo, A., Catarinucci, L., Tarricone, L., Attivissimo, F., Trotta, A.: A frequency-domain method for extending TDR performance in quality determination of fluids. *Meas. Sci. Technol.* 18(3), 675–688 (2007)
- [10] Cataldo, A., Cannazza, G., De Benedetto, E., Tarricone, L., Cipressa, M.: Metrological assessment of TDR performance for moisture evaluation in granular materials. *Measurement* 42(2), 254–263 (2009)
- [11] Cataldo, A., Catarinucci, L., Tarricone, L., Attivissimo, F., Piuze, E.: A combined TD-FD method for enhanced reflectometry measurements in liquid quality monitoring. *IEEE Trans. Instrum. Meas.* 58(10), 3534–3543 (2009)
- [12] Cataldo, A., Monti, G., De Benedetto, E., Cannazza, G., Tarricone, L.: A noninvasive resonance-based method for moisture content evaluation through microstrip antennas. *IEEE Trans. Instrum. Meas.* 58(5), 1420–1426 (2009)
- [13] Cataldo, A., Piuze, E., Cannazza, G., De Benedetto, E.: Improvement and metrological validation of TDR-methods for the estimation of static electrical conductivity. *IEEE Trans. Instrum. Meas.* 59(5), 1207–1215 (2010)
- [14] Cerny, R.: Time-domain reflectometry method and its application for measuring moisture content in porous materials: a review. *Measurement* 42(3), 329–336 (2009)
- [15] Corwin, D.L., Lesch, S.M.: Apparent soil electrical conductivity measurements in agriculture. *Comp. Electron. Agric.* 46(1-3), 11–43 (2005)
- [16] Dalton, F.N., Herkelrath, W.N., Rawlins, D.S., Rhoades, J.D.: Time-domain reflectometry: simultaneous measurement of soil water content and electrical conductivity with a single probe. *Science* 224(4652), 898–990 (1990)
- [17] Dasberg, S., Dalton, F.N.: Time domain reflectometry field measurements of soil water content and electrical conductivity. *Soil Sci. Soc. Am. J.* 49, 293–297 (1985)
- [18] Dehghanisanij, H., Agassi, M., Anyoji, H., Yamamoto, T., Inoue, M., Eneji, A.E.: Improvement of saline water use under drip irrigation system. *Agric. Water Manag.* 85(3), 233–242 (2006)

- [19] Dirksen, C., Dasberg, S.: Improved calibration of time-domain reflectometry soil water content measurements. *Soil Sci. Soc. Am. J.* 57, 660–667 (1993)
- [20] Dobson, M.C., Hallikainen, M.T.: Microwave dielectric behavior of wet soil-part ii: dielectric mixing models. *IEEE Trans. Geosci. Remote Sens.* 23(1), 35–46 (1985)
- [21] Feng, W., Lin, C.P., Deschamps, R.J., Drnevich, V.P.: Theoretical model of a multisection time domain reflectometry measurement system. *Water Resour. Res.* 35(8), 2321–2331 (1999)
- [22] Giese, K., Tiemann, R.: Determination of complex permittivity from thin-sample time domain reflectometry: improved analysis of the step response waveform. *Mol. Relax. Process.* 7, 45–59 (1975)
- [23] Greco, R.: Soil water content inverse profiling from single TDR waveforms. *J. Hydrol.* 317(3–4), 325–339 (2006)
- [24] Gregory, A.P., Clarke, R.N.: Traceable measurements of the static permittivity of dielectric reference liquids over the temperature range 5–50°C. *Meas. Sci. Technol.* 15(7), 1506–1516 (2005)
- [25] Hamed, Y., Persson, M., Berndtsson, R.: Soil solution electrical conductivity measurements using different dielectric techniques. *Soil. Sci. Soc. Am. J.* 67(4), 1071–1078 (2003)
- [26] Hasted, J.B.: *Aqueous dielectric*. Chapman and Hall, UK (1973)
- [27] Heimovaara, T.J.: Frequency domain analysis of time domain reflectometry waveforms: I. measurement of the complex dielectric permittivity of soils. *Water Resour. Res.* 30(2), 189–199 (1994)
- [28] Heimovaara, T.J., Focke, A.G., Bouten, W., Verstraten, J.M.: Assessing temporal variation in soil water composition with time domain reflectometry. *Soil. Sci. Soc. Am. J.* 59, 689–698 (1995)
- [29] Heimovaara, T.J., Huisman, J.A., Vrugt, J.A., Bouten, W.: Obtaining the spatial distribution of water content along a TDR probe using the SCEM-UA bayesian inverse modeling scheme. *Vadose Zone J.* 3, 1128–1145 (2004)
- [30] Hendrickx, J.M.H., Borchers, B., Corwin, D.L., Lesch, S.M., Hilgendorf, A.C., Schlue, J.: Inversion of soil conductivity profiles from electromagnetic induction measurements: theory and experimental verification. *Soil. Sci. Soc. Am. J.* 66, 673–685 (2002)
- [31] Hilhorst, M.A., Dirksen, C., Kampers, F.W.H., Feddes, R.A.: New dielectric mixture equation for porous materials based on depolarization factors. *Soil Sci. Soc. Am. J.* 64, 1581–1587 (2000)
- [32] Huisman, J.A., Weerts, A.H., Heimovaara, T.J., Bouten, W.: Comparison of travel time analysis and inverse modeling for soil water content determination with time domain reflectometry. *Water Resour. Res.* 38(6), 13.1–13.8 (2002)
- [33] Huisman, J.A., Lin, C.P., Weihermuller, L., Vereecken, H.: Accuracy of bulk electrical conductivity measurements with time domain reflectometry. *Vadose Zone J.* 7(2), 426–433 (2008)
- [34] ISO, Guide to expression of uncertainty in measurement (1995)
- [35] Kaatze, U.: Complex permittivity of water as a function of frequency and temperature. *J. Chem. Eng. Data* 34(4), 371–374 (1989)
- [36] Kachanoski, R.G., Pringle, E., Ward, A.: Field measurement of solute travel times using time domain reflectometry. *Soil Sci. Soc. Am. J.* 56, 47–52 (1992)
- [37] Kumar, G., Ray, K.P.: *Broadband microstrip antennas*. Artech House, London (2003)
- [38] Lin, C.P.: Analysis of nonuniform and dispersive time domain reflectometry measurement systems with application to the dielectric spectroscopy of soils. *Water Resour. Res.* 39(1), art. no. 1012 (2003)

- [39] Lin, C.P.: Frequency domain versus travel time analyses of TDR waveforms for soil moisture measurements. *Soil. Sci. Soc. Am. J.* 67(3), 720–729 (2003)
- [40] Lin, C.P., Chung, C.C., Tang, S.H.: Accurate time domain reflectometry measurement of electrical conductivity accounting for cable resistance and recording time. *Soil. Sci. Soc. Am. J.* 71(4), 1278–1287 (2007)
- [41] Lin, C.P., Chung, C.C., Huisman, J.A., Tang, S.H.: Clarification and calibration of reflection coefficient for electrical conductivity measurement by time domain reflectometry. *Soil. Sci. Soc. Am. J.* 72(4), 1033–1049 (2008)
- [42] Malicki, M.A., Plagge, R., Roth, C.H.: Improving the calibration of dielectric TDR soil moisture determination taking into account the solid soil. *European J. Soil. Sci.* 47(3), 357–366 (1996)
- [43] Mohamed, A.M.O.: Principles and applications of time domain electrometry in geoenvironmental engineering. Taylor & Francis Group, UK (2006)
- [44] Moret-Fernández, D., Lera, F., Arrùe, J.L., Lòpez, M.V.: Measurement of soil bulk electrical conductivity using partially coated TDR probes. *Vadose Zone J.* 8(3), 594–600 (2009)
- [45] Nielsen, D.M.: Practical handbook of environmental site characterization and groundwater monitoring, 2nd edn. CRC Press, Boca Raton (2006)
- [46] Noborio, K.: Measurement of soil water content and electrical conductivity by time domain reflectometry: a review. *Comp. Electron. Agric.* 31(3), 213–237 (2001)
- [47] O'Connor, K., Dowding, C.H.: Geomeasurements by pulsing TDR cables and probes. CRC Press, Boca Raton (1999)
- [48] Piuze, E., Cataldo, A., Cannazza, G., De Benedetto, E.: An improved reflectometric method for soil moisture measurement exploiting an innovative triple-short calibration. *IEEE Trans. Instrum. Meas.* 59(10), 2747–2754 (2010)
- [49] Ponizovsky, A.A., Chudinova, S.M., Pachepsky, Y.A.: Performance of tdr calibration models as affected by soil texture. *J. Hydrol.* 218(1-2), 35–43 (1999)
- [50] Pozar, D.M.: Microwave engineering, 2nd edn. J. Wiley & Sons Inc., New York (1998)
- [51] Previati, M., Bevilacqua, I., Canone, D., Ferraris, S., Haverkamp, R.: Evaluation of soil water storage efficiency for rainfall harvesting on hillslope micro-basins built using time domain reflectometry measurements. *Agric. Water Manag.* 97(3), 449–456 (2010)
- [52] Regalado, C., Carpena, R.M., Socorro, A.R., Moreno, J.M.: Time domain reflectometry models as a tool to understand the dielectric response of volcanic soils. *Geoderma* 117, 313–330 (2003)
- [53] Rhoades, J.D., Manteghi, N.A., Shouse, P.J., Alves, W.J.: Soil electrical conductivity and soil salinity: new formulation and calibrations. *Soil Sci. Soc. Am. J.* 53, 433–439 (1989)
- [54] Robinson, D.A.: Measurement of the solid dielectric permittivity of clay minerals and granular samples using a time domain reflectometry immersion method. *Vadose Zone J.* 3, 705–713 (2004)
- [55] Robinson, D.A., Jones, S.B., Wraith, J.M., Or, D., Friedman, S.P.: A review of advances in dielectric and electrical conductivity measurement in soils using time domain reflectometry. *Vadose Zone J.* 2(4), 444–475 (2003)
- [56] Roth, C.H., Malicki, M.A., Plagge, R.: Empirical evaluation of the relationship between soil dielectric constant and volumetric water content as the basis for calibrating soil moisture measurements by TDR. *J. Soil Sci.* 43(1), 1–13 (1992)

- [57] Sabbagh, A.M.E., Ramahi, O.M., Trabelsi, S., Nelson, S.O., Khan, L.: Use of microstrip patch antennas in grain and pulverized materials permittivity measurement. In: Proceedings of IEEE Antennas and Propagation Society International Symposium, vol. 4, pp. 42–45 (2003)
- [58] Sakaki, T., Rajaram, H.: Performance of different types of time domain reflectometry probes for water content measurement in partially saturated rocks. *Water Resour. Res.* 42(7) (2006)
- [59] Selker, J.S., Graff, L., Steenhuis, T.: Noninvasive time domain reflectometry moisture measurement probe. *Soil Sci. Soc. Am. J.* 57(4), 934–936 (1993)
- [60] Stangl, R., Buchan, G.D., Loiskandl, W.: Field use and calibration of a TDR-based probe for monitoring water content in a high-clay landslide soil in Austria. *Geoderma* 150, 23–31 (2009)
- [61] Tektronix. User manual-ICConnect and measureXtractor™ TDR and VNA software. Beaverton, OR (2007)
- [62] Todoroff, P., Langellier, P.: Comparison of empirical and partly deterministic methods of time domain reflectometry calibration, based on a study of two tropical soils. *Soil Tillage Res.* 45(3), 325–340 (1998)
- [63] Topp, G.C., Davis, J.L., Annan, A.P.: Electromagnetic determination of soil water content: measurements in coaxial transmission lines. *Water Resour. Res.* 16, 574–582 (1980)
- [64] Topp, G.C., Yanuka, M., Zebchuk, W.D., Zegelin, S.: Determination of electrical conductivity using time domain reflectometry: soil and water experiments in coaxial lines. *Water Resour. Res.* 24(7), 945–952 (1988)
- [65] Waterhouse, R.B.: Microstrip patch antennas: a designer's guide, 1st edn. Kluwer Academic Publications, USA (2003)
- [66] Weast, R.C., Astle, M.J.: Handbook of chemistry and physics, 62nd edn. CRC Press, Boca Raton (1981)
- [67] Webster, J.G.: The measurement, instrumentation and sensors handbook. Springer, New York (1999)
- [68] Yu, X., Drnevich, V.P., Nowack, R.L.: Improvements of soil dielectric mixing model for inversion analysis of time domain reflectometry measurements. In: Proc. TDR 2006: 3rd International Symposium and Workshop on Time Domain Reflectometry for Innovative Soils Applications (2006)
- [69] Zegelin, S.J., White, I., Jenkins, D.R.: Improved field probes for soil water content and electrical conductivity measurement using time domain reflectometry. *Water Resour. Res.* 25(11), 2367–2376 (1989)
- [70] Zurcher, J.F., Gardiol, F.E.: Broadband patch antennas. Artech House Inc., Norwood (1995)

Chapter 6

BMR Characterization of Antennas through the Combined TD/FD Approach

'Science progresses best when observations force us to alter our preconceptions.'

Vera Rubin

Abstract. Antenna characterization measurements are traditionally performed in the frequency domain (FD) through vector network analyzers (VNAs) in anechoic chambers. Nevertheless, the expensiveness of these facilities limits the possibility of using this approach for routine measurements. In this chapter, the strategies for the accurate evaluation of the reflection scattering parameter ($S_{11}(f)$) of antennas, starting from simple time domain reflectometry (TDR) measurements, are described. As a matter of fact, not only are instruments operating in time domain (TD) usually less expensive than VNAs; but they allow performing time windowing, which is the key for excluding the unwanted spurious reflection from the environment, thus avoiding the use of anechoic chamber.

6.1 Introduction

Traditionally, measurements on antennas are carried out in the frequency domain (FD) through vector network analyzers (VNAs) [6], in dedicated facilities (i.e., anechoic chamber). Although this procedure undoubtedly provides highly accurate results, the high costs involved make such procedure virtually impracticable for routine measurements. For this reason, there is an abiding interest for assessing alternative methods (less expensive and yet accurate) for antenna characterization. Starting from these considerations, this chapter focuses on the possibility of measuring the reflection scattering parameter, $S_{11}(f)$, of antennas through the TD/FD combined approach, particularly useful for evaluating the impedance matching performance and the resonance characteristics [17].

TDR has been largely used for the characterization of electronic devices, especially for characterization at low frequencies where VNA have some intrinsic limitations [18]; yet the characterization of antenna through a TD-based approach is still an open issue.

As a matter of fact, some of the advantages of the VNA (e.g., its high dynamic range, frequency resolution and bandwidth) can be achieved with instruments operating in TD, by appropriately tuning some measurement parameters, such as the

time window (T_w), the number of averages, and the sampling period (T_c). Moreover, when reference standards are not readily available, de-embedding the effect of fixtures is easier when using TDR rather than when using a VNA (for example, through a suitable time domain gating) [16].

It is worth mentioning that many existing works deal with the possibility of compensating errors in time domain antenna measurements through time gating techniques [2, 7, 8, 9, 10, 11, 13, 15]. Nevertheless, no work describes a simple procedure to be practically implemented even when basic TD instrumentation (i.e., without any specific additional tool) is used. On such basis, an in-depth analysis that pinpoints the crucial steps for an accurate TDR-based antenna characterization is hereby provided.

Similarly to the applications discussed previously, the overall procedure includes two main steps, namely the TDR waveforms acquisition and the correspondent FD signal evaluation. In the following subsections, both steps are discussed in detail. Starting from theoretical considerations, it is demonstrated that the optimal choice of a specific time window can suitably balance all the effects that limit the final measurement accuracy. The optimal trade-off is reached by

1. optimizing the frequency resolution;
2. maximizing the signal to noise ratio (SNR);
3. including as many TDR multiple reflections so as to obtain a complete spectral picture; and
4. excluding the spurious reflections coming from the surrounding objects.

To assess the proposed method from an experimental point of view, the $S_{11}(f)$ of two antennas was evaluated from TDR measurements performed under different experimental conditions (i.e., choosing different acquisition windows, applying digital filters on TD data, placing reflecting objects near the antenna). The crucial parameters related to the achievement of a measurement accuracy comparable to that provided by the use of a VNA in an anechoic chamber, were individuated and optimized. The obtained data were compared to reference-VNA measurements performed in an anechoic chamber ($S_{11,ref}(f)$), thus definitely validating the accuracy enhancement [3], [5].

On the basis of the aforementioned discussion, the ultimate goal is to demonstrate that TDR-based measurements, in conjunction with a specific data processing, can be regarded as a robust and cost-effective procedure for accurate characterization of antennas.

This paves the way for the use of inexpensive TDR devices in practical applications (without compromising measurement accuracy and reliability), and for the adoption of such a method as the next best thing to VNA measurements in anechoic chamber.

6.2 Measurement Setup for the Validation of the Method

The first considered device is Alien ALR-8610-AC antenna: a patch antenna intended for a Radio Frequency Identification (RFId) reader (Fig. 6.1(a)). The second

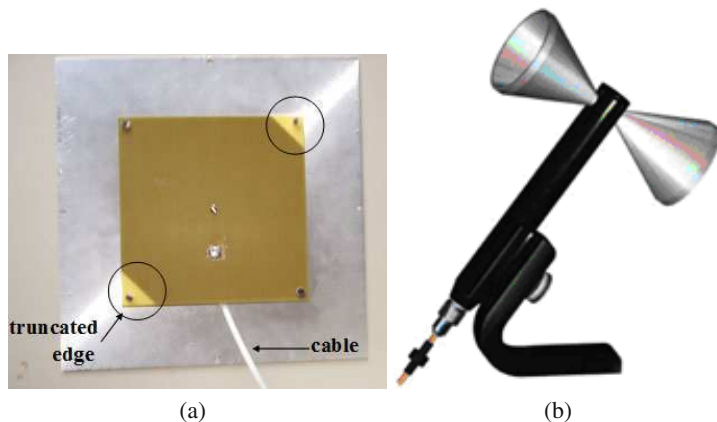


Fig. 6.1 **a** RFID-reader antenna. **b** biconical antenna [3]

is the Clampco Sistemi AP3000 biconical antenna: a wideband biconical antenna (Fig. 6.1(b)).

These antennas have very different characteristics in terms of operating frequency band; in fact, the former is a narrow-band antenna and operates in the 865 MHz–940 MHz frequency range, whereas the latter is a wide-band antenna designed to work in a larger frequency range (80 MHz–3 GHz). The different performance of these two antennas allow assessing the proposed approach for different possible practical conditions.

The TDR measurements were performed through the TDR80E04 module.

6.3 Acquisition in Time Domain

To obtain the corresponding FD information, TDR waveforms are suitably windowed and processed through the FFT-based algorithm described in subsections 3.4.1 and 3.6.2. It is worth noting that for the TD-acquisition, a rectangular windowing is a wise choice, since it provides good balance between amplitude accuracy and frequency resolution for the subsequent FD-transformation.

Averaged TDR measurements were performed setting the maximum number of acquisition points (4000 points), thus forcing the time domain resolution (or sampling period, T_c) to the minimum allowed by the instrument for each considered time window.

When acquiring a TD waveform for a fixed maximum number of measurement points, the only parameter that can be modified is the time window duration. As will be clarified, the choice of this parameter has direct consequences in terms of measurement performance. In order to understand how the time windowing affects the final results, let us briefly recall how the TDR instrument performs measurements.

As already mentioned, the reflected waveform usually includes the so-called multiple reflections due to the signal traveling back and forth between the measurement instrument and the device under test. Multiple reflections contain information on the spectral behavior of the whole system, including those contributions that intrinsically ‘belong’ to the device. Therefore, as a general rule, a time window long enough to include all the multiple reflections occurring before the steady-state condition is achieved, should be set. In this way, the subsequent FD-transformation would provide a complete spectral picture.

Additionally, longer time windows guarantee a better frequency resolution, Δf , of the FD-transformed data, according to the following equation:

$$\Delta f = \frac{1}{T_w} \quad (6.1)$$

where T_w is the duration of the time window.

However, when characterizing antennas, other issues come along. In fact, when the electromagnetic signal generated by the TDR unit enters the antenna connected to it, part of the signal is reflected back due to the impedance mismatch of the physical device (i.e., at the antenna port); nevertheless, another portion of the signal is radiated according to the radiation pattern of the antenna. As soon as the radiated signal reaches an object, it is reflected and the antenna receives the signal that is bounced back. As a consequence, the measured TDR waveform might include unwanted contributions due to some spurious reflections. Such effects can be excluded by choosing an appropriate time window that leaves them out. This is a relevant advantage of TD-based measurements over the direct FD-measurements, and can be considered as the practical way for avoiding the use of the anechoic chamber. Fig. 6.2(a) shows a typical schematization of a TDR antenna waveform: in particular, the grey-colored area corresponds to the portion of the signal that should be included in the acquisition window. Fig. 6.2(b) shows a schematization of the measurement setup in which an antenna is connected to the TDR unit through an L_c -long cable and the nearest reflecting object is placed at a distance d from the antenna. Therefore, the time window that excludes possible unwanted reflections can be calculated through the following equation:

$$T_w = 2 \left(\frac{d}{c} + \frac{L}{v} \right) \quad (6.2)$$

where $c \cong 3 \times 10^8 \text{ ms}^{-1}$ is the speed of light in vacuum, L is the fraction of L_c that corresponds to the portion of the cable included in the time window¹, and v is velocity of the signal propagated in the cable. The incident signal portion is windowed out, as required for the successive FD-processing [16].

¹ In practice, the L -long cable portion inclusion is necessary for effectively performing the subsequent FD-transformation, as reported in [4, 14].

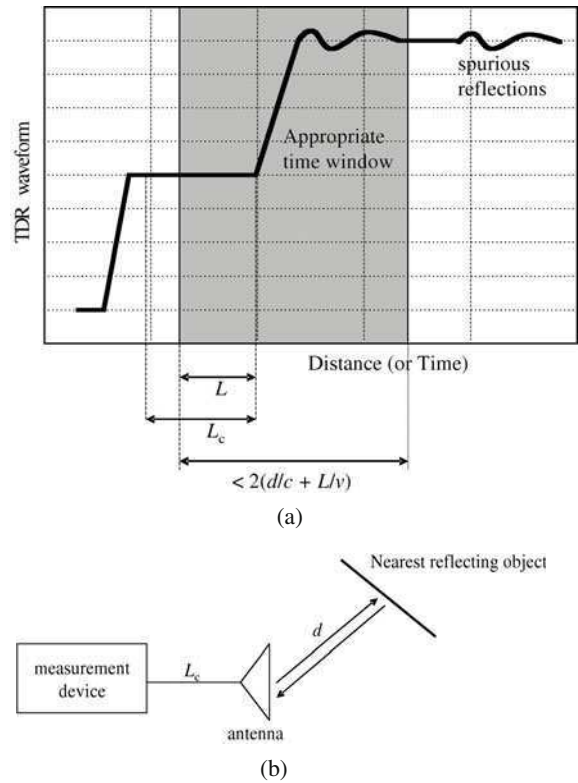


Fig. 6.2 **a** Schematization of a typical TDR waveform. **b** schematization of possible interferences from the environment [5]

6.4 RFID Antenna Results

The configuration of the Alien ALR-8610-AC antenna antenna is shown in Fig. 6.1(a). The truncated edge-geometry of this antenna (highlighted with circles in the figure) is realized to guarantee circular polarization with only one feed point and to generate two closely-spaced resonant frequencies, between which the antenna should operate [12].

The antenna was connected to the TDR module through a 28 cm-long LMR195 cable with a nominal impedance of 50Ω . It is worth underlining an important aspect on the feed of this antenna under test (AUT). The terminal part of the central conductor of the coaxial cable that feeds the antenna is not surrounded either by dielectric insulator or by external jacket: this introduces an additional impedance mismatch (between the 50Ω -cable and the antenna) that inevitably affects the TDR response of the antenna [1].

Before proceeding with the individuation of the most appropriate time window, it is useful to analyze the TDR waveform associated to the antenna. Fig. 6.3(a) shows the TDR waveform of the RFId antenna for a 100 ns-long time window; Fig. 6.3(b) zooms the 0–15 ns range.

The first portion of the waveform at approximately 0.25 V corresponds to the 50 Ω -matched cable portion. The measured time between the beginning of the acquisition window and the end of the cable is 2.8 ns, corresponding to the length L in (6.2). After this portion of cable, there is a brief but abrupt change in the amplitude of the waveform caused by the considerable impedance mismatch introduced by the ‘naked’ termination of the feeding cable (feed pin). The following portion of the waveform carries the antenna ‘imprint’ and, subsequently, the reflected signal approaches the steady-state condition (around the value of 0.5 V that corresponds to the open circuit) through several multiple reflections, whose shape is related to the resonant behavior of the antenna. The attenuating response of the multiple reflections can be clearly distinguished until their peak-to-peak signal excursion is overwhelmed by noise.

6.4.1 Practical Guidelines for Retrieving Accurate Measurements

In this subsection, the results achieved through the FD-transformation of TDR data are reported.

To have a definitive reference to which TDR-based measurements could be compared, the $S_{11,\text{ref}}(f)$ of the AUT was measured through an HP8753C VNA, equipped with the 85047A S-Parameter Test Set, inside an anechoic chamber (Fig. 6.4). After the short-open-load (SOL) calibration procedure, VNA measurement was carried out in the frequency range between 810 MHz and 960 MHz (with a frequency resolution of 1 MHz), since this range corresponds to the operating band of the antenna. The $S_{11,\text{ref}}(f)$ curves (magnitude and phase) are shown in Fig. 6.5(a) and Fig. 6.5(b).

As for the TD measurements, to avoid undesired spurious reflections, measurements were performed outdoor, making sure that no reflecting object was in the nearby of the antenna. A first set of measurement was carried out choosing different time windows, thus evidencing the consequences in the FD-transformed data. Therefore, different TDR waveforms of the AUT were acquired, varying the time windows (T_w), from 10 ns to 100 ns, and the $S_{11}(f)$ data were evaluated. Results are reported in Fig. 6.5(a) and Fig. 6.5(b), for magnitude and phase, respectively, and they are compared to the $S_{11,\text{ref}}(f)$.

The root mean square error (*rmse*) between the magnitude of $S_{11,\text{ref}}(f)$ and the magnitude of each of the $S_{11}(f)$ evaluated from TDR measurement was calculated for qualitatively identifying the most appropriate time window duration: results are summarized in Table 6.1. The *rmse* analysis anticipates that the most appropriate windowing seems to be $T_w = 32$ ns. Starting from this experimental validation, in the following paragraphs an in-depth analysis is conducted, thus demonstrating how the optimal time windowing can be predicted, thus avoiding the use of reference VNA measurements.

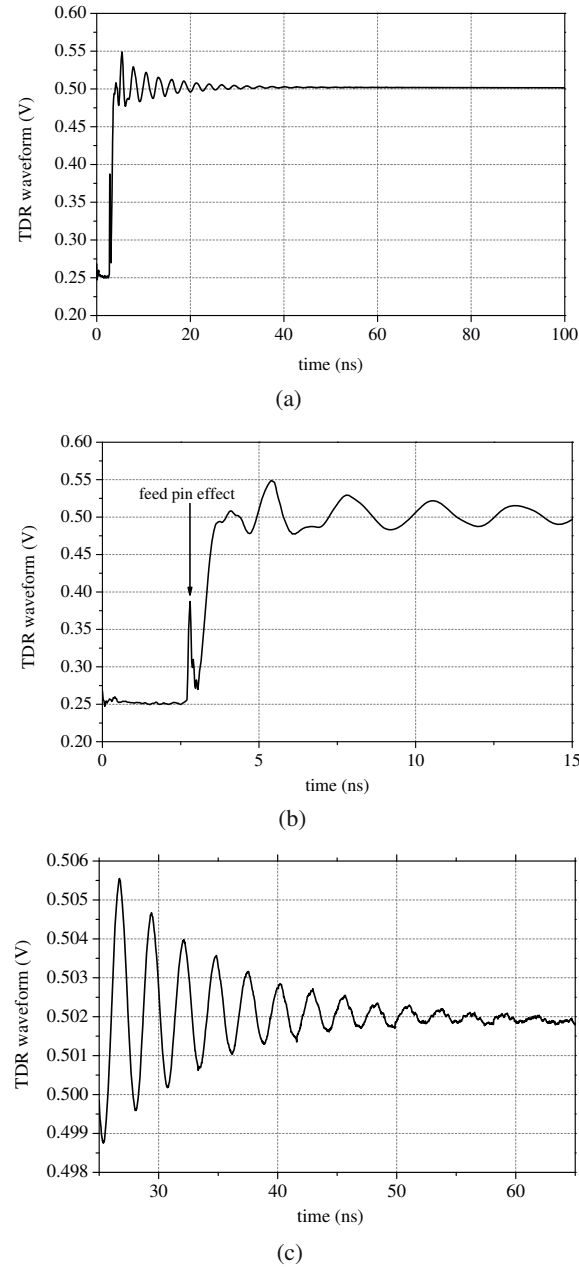


Fig. 6.3 **a** TDR waveform for the RFID antenna for a 100 ns-window. **b** zoom of the beginning of the waveform. **c** zoom of the settling of the waveform



Fig. 6.4 Antenna measurements performed in anechoic chamber [5]

Table 6.1 *rmse* values, over the 810–960 MHz frequency range, between $|S_{11}(f)|$ measured (for different acquisition windows) through the TD/FD combined approach and $|S_{11,\text{ref}}(f)|$

T_w (ns)	<i>rmse</i>
100	0.040
50	0.037
40	0.019
35	0.019
32	0.010
20	0.021
10	0.068

6.4.1.1 Lower Limit for the Acquisition Time Window

As can be seen from Fig. 6.5(a) and Fig. 6.5(b), the $S_{11}(f)$ curve corresponding to a 10 ns-long time window is far from representing the actual antenna behavior. This result can be easily explained considering that according to (6.1), the frequency resolution corresponding to $T_w = 10$ ns is approximately 100 MHz, which is not even adequate to resolve the two closely-spaced resonant frequencies that characterize the AUT. In fact, looking at the specifications, it is known (and it is confirmed by

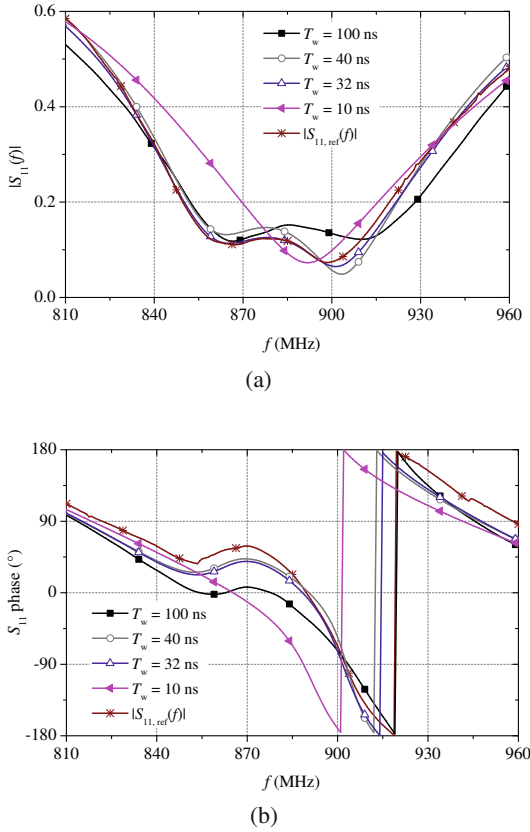


Fig. 6.5 Comparison between the $S_{11}(f)$ measured through the TD/FD combined approach (for different time windows) and the $S_{11,ref}(f)$. **a** magnitude. **b** phase

the $S_{11,ref}(f)$, that the AUT presents two resonant frequencies in its operating frequency range. The analysis of the FD-transformed data in the 810–960 MHz range, confirmed that for $T_w = 10$ ns, $T_w = 20$ ns and $T_w = 30$ ns, the corresponding frequency resolution ensures the presence of one, three, and four spectral components, respectively. As a matter of fact, for $T_w > 20$ ns the frequency resolution seems to be adequate for discriminating the two resonant peaks. Additionally, Fig. 6.3(b) shows that at low times (< 20 ns), multiple reflections effects are still considerable and thus they cannot be windowed out, since the related spectral content is relevant. The frequency resolution requirements, along with the aforementioned considerations, suggest that the lowest limit for the windowing is $T_{w,LOW} > 30$ ns.

6.4.1.2 Upper Limit for the Acquisition Time Window and Interferences from Spurious Reflections

As discussed in the previous section, a longer time window provides both a better frequency resolution and a more complete spectral representation of the response of the device under test.

Nevertheless, considering Fig. 6.5, a longer time window does not necessarily guarantee better results, as can be seen, for example, observing the $S_{11}(f)$ curve corresponding to the 100 ns-long time window. In fact, when time window is increased, noise contribution becomes more relevant; this is the intrinsic measurement limitation for the used instrument.

To verify that the corruption of the measured waveform occurring at longer times (Fig. 6.3(c)) is mostly due to noise contributions, the TDR response of the AUT was simulated through a full-wave simulation software, CST Microwave Studio. The simulation results are reported in Fig. 6.6 for the longer times, and they show a good agreement with the measurement data. As expected, the only difference is the noise absence, since the ideal condition is reproduced.

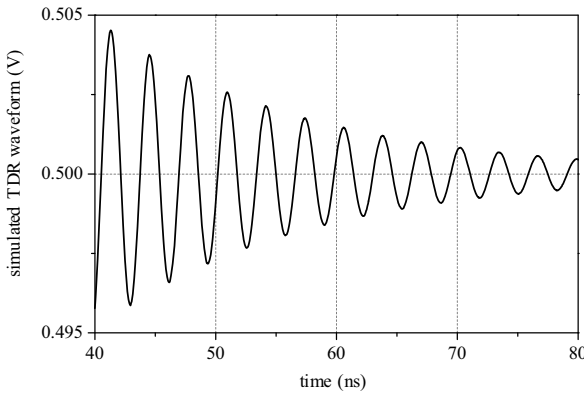


Fig. 6.6 Simulated TDR waveform of the RFID antenna

As mentioned in the previous subsections, another critical issue related to the upper limit for the acquisition window is related to the possible presence of objects in the nearby of the AUT.

To verify the influence of the spurious reflection, a second set of measurement was performed outdoor. Another set of $S_{11}(f)$ measurements was performed using a fixed time window and placing a reflecting object (a steel plate) at a varying distance from the AUT: this allowed making considerations on the interferences occurring, for example, when measurements are performed inside a laboratory.

After arbitrarily setting the time window duration at 27 ns, different waveforms were acquired placing a reflecting steel-made plate in front of the AUT, at a progressively increasing distance (from 1 m to 4 m, with step of 1 m). The steel plate was placed in the direction of maximum radiation of the AUT (i.e., in front of the AUT). Then the scattering parameter was evaluated: results are shown in Fig. 6.7.

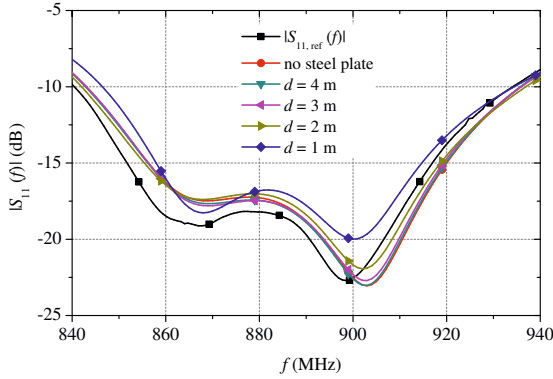


Fig. 6.7 Scattering parameter measurement with a steel plate placed at distance d in front of the antenna

As expected, as the steel plate is taken far from the antenna, the $S_{11}(f)$ curves shift towards the curve of the $S_{11}(f)$ when the steel plate is not present. In particular, the $S_{11}(f)$ curve corresponding to a distance of 4 m from the antenna is practically superimposed to the $S_{11}(f)$ of the antenna in free space: the steel plate seems to have no effect at all. Indeed, with reference to Fig. 6.2(b) and according to (6.2), the distance d corresponding to a time window of 27 ns (which includes the 2.8 ns-portion that corresponds to the cable) is approximately 3.6 m.

The interference of surrounding objects can actually be seen directly in the TD. In this regard, Fig. 6.8 shows the comparison between the TDR waveforms with the steel plate placed at approximately 1 m from the AUT and without.

The two curves overlap up to approximately 10.4 ns (including 2.8 ns of the cable): at this point some differences are clearly detectable. Indeed, according to (6.2), 10 ns correspond to a distance of approximately 1 m. This validates the fact that interferences due to the presence of the reflecting objects in an indoor condition may actually be left out through an appropriate choice of the time window.

Finally, additional measurements were performed comparing TDR waveforms acquired outdoor (making sure that no reflecting object was around) and indoor. As expected, both waveforms appear noisy at longer times, but the indoor-waveform appears corrupted by some additional spurious signals that are definitely attributable to the reflections from the environment: this effect starts to become relevant for a corresponding distance of 5 m, which is approximately the distances of the wall in the room.

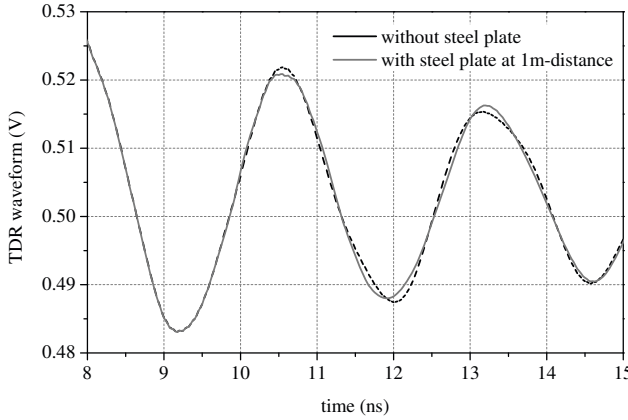


Fig. 6.8 Comparison between TDR waveforms of the antenna, with and without the steel plate placed at a distance of 1 m from the AUT

Therefore, referring to the TDR waveform reported in Fig. 6.3(c), it appears that the upper limit for the time windowing in order to ensure a $\text{SNR} > 1$ is approximately $T_{w,UP} < 35$ ns. SNR measurements, directly available on the used instrument, confirmed these theoretical considerations.

Indeed, longer time windows can be used, provided that the influence of noise is reduced through an appropriate post-processing of the acquired TDR waveform. In particular, a time domain filter can be applied before the FD-transformation. The feasibility of this approach was confirmed by the results achieved applying a 5th order-moving average filter (available within the MATLAB filtering toolbox) to the TD data of a 100 ns-long time window. Fig. 6.9 shows the comparison between the $S_{11,ref}(f)$ curve and the $S_{11}(f)$ curves obtained with and without the application of the filter.

As expected, the $S_{11}(f)$ curve obtained from the filtered TDR waveforms provides a more truthful picture of the AUT response. This is confirmed by the evaluation of the *rmse* between the magnitudes of $S_{11}(f)$ (with and without the application of the filter) and of $S_{11,ref}(f)$: the *rmse* is 0.01 for the filtered data and 0.04 for the non-filtered data.

These results suggest that the choice of a long time window, such as the considered 100 ns-long time window, in conjunction with an appropriate time-domain filtering, can efficiently circumvent the noise limitation, and can simultaneously guarantee a better frequency resolution. Additional experimental results (not reported here for the sake of brevity), confirmed that a long-time windowing, together with the aforementioned filtering procedure, is definitely the most appropriate choice when the frequency response of the device must be retrieved also at the lowest

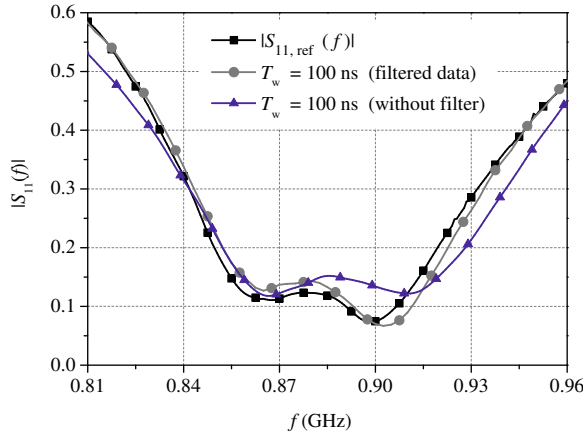


Fig. 6.9 Comparison between the $|S_{11}(f)|$ measured through the TD/FD combined approach (with and without the application of the digital filter) and the $|S_{11,\text{ref}}(f)|$

frequencies. On the other hand, when exploring a limited frequency bandwidth, as in the considered test-case, the optimal time windowing (for the considered AUT) is $30 \text{ ns} < T_w < 35 \text{ ns}$.

6.5 Biconical Antenna Results

As a further experimental validation of the method, the second considered antenna was a biconical antenna (Fig. 6.1(b)), generally used for Electromagnetic Compatibility (EMC) measurements: the wideband characteristics of this antenna anticipate different criteria for the choice of the optimal time window [15].

Similarly to the previous case, the TDR measurements on the antenna were performed by choosing several time windows, ranging from 15 ns to 150 ns; once again, the corresponding $S_{11}(f)$ was extrapolated and compared to the $S_{11,\text{ref}}(f)$ in terms of *rmse* (Table 6.2).

Table 6.2 *rmse* values between $|S_{11}(f)|$ measured (for different acquisition windows) through the TD/FD combined approach and $|S_{11,\text{ref}}(f)|$, for the biconical antenna

T_w (ns)	<i>rmse</i>
150	0.010
100	0.006
80	0.007
40	0.010
35	0.013
15	0.019

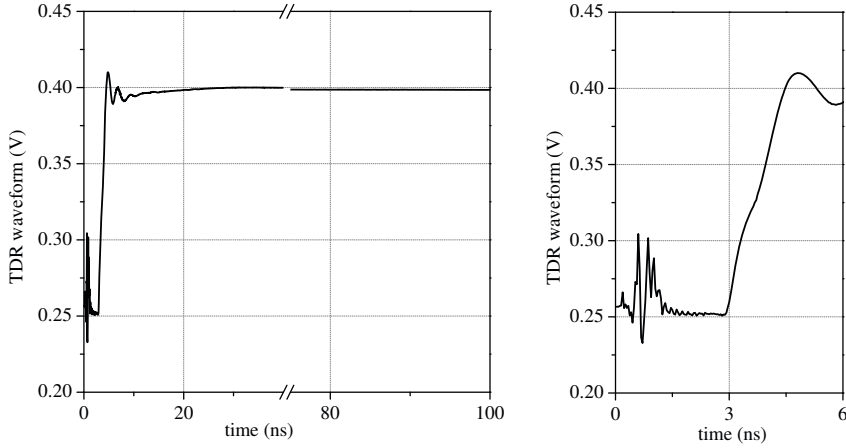


Fig. 6.10 TDR waveform of the biconical antenna for a 100 ns-long time window (left), zoom of the initial portion of the waveform (right) [3]

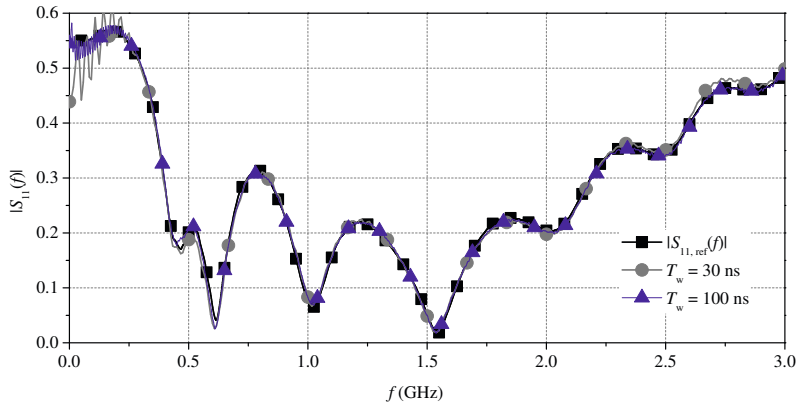


Fig. 6.11 Comparison between $|S_{11,\text{ref}}(f)|$ and the $|S_{11}(f)|$ curves obtained from FD-transformed data for different time windows (T_w), for the biconical antenna [3]

The analysis of the TDR waveform of the biconical antenna (reported in Fig. 6.10) clearly shows that, differently from the previous case, the multiple reflections quickly die out and the signal reaches a steady-state condition in about 20 ns. Nevertheless, such a short T_w would not accurately represent the antenna response at lower frequencies. In fact, Fig. 6.11 shows that even a 30 ns-long time window, although providing overall accurate results, fails in accurately representing the antenna response at low frequencies. On the other hand, if the time window is too long, this will translate in inaccurate results at high frequencies. In fact, since the maximum number of acquisition points is fixed, then the sampling period (T_c) may

become too high, and hence the sampling frequency too low: this represents the upper limit for the maximum frequency f_M . In order to retrieve the frequency response up to $f_M = 3$ GHz, then f_S should be at least 6 GHz, so as to satisfy the sampling theorem. As a result, the corresponding T_c should be lower than 0.166 ns. Considering that, for a fixed time window, the used instrument provides 4000 measurement points in TD, the maximum time window must be shorter than 666 ns.

Indeed, the maximum time window should be definitely shorter. In fact, the used TDR instrument performs a real-time sampling only for time windows shorter than 120 ns: beyond this limit, the instrument samples in equivalent-time. As a matter of fact, equivalent-time sampling is inappropriate when such one-shot signals are considered. Therefore, it is advisable to use windows shorter than 100 ns. Additionally, it is worth pointing out that, in this case, the intrinsic noise limitation is not critical, since the steady-state condition is not reached through an oscillating and attenuating transient.

The aforementioned considerations may be summarized as follows: if T_w is too short, then results will be less accurate at low frequencies, conversely, if T_w is too long, this will result in inaccurate results at high frequency.

On such basis, Fig. 6.11 shows that a 100 ns-long time window provides overall accurate results over the entire considered frequency range. The evaluation of the *rmse* values (reported in Table 6.2) confirmed that a 100 ns-long time window (for which real-time sampling is assured), provides the best results in terms of accuracy. The *rmse* value corresponding to a 150 ns-long time window confirms the performance degradation for higher time windows.

References

- [1] Time domain reflectometry theory. Agilent Application Note 1304-2, Palo Alto, CA (2006)
- [2] Alenkowicz, H., Levitas, B.: Using of sampling scope for antenna measurements in time and frequency domain. In: Proceedings of the 13th International Conference on Microwaves, Radar and Wireless Communications, pp. 313–316 (2000)
- [3] Cataldo, A., De Benedetto, E., Cannazza, G., Monti, G.: A reliable low-cost method for accurate characterization of antennas in time domain. *Metrol. Meas. Syst.* 15(4), 571–583 (2008)
- [4] Cataldo, A., Catarinucci, L., Tarricone, L., Attivissimo, F., Piuze, E.: A combined TD-FD method for enhanced reflectometry measurements in liquid quality monitoring. *IEEE Trans. Instrum. Meas.* 58(10), 3534–3543 (2009)
- [5] Cataldo, A., Monti, G., De Benedetto, E., Cannazza, G., Tarricone, L., Catarinucci, L.: Assessment of a TD-based method for characterization of antennas. *IEEE Trans. Instrum. Meas.* 58(5), 1412–1419 (2009)
- [6] Hemming, L.H.: Electromagnetic anechoic chambers: a fundamental design and specification guide. Wiley-IEEE Press, Piscataway (2002)
- [7] Henderson, A., James, J.R., Newham, P., Morris, G.: Analysis of gating errors in time domain antenna measurements. *IEE Proceedings H Microwaves, Antennas and Propagation* 136, 311–320 (1989)

- [8] de Jongh, R.V., Hajian, M., Ligthart, L.P.: Time domain antenna measurements: implementation and verification of a novel technique. In: Proceedings of the 27th European Microwave Conference and Exhibition, Jerusalem, pp. 470–475 (1997)
- [9] Klembowski, W., Levitas, B., Ponomarev, D., Proshin, V.: Method of time domain antenna measurements and its application to field test of radar antenna subsystem. In: Proc. CIE Int. Conf. Radar, Beijing, pp. 511–514 (1996)
- [10] Lestari, A.A., Suksmono, A.B., Kurniawan, A., Bharata, E., Yarovoy, A.G., Ligthart, L.P.: A facility for UWB antenna measurements in time domain. In: Proc. IEEE International Workshop on Antenna Technology: Small Antennas and Novel Metamaterials, pp. 109–112 (2005)
- [11] Levitas, B.N.: Time domain antenna measurement systems. In: Proc. 3rd Int. Conf. Ultrawideband and Ultrashort Impulse Signals, Sevastopol, pp. 90–95 (2006)
- [12] Milligan, T.A.: Modern antenna design. John Wiley & Sons Inc., Hoboken (2005)
- [13] Okhovvat, M., Fallahi, R.: Measurement of antenna reflection coefficient in time domain. In: Proc. 11th International Conference on Mathematical Methods in Electromagnetic Theory, pp. 328–330 (2006)
- [14] Tektronix. User manual-ICConnect and measureXtractorTM TDR and VNA software. Beaverton, OR (2007)
- [15] Waiyapattanakorn, C., Parini, C.G.: Theoretical and experimental investigations of using time domain gating in antenna pattern measurements. In: Proc. 8th Int. Conf. Antennas and Propagation, Edinburgh, vol. 1, pp. 327–330 (1993)
- [16] Wakayama, C., Loyer, J.: Correlation between VNA and TDR/TDT extracted S-parameters up to 20 GHz. Tech. Rep. (2005)
- [17] Woopoung, K., Swaminathan, M., Li, Y.L.: Extraction of the frequency-dependent characteristic impedance of transmission lines using TDR measurements. In: Proc. of 3rd Electronics Packaging Technology Conference, Singapore, pp. 191–197 (2000)
- [18] Woopoung, K., Joong-Ho, K., Dan, O., Chuck, Y.: S-parameters based transmission line modeling with accurate low-frequency response. In: Proc. of 2006 IEEE Electrical Performance of Electronic Packaging, pp. 79–82 (2005)